STUDY OF ANODIC OXIDE FILMS ON TITANIUM AND TITANIUM-ZIRCONIUM ALLOYS AND THEIR POTENTIAL FOR CAPACITIVE ENERGY STORAGE

by

MIN KYONG CHUNG

Submitted in partial fulfillment of the requirements

For the degree of Doctor of Philosophy

Dissertation Adviser: Dr. Gerhard E. Welsch

Department of Materials Science and Engineering

CASE WESTERN RESERVE UNIVERSITY

January, 2016

CASE WESTERN RESERVE UNIVERSITY

SCHOOL OF GRADUATE STUDIES

We hereby approve the thesis/dissertation of

Min-Kyong Chung

candidate for the Doctoral of Philosophy degree. *

(signed) Gerhard E. Welsch
(chair of the committee)

Matthew A. Willard

Alp Sehirlioglu

Francis L. Merat

Date of Defense January 12, 2015

*We also certify that written approval has been obtained for any proprietary material contained therein.

Dedicated to my parents for their unparalleled love,

to my adorable daughter, Eajae, and my beloved wife, Hyesun

“The only true wisdom is in knowing you know nothing.”

— Socrates

Table of Contents

List of Tables

List of Figures

List of Abbreviations

symbol	definition	SI Unit
A	surface area of electrode	[m^2]
a	oxidation number	
A_r	atomic weight	kilograms [kg]
C	capacitance	farad [F]
C_{ideal}	capacitance of an ideal capacitor	
D	particle dimension	
$\boldsymbol{D}$	dielectric displacement	[C m^{-2}]
d	thickness of oxide layer	meter [m]
$\widetilde{D}$	diffusion coefficient	[cm^2s^{-1}]
$d_{(hkl)}$	interplanar spacing	
DF	dissipation factor	
$\boldsymbol{E}$	electric field strength	[V m^{-1}]
$E_{breakdown}$	breakdown potential	
E_g	band gap energy	electron volts [eV]
E_{OCP}	open circuit potential	
E_{pp}	primary passive potential	
EW	equivalent weight	[g mol^{-1}]
F	Faraday's constant (96,485 C mol^{-1})	
f	frequency	hertz [Hz]
f_m	mass friction	
G	Gibbs free energy	[kJ/mol]
H	enthalpy	[kJ/mol]
I	current	ampere [A]
i	current density	[A m^{-2}]

i_{crit}	critical current density	
I_{leak}	leakage current	
i_{pass}	passive current density	
m	mass resolved	
N_{EQ}	total number of equivalent	[mol g^{-1}]
n	refractive index	
P	pressure	
P	polarization	[C m^{-2}]
p	porosity	percentage [%]
P_c	power of the capacitor	[J s^{-1}]
Q		coulomb [C]
q	electric charge density	[C m^{-2}]
Q_{CPE}	coefficient of constant phase element (CPE)	[Ω^{-1} s^n]
R	resistance	ohm [Ω]
R_{ESR}	equivalent circuit resistance (ESR)	
s	complex frequency for Laplace transform	
T	temperature	Kelvin [K] or Celsius [°C]
t	time	second [s] or hour [h]
U_c	energy stored in the capacitor	joule [J]
V	potential difference	volt [V]
V_{SHE}	standard hydrogen electrode potential	[V_{SHE}]
W	molar mass	[g mol^{-1}]
w	weight	kilograms [kg]
x	distance of diffusion	centimeter [cm]
Z	impedance	ohm [Ω]
z	the number of moles of electrons for oxidation	mole [mol]
Z^*	complex impedance	
Z" or Z_{im}	imaginary part of impedance	
Z' or Z_{re}	real part of impedance	

Greek

$\tan \delta$	loss tangent	
α	depression factor for constant phase element	
Γ	optical path difference	
δ	loss angle	degree [˚]
ε	permittivity	[Fm^{-1}]
ε_r''	complex permittivity	
ε_0	permittivity of vacuum (8.845×10^{-12} Fm^{-1})	
ε_r	relative permittivity	
ε_r'	real component of complex relative permittivity	
ε_r''	imaginary component of complex relative permittivity	
λ	color wavelength of oxide	meter [m]
ρ	density	[g cm^{-3}]
τ	time constant of self-discharge	second [s]
Φ	phase angle	degree [˚]
χ_e	electric susceptibility	
ω	angular frequency	hertz [Hz]

Acknowledgement

I would like to express my most sincere gratitude and appreciation to my thesis advisor, Dr. Gerhard E. Welsch, for his guidance, suggestions and patience throughout this study. His warm encouragement and unlimited support were always the best motive to me to step forward. Thanks to him for giving me a lot of inspiration, and also opportunity to do this work with him. I also would like to thank my committee members, Professor Matthew A. Willard, Professor Alp Sehirlioglu, and Professor Francis L. Merat. I deeply and truly appreciate their helpful suggestion and criticism, which make my dissertation better. Also I would like to thank Mr. Jim Berilla and Dr. Danqi Wang for helping me for experimental works.

I would like to appreciate my parents, and their endless support. Finally, I gratefully thank my daughter, Eajae, and my beloved wife, Hyesun for her unlimited support.

Study of Anodic Oxide Films on Titanium and Titanium-Zirconium Alloys and their Potential for Capacitive Energy Storage

Abstract

by

MIN-KYONG CHUNG

Anodic oxide films were formed on titanium and titanium-zirconium alloys. They were studied for their ability to serve as dielectrics for storage of electrical energy and for their utility as anodes of electrolytic capacitors. The work comprised a study of the development of structure and electrochemical properties of TiO_2 and of mixed TiO_2-ZrO_2 oxide films during their short-time anodic formation and during long-time repair-anodization in oxidizing electrolyte.

The TiO_2 anodic films evolved from an initially homogeneous amorphous state by nucleation of nanometer-sized grains and by additional recrystallization into films with islands of nm-grains and eventually with 'anatase'-phase oxide nodules. They

became embedded in the inner parts of the film, forming a stratified oxide layer and eventually replaced and overgrew most of the original anodic film. During this development the electrochemical parameters and the oxide-dielectrics' property changes were recorded in-situ and interpreted by electrochemical impedance spectroscopy (EIS) and by equivalent circuit (EC) modeling. The permittivity of the films increased as a result of the recrystallization. However, their leakage currents increased also and diminished their useful electric field strength. Mixed TiO_2-ZrO_2 films were formed by anodizing Ti-Zr alloy. They developed in similar fashion as the TiO_2 films, except they remained relatively homogenous during long-time anodization because of their resistance to recrystallization. They maintained a lower leakage current and were better suited as a capacitor dielectric.

Another objective was the development of a process to synthesize homogeneous anodes of Ti-Zr anode alloy with high surface enhancement. The process is based on magnesiothermic reduction of titanium and/or zirconium halides and the sinter-bonding of the so-formed alloy particles. It formed nanocomposites of interpenetrating Ti-Zr alloy and magnesium-halide salts. After removal of the salts by distillation open-porous alloy specimens were obtained that could be anodized to convert their surface into a continuous (Ti-Zr)O_2 oxide film. By variation of the processing times and temperatures the process rates of reduction and sintering could be controlled. Ti-Zr alloy sponge samples were produced with nm-sized branch and pores. They were suited as electrolytic capacitor anodes.

Chapter 1 Research Objectives and Introduction

1.0 Research Objectives

The present work addresses Ti and Ti-Zr alloy and their anodic oxides as potential anodes and dielectrics for electrolytic capacitors with the following objectives;

i. Anodic Formation of Titanium Oxide on Unalloyed Titanium and Evaluation of its Capacity to Serve as an Energy-Storing Dielectric in Electrolytic Capacitors

ii. Anodic Formation of Titanium-Zirconium Oxide on Ti-Zr Alloy and Evaluation of its Capacity to Serve as an Energy-Storing Dielectric in Electrolytic Capacitors

iii. Synthesis of Open-Porous Ti-Zr Alloy and Evaluation of its Suitability as Surface-Enhanced Capacitor Anode

1.1 Introduction to Capacitors, Anodic Oxide Synthesis and Electrochemical Evaluation Methods

A capacitor is an energy storage device that uses a dielectric to accumulate electric charges on electrodes. It is useful for many engineering applications requiring energy storage and power-conditioning, such as in power electronics circuits. Of the various capacitor types the electrolytic capacitors have the highest energy density. To enable the trends of miniaturization of electronic products capacitors with higher energy density are desired. Such electrolytic capacitors with dielectric films that have high electric field strength, high permittivity and reliability against rapid self-discharge and electrical breakdown can serve this purpose. Surface-enhanced anodes are desired that enable a large volume fraction of energy-storing dielectric in a capacitor.

Since a “Leyden jar”—a prototype of capacitor—was invented by Dutch physicist Pieter van Musschenbroek in the mid 18th century, the capacitor has developed rapidly as effective “energy storage” [1]. The original idea of the Leyden jar that stores electrostatic energy between two metal electrodes separated by glass jar has been advanced to the system that uses various kinds of dielectric media in order to raise the capacity of electric charge storing. Owing to frequency dependence in alternating current (AC) circuits, a capacitor can serve diverse functions in circuits, such as filtering, blocking, ac-dc separation, and coupling-decoupling [2] [3].

Capacitor is essential in electrical power management. An example of this is in portable devices. Here, capacitors are used for circuit components, energy storage and signal power [3]. Dielectrics with small thickness, high permittivity, high field strength and low leakage current are the key components of capacitors.

Capacitors with diverse dielectrics are used commercially. They are often named for their dielectric media; for instance, vacuum capacitors, mica capacitors, paper film capacitors, ceramic capacitors, etc. Electrolytic capacitors are named for their construction in which an electrolyte is used on the cathode-side of the capacitor's dielectric to enable anodic self-repair. Table 1-1 shows various capacitor types and their applications.

Table 1-1. Types of capacitors and their applications [2] [3] [4] [5] [6] [7] [8] [9]

Capacitor Types	Dielectric	Relative Permittivity @ 1kHz	Capacitance Range	Typical Dielectric Loss	Main Applications
Vacuum Capacitors	vacuum	1			high power RF transmitter
Paper Capacitors	paper	1.2-2.6		1%	
Mica Capacitors	mica	5-7	1 pF ~100 nF	0.1%	
Glass Capacitors	glass	5-10	1 pF ~10 μF	0.1-3%	
Multi-Layer Ceramic Capacitors	ceramics		1 pF ~100 μF	1-3%	electronics use
Polymer Film Capacitors	polymers (PP, PET, PEN, etc.)	2.2-3.0	100 pF ~33 nF	0.1-2%	electronics use, electric power source
Aluminum Electrolytic Capacitors	Al_2O_3		0.5 μF ~10 μF	2%	electronics use, high frequency circuit use, power supply
Tantalum Electrolytic Capacitors	Ta_2O_5		0.01 μF ~1000 μF	6%	electronics use, telephone exchange, AC motors
Supercapacitors	Helmholtz Double Layer	-	~3×10^6 μF	-	memory back-up, electric and hybrid vehicles, portable power supplies

Energy is stored entirely in the dielectric of a capacitor. To maximize energy density, i.e., the energy stored per capacitor volume implies that one should maximize the volume fraction of dielectric in a capacitor. The energy density of a dielectric is determined by ($½\ \varepsilon_0\varepsilon_r \boldsymbol{E}^2$) i.e., the product of permittivity of vacuum (8.845×10^{-12} Fm^{-1}), relative permittivity and the square of the electric field strength $\boldsymbol{E}$. To maximize the dielectric's energy density the values of ε and $\boldsymbol{E}$ should be high. Metals with anodically formed oxide films that exhibit reasonably high values of these properties are used as anodes in electrolytic capacitors. Tantalum with anodic pentoxide (Ta/Ta_2O_5) film forms the most energy-dense commercial capacitor anodes [3] [10]. Similarly, anodic niobium oxide on niobium and aluminum oxide on aluminum form useful anodes. They work because their anodic oxides form stable passive dielectric layers with reasonably high ε and $\boldsymbol{E}$ values [10] [11] [12]. A study by Badawy et al. showed Ta-oxide layer to exhibits nearly ideal capacitive behavior, that is, the phase angle between current and voltage was close to 90° in electrochemical impedance spectroscopy [13]. Tantalum pentoxide was found to be more stable than niobium pentoxide [14] and titanium dioxide [15].

Capacitors with high volume fraction of dielectric can be made from surface-enhanced tantalum anodes that are fabricated from dendritic tantalum sponge particles [16] [17]. When anodized, these surface-enhanced Ta/Ta_2O_5 anodes form the basis for industrially used tantalum electrolytic capacitors [18] [19]. However, because tantalum is a relatively rare element with only 2×10^{-4} wt.% in the Earth's crust [20],

such capacitors are rather costly. The price of commercial-purity (99.8%) Ta is more than $400/kg [21], and when made as surface-enhanced capacitor-grade material its price more than doubles. The prices for capacitor-grade tantalum sponge have fluctuated around the $1,000/kg market during the last decade. It is of interest to find a lower-cost material, e.g., Ti.

Titanium is a 'valve-metal' that forms a thin passive oxide layer on its surface. It is attractive for the anode of an electrolytic capacitor, because TiO_2's dielectric constant value is higher than those of most other metal oxides used for the electrolytic capacitors, such as Nb_2O_5 or Al_2O_3 [4] [5]. If one considers energy per unit mass, then the titanium dioxide is additionally competitive because its density (3.78 g/cm^3 of anatase and 4.23 g/cm^3 of rutile) is significantly lower than the 8.18 g/cm^3 of Ta_2O_5. Another factor in the energy density consideration is the dielectric strength $\boldsymbol{E}$ of titanium dioxide. It is comparable to or may be slightly higher than that of tantalum pentoxide dielectric. The value for $TiO_2 \approx 0.75$ V/nm compared to 0.7 V/nm of Ta_2O_5 [22] [23]. These high electric field strengths are only obtained on defect-free dielectrics. A relatively defect-free anodic TiO_2 oxide films could sustain a high electric field, comparable to anodic Ta_2O_5 oxide films. Despite these characteristics for being a potential dielectric medium of an electrolytic capacitor TiO_2 has weaknesses, namely intermediate states within the band gap caused by lattice defects or impurities; these enable electron hopping between valence band, the intermediate states and the conduction band. The titanium oxide film then behaves as a semiconductor and exhibits thermally activated leakage current when lattice defects

in the oxide create intermediate states in its band gap [5]. It is then a poor insulator, and allows electrons to flow through the oxide layer and cause self-discharge of a capacitor. This is called “direct leakage current (DCL)”. It leads to self-discharge, instability, and short lifetime of a capacitor. Owing to defects in the oxide structure causing electronic state within the band gap, a poly-crystalline anodic titanium oxide layer shows relatively high value of leakage current compared to other metal oxides such as Ta_2O_5 and Al_2O_3 used in electrolytic capacitors [22] [23].

In order to reduce its leakage current, we consider alloying titanium with zirconium and by anodizing form a mixed-oxide dielectric. Zirconium is transition metal with similar chemical-physical properties to titanium. Zirconium itself is also able to form a protective passive oxide layer and shows a relatively high value of permittivity [4] [5]. It is reported that Zr can hinder the formation of crystalline oxide on the Ti-Zr alloy and form a more stable amorphous oxide layer on the Ti-Zr alloy [24] [25] with reduced leakage current.

Prescribing a large specific surface area is a way to increase the capacitance of an electrolytic capacitor. Most anodes of electrolytic capacitors have a ‘porous sponge structure’ to increase their area to accumulate electric charges. Sintering is a frequently used process to fabricate porous anodes for the electrolytic capacitors. For titanium a calcio- or magnesiothermic reduction process of titanium compounds (usually $TiCl_4$) could be used for the synthesis of the metal as well as of a porous metallic sponge. The Kroll process for reduction of $TiCl_4$ with Mg or Ca is a potential method to fabricate porous anodes. One of the objectives of the present work is to

synthesize porous Ti-Zr alloy anodes by a similar reduction method. Then a surface oxide film is grown on the sponge surface to serve as the dielectric of a capacitor

1.2 Electrolytic Capacitors: Theory and Characteristics

1.2.1 Theory of Operation

From the time of the Leyden jar, a basic construction of capacitors has not been changed much; it basically consists of at least two electrodes that have terminals for electrical connection to the circuit and dielectric materials (Figure 1-1-(a)). Conductive materials (e.g., metal plates) are used for the electrodes while insulators are used for dielectrics, such as mica, metal oxides, ceramics, plastic films, paper and even air. The dielectric materials are non-conductive materials. Their purpose is to sustain electric field between opposing metal plates. When the capacitor is connected to an electrical circuit and a voltage is applied, it develops an electric field across the dielectric and induces negative and positive charges on opposite metal plates (Figure 1-1-(b)). Dipole moments are formed in the molecules of the medium, aligning the positive charges along the electric field and the negative charges against it. This is called dielectric polarization. It creates an opposite electric field and for a given applied electric field it decreases the localized electric field inside the dielectric. Electrical energy is stored in the form of positive and negative charges held apart by the dielectric against the attraction forces provided by the applied electric field.

(Figure 1-1 (c)). A good insulator should be used for the dielectric to prevent the recombination of the electrical charges through the dielectric, i.e., to prevent leakage current. Recombination of the electrical charges is allowed only through the 'load' of an external circuit when the stored energy is to be harvested.

1.2.2 Characteristics of Capacitor

1.2.2.1 Capacitance and Relative Permittivity

Figure 1-1-(a) shows a capacitor with parallel, equal-sized conductive metal plates separated by a dielectric medium (figure 1-1-(a)). Assume that it is an ideal capacitor which can store and release electrical energy with no dissipation, and behaves like a perfect insulator. Polarization $\boldsymbol{P}$ is in proportion to the electric field strength, $\boldsymbol{E}$.

$$\boldsymbol{P} = \varepsilon_0 \chi_e \boldsymbol{E} \tag{1-1}$$

The polarization $\boldsymbol{P}$ is defined as the dipole moment per unit volume. χ_e is called the electric susceptibility, and is a second-rank tensor. ε_0 is the permittivity of vacuum, 8.845×10^{-12} Fm^{-1}. The electric susceptibility represents how readily the dielectric is polarized by an externally applied electric field. The electric displacement, $\boldsymbol{D}$, in the linear dielectric is,

$$\boldsymbol{D} = \varepsilon_0 \boldsymbol{E} + \boldsymbol{P} = \varepsilon_0 \boldsymbol{E} + \varepsilon_0 \chi_e \boldsymbol{E} = \varepsilon \boldsymbol{E} \tag{1-2}$$

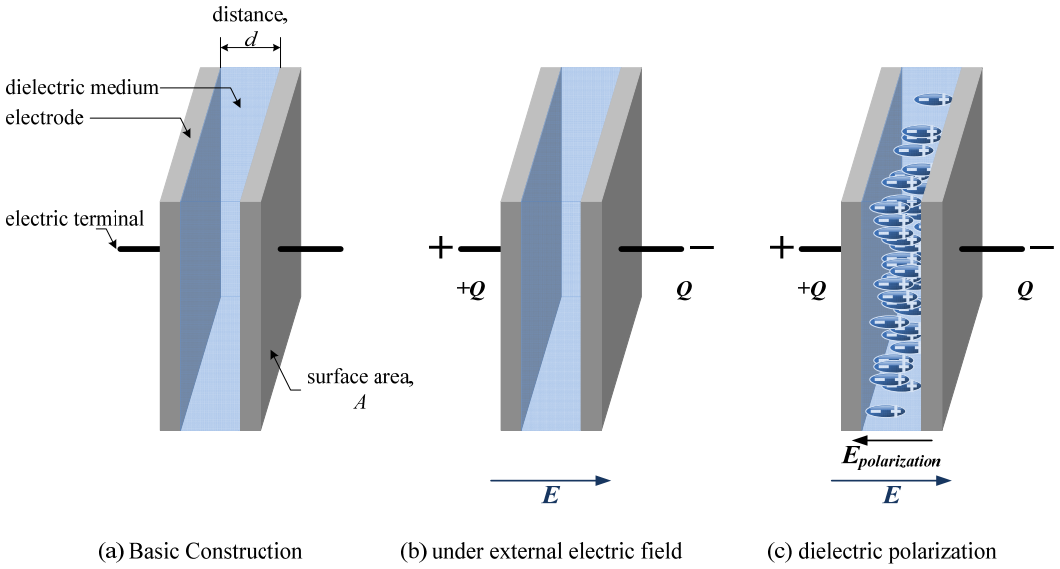

Figure 1-1. Schematic diagrams of simple capacitor, (a) construction of separated electrodes, (b) under applied electric field, (c) under an applied field mitigated by a dielectric

ε is the permittivity of a material.

$$\varepsilon = \varepsilon_0 (1 + \chi_e) \tag{1-3}$$

The electric displacement, $\boldsymbol{D}$, is a vector field in the dielectric, and is also called total electric flux density. Its magnitude is equal to the total charge density on the metal plates, σ_T,

$$|\boldsymbol{D}| = \sigma_T = \varepsilon \boldsymbol{E} \tag{1-4}$$

which leads to

$$\sigma_T = \varepsilon \boldsymbol{E} = \frac{q}{A} = \varepsilon \frac{V}{d} \tag{1-5}$$

q is electric charge, A is surface area of the plates, d is distance and V is potential difference between the two plates. The potential difference between the plates is a line integral of $\boldsymbol{E}$ on a path from positive plate to negative plate. The amount of electrical charge that is held on the plate is proportional to the applied voltage, V. The capacitance, C, of the capacitor is,

$$C = \frac{q}{V} \tag{1-6}$$

Assume that the linear dielectric is used as the medium of capacitor. Comparing two equations above,

$$C = \frac{q}{V} = \frac{\varepsilon A}{d} \tag{1-7}$$

ε_r is the relative permittivity of the dielectric material. It is the ratio of the permittivity of the dielectric to that of vacuum, ε_0. The absolute permittivity, ε is often represented by the product $(\varepsilon_r \varepsilon_0)$. With equation 1-3, it can be described as,

$$\varepsilon = \varepsilon_0 \varepsilon_r = \varepsilon_0 (1 + \chi_e) \tag{1-8}$$

Therefore, the capacitance of the capacitor is,

$$C = \frac{\varepsilon_0 \varepsilon_r A}{d} \tag{1-9}$$

1.2.2.2 Energy Density and Power Density

U_c, defines the total amount of energy stored on a capacitor. It is described below.

$$U_c = \int_0^Q V \mathrm{d}q = \int_0^Q \frac{q}{C} \mathrm{d}q = \frac{1}{2}\frac{Q^2}{C} = \frac{1}{2} C V^2 = \frac{1}{2} V^2 \cdot \left(\frac{\varepsilon_0 \varepsilon_r A}{d}\right) \tag{1-10}$$

Energy density can either be stated as the amount of storable energy per unit volume (J/L) or per unit mass (J/kg) of the dielectric or of the packaged capacitor.

$$energy\ density = \frac{\left(\frac{1}{2}CV^2\right)}{volume}\,[\mathrm{J/L}] \tag{1-11}$$

or

$$specific\ energy = \frac{\left(\frac{1}{2}CV^2\right)}{mass}\,[\mathrm{J/kg}] \tag{1-12}$$

The power of the capacitor can be described by,

$$P_c = \frac{\mathrm{d}U_c}{\mathrm{d}t} = \frac{\mathrm{d}}{\mathrm{d}t}\left(\frac{1}{2}CV^2\right) = CV(t)\frac{\mathrm{d}V}{\mathrm{d}t} \tag{1-13}$$

1.2.3 Non-Ideal Behavior of Capacitor

1.2.3.1 Equivalent Series Resistance(ESR)

A practical capacitor in an electric circuit does not act as an ideal component as it suffers energy loss during discharge through an external circuit. The loss is caused by the circuit's resistance and is called equivalent series resistance (ESR). It is the sum of in-phase resistance caused from the capacitor's components i.e., the

electrolyte, the electrodes, and their interfaces. In a circuit operating with alternating current (AC), charging and discharging the capacitor with a specified frequency, the ESR can be measured. A circuit representation of a practical capacitor is shown in figure 1-2. It depicts the series combination of an ideal capacitor and a resistor representing the ESR.

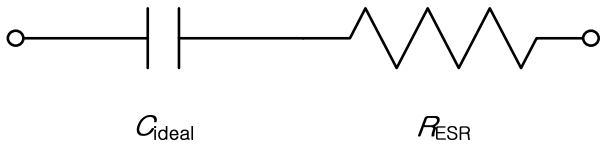

Figure 1-2. Equivalent circuit model of a practical capacitor; a series connection of an ideal capacitor, $C_{ideal,}$ and equivalent series resistance, R_{ESR}

The impedance of a practical capacitor at an arbitrary frequency is,

$$Z = R + \frac{1}{j\omega C} = Z_{\mathrm{re}} + Z_{\mathrm{im}} = Z' + Z'' \quad (1\text{-}14)$$

where, Z is impedance of a practical capacitor, and ω is an angular frequency. Z_{re} and Z_{im} (or Z' and Z'') represent the real and the imaginary part of AC impedance. The ESR is defined as the real part of the impedance, which causes 'energy loss' whereas the imaginary part of the impedance means 'energy stored'.

$$ESR = Z_{\mathrm{re}} = Z' = R_{\mathrm{ESR}} \tag{1-15}$$

Since the ESR represents non-ideality of the capacitor, that is, ‘energy loss’ by its definition, it is definitely related to other non-ideal characteristics of the practical capacitor, such as self-discharge time and, particularly, dielectric loss.

1.2.3.2 Leakage Current through Dielectric

The dielectric of the ideal capacitor is an ideal insulator. In actuality a small current can flow through the dielectric. It is called ‘leakage current’. It is caused by imperfections of dielectrics, such as impurities and grain boundaries [26], which introduce intermediate energy states into the band gap of the dielectric. These enable electrons to channel from the valence to the conduction band with a greatly reduced activation energy, e.g., significantly smaller than 3eV. The value of kT at room temperature (approximately 0.025eV) may then suffice to activate the occurrence of leakage current. When defects are present with a distribution and number density enabling transverse (semi)-conductive paths through the dielectric film localized leakage current is likely. Tunneling is also reported to be one of the reason of leakage current in a metal oxide dielectric film that behaves like a semiconductor rather than a perfect insulator.

Leakage current can be estimated by following equation, measuring the voltage decrease under open circuit potential (OCP) during self-discharging of a charged capacitor [27].

$$I_{\text{leak}} = C\frac{\mathrm{d}V}{\mathrm{d}t} \tag{1-16}$$

where I_{leak} is the leakage current, C is capacitance of the given capacitor, V is potential and t is time measuring potential drop under OCP. The measured voltage drop ($\mathrm{d}V/\mathrm{d}t$) can be fitted by software. It can be measured by potentiostatic polarization technique; for example, at a specific voltage the leakage current is measured over time, e.g., after 3 or 5 minutes. Leakage current is activated by temperature (kT, where k is Boltzmann's constant). For electrolytic capacitors with liquid electrolyte it is usually measured at room temperature and up to the boiling point of the electrolyte. In this research, the potentiostatic polarization technique was used at room temperature to investigate leakage current through anodic oxide films. It can provide electrochemical information of the anodic thin oxide layer of the anode.

1.2.3.3 Self-Discharge Time

During self-discharge the stored charge and voltage of the capacitor drop exponentially with time. One wants this time to be long. The time to drop to 1/e of the

initial value is obtained from the RC time constant. Here, the resistance R is that across the dielectric. The value of C is measured with an LCR meter. Another discharge time refers to the time a capacitor can be discharged intentionally to harvest its energy. Here the RC-time constant is controlled by the ESR resistance of the capacitor and the additional resistance of a load. An additional resistance component from inductive impedance may be added. For high-power or high-frequency use one wants this time to be short.

$$\tau = R_{\mathrm{ESR}} \cdot C \tag{1-17}$$

1.2.3.4 Dielectric Loss Tangent

Energy loss of a practical dielectric can be quantified in terms of dielectric loss tangent, tan δ, which is closely associated with the ESR. It is also termed the dissipation factor, DF, and defined as a ratio (occasionally expressed as a percentage) of energy loss to energy stored. It is described by the loss angle, δ, in the complex impedance plane (figure 1-3).

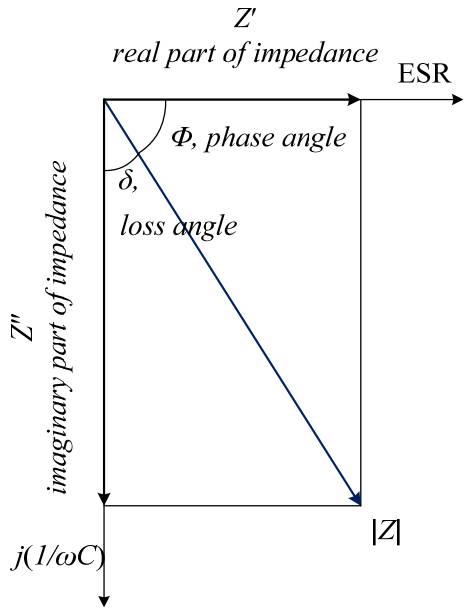

Impedance Plane

Figure 1-3. Phase angle and loss angle plotted in the complex impedance plane

Due to its frequency dependency, the relative permittivity can be described as complex permittivity, ε_r^*, with real ($\varepsilon_r^{'}$) and imaginary ($\varepsilon_r^{''}$) components.

$$\varepsilon_r^* = \varepsilon_r^{'} - j\varepsilon_r^{''} \tag{1-18}$$

and it shows a relation with complex impedance, Z^*,

$$Z^* = Z^{'} + jZ^{''} = \frac{1}{j\omega C_0 \varepsilon_r^*} \tag{1-19}$$

where ω is angular frequency ($\omega = 2\pi f$) and C_0 is geometrical capacitance with vacuum ($C_0 = \varepsilon_0 A/d$) [28]. From above equations, Z' and Z'' can be derived,

$$Z' = \frac{\varepsilon_r''}{\omega C_0(\varepsilon_r'^2 + \varepsilon_r''^2)} \tag{1-20}$$

$$Z'' = \frac{-\varepsilon_r'}{\omega C_0(\varepsilon_r'^2 + \varepsilon_r''^2)} \tag{1-21}$$

Conclusively, the loss tangent can be described as follows [29] [30] [31] [32] [33] [34];

$$\tan\delta = \frac{\varepsilon_r''}{\varepsilon_r'} = -\frac{Z'}{Z''} \tag{1-22}$$

thus,

$$\delta = arc\,tan\left(-\frac{Z'}{Z''}\right) = 90 - arc\,tan\left(-\frac{Z''}{Z'}\right) = 90 - \phi \tag{1-23}$$

By definition, the tangent of phase angle, *Φ*, equals the ratio of -*Z*″ to *Z*′. When the phase angle approaches to 90˚, the dielectric exhibits low energy loss. Using the electrochemical impedance spectroscopy (EIS) technique, the phase angle of the

dielectric can be plotted with range of frequency (Bode plot). Also, the dielectric loss tangent can be measured by LCR meter.

1.3 Anodization for Oxide Film Growth and Electrochemical Analysis Methods

1.3.1 Potentiostatic Polarization

'Potentiostatic' consists of two words, 'potentio-' and 'static' that mean [potential] and [constant]. Potentiostatic polarization is an electrochemical method to apply a constant DC potential to electrodes in a cell. The anode is polarized, and oxidation occurs on its surface. The current density can be measured, and the amount of cations that participate in the oxidation reactions to form the thin oxide film can be estimated. It is useful to characterize corrosion/electrochemical behavior of metal surface and the formation of a passive oxide layer during 'anodization'.

Figure 1-4 shows a schematic diagram for anodization and for measurement of leakage current in the present research. A conventional electrochemical cell with two electrodes is used to anodize the anode material. Current and voltage are recorded in real time by a computer. In the present research potentiostatic polarization was carried out to form anodic oxide layers. The current during anodization was measured in-situ.

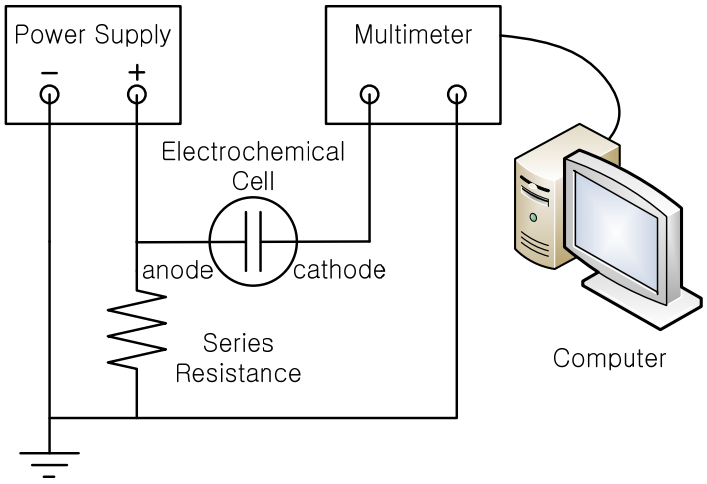

Figure 1-4. Setup for anodization and electrochemical analyses.

Figure 1-5 shows a schematic graph of the potentiostatic polarization at fixed voltage. During the initial few seconds, the voltage increases at a constant applied current. When the voltage reaches the maximum pre-set level, it is maintained at the constant preset value. When the dielectric film is fully formed, it develops an opposing field and then the current drops. For an ideal dielectric of infinite resistance the current should drop to zero. During the formation of a real dielectric an incompletely-passive oxide layer is formed; upon reaching its full thickness the current decreases rapidly (exponentially) with time and levels out at a finite value; it is the “leakage current”.

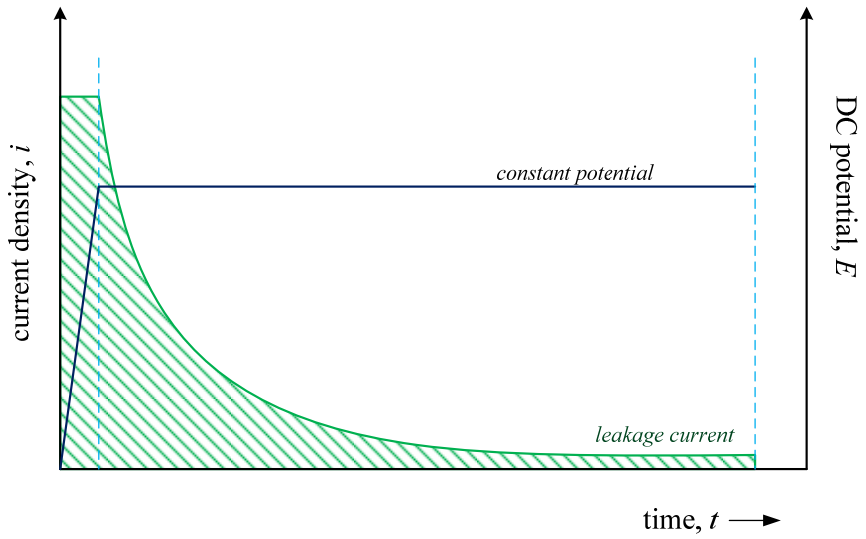

Figure 1-5. Plot of anodizing current with time; the growth of an oxide film of certain thickness to balance the applied electric field is represented by potentiostatic polarization as a function of time

1.3.2 Potentiodynamic Polarization

During potentiodynamic anodic polarization the applied potential is gradually increased and the current is measured. The current is plotted as a function of applied potential on the potential-current plane. The measured contains the electrochemical information on the anodic reaction. It shows whether the specimen corrodes, or forms a passive oxide layer [35].

Figure 1-6 shows a schematic diagram of potentiodynamic anodic polarization for an exemplar metal forming a passive oxide layer. The potential scan starts from the open circuit potential (OCP, at the point A in figure 1-6). The open circuit

potential, also referred to as the equilibrium or corrosion potential, is a voltage at which anode and cathode are in equilibrium. Corrosion current between anode and cathode is minimized; it is the passive region.

In most electrochemical tests, the OCP is measured first. As the anodic potential increases, the metal dissolution occurs on the anode surface (Reaction 1-a).

$$\mathrm{M} \rightarrow \mathrm{M}^{a+} + a\mathrm{e}^{-} \tag{1-a}$$

M is a metal that is anodized in an aqueous solution (the solution). a is an oxidation number.

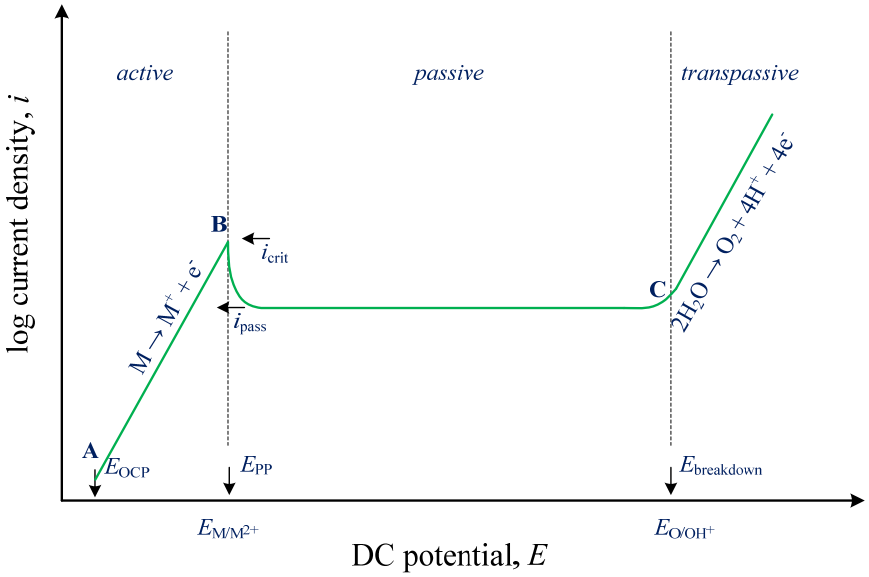

Figure 1-6. Diagram of potentiodynamic anodic polarization measurement

At the inflection point B, metal ions are oxidized and start forming a thin oxide layer. The potential at point B is called the 'primary passive potential', E_{pp}, and the associated current is called the 'critical current', i_{crit}. They indicate the starting condition for passivation. If the oxide layer is passive, and sufficiently resistive to restrain migration of metal ions and penetration of oxygen ions, it acts as an insulator. The current density remains at a low constant level with further potential increases. The more resistive the oxide layer, the lower is the constant passive current density, i_{pass}. The general reaction is,

$$aM + bH_2O \rightarrow M_aO_b + 2bH^+ + 2be^- \quad (1\text{-b})$$

At the point C, the transpassive region begins. Oxygen evolution now occurs on the anode surface.

$$H_2O(l) \rightarrow O_2(g) + 4H^+(aq) + 4e^- \quad (1\text{-c})$$

The standard oxygen reduction potential in an aqueous solution is 1.229 V_{SHE} (standard hydrogen electrode) when pH = 0 [35]. The value varies with pH described by the Nernst equation.

$$E_{O/OH^+} = 1.229 - \frac{0.059}{4}\log\frac{1}{p(O_2)[H^+]^4} \quad (1\text{-}24)$$

$p(O_2)$ is the partial pressure of oxygen. It is 1 atm in the standard state. If the pH value for a given solution is known, one can calculate the oxygen reduction potential at which water dissociates, and oxygen gas is generated on the anode surface. The current density in the transpassive region at which oxygen evolution occurs can determine the extent of passivity of the oxide layer.

1.3.3 Estimation of the Thickness of Anodic Oxide Layer using Faraday's Law of Electrolysis

According to M. Faraday, the amount of reacted metal ions at the anode is proportional to the electric charge that flows from the anode into the cathode. Since we can measure the electric charges (= current × time) in the oxidation reaction, it is possible to calculate the amount of reacted metal. The reaction is [35];

$$m = \left(\frac{Q}{F}\right)\left(\frac{A_r}{z}\right) \quad (1\text{-}25)$$

where m is mass reacted (grams), Q is total electric charge (coulomb/mole), F is Faraday's constant (96,485 coulomb/mole), A_r is the atomic weight (or relative atomic

mass, grams), and z is the number of moles of electrons required to oxidize the element in the oxidation process (mole). A_r/z is an equivalents weight, EW, i.e., the mass of metal (in gram) that is oxidized by the passage of one mole of electrons.

For alloys the equivalent weight is more complex. Assuming that there is no selective oxidation of an alloy, and every component of the given alloy equally participates in the oxidation process. Also the oxidation process forms a homogeneous and uniform oxide layer on the alloy surface. The total number of equivalents, N_{EQ}, is determined by sum of the fractions of equivalents of the alloy elements.

$$N_{\mathrm{EQ}} = \sum \frac{z_{\mathrm{i}} f_{\mathrm{i}}}{A_{\mathrm{r,i}}} \tag{1-26}$$

z_i represents the valence of the i^{th} element of the alloy, and f_i is the mass fraction of the i^{th} element. $A_{r,i}$ is the atomic weight of the i^{th} element in the alloy. The equivalent weight of an alloy, EW_{alloy}, is the reciprocal of the N_{EQ} [36],

$$EW_{\mathrm{alloy}} = \frac{1}{N_{\mathrm{EQ}}} = \frac{1}{\sum \frac{z_{\mathrm{i}} f_{\mathrm{i}}}{W_{\mathrm{i}}}} \tag{1-27}$$

Assuming that the metal ions fully contribute to form a uniform oxide layer, the total amount of dissolved metal ions can be estimated from the volume of the formed oxide. Thus,

$$m = \rho A d = \left(\frac{Q}{F}\right) EW \tag{1-28}$$

where, ρ is density of the oxide, A is area that oxide layer formed and d is thickness of the layer. With Q/A as the charge density,

$$\rho d = q\left(\frac{1}{F}\right) EW \tag{1-29}$$

The total electric charge can be calculated by integration of the product of current i_{ox} and time t.

$$q = \int_0^t i_{ox} \mathrm{d}t \tag{1-30}$$

where, i_{ox} is the Faraday current density that converts Ti-atoms into Ti^{4+} cations that forms the oxide film a given surface area during anodizing. The charge q determines how many cations are formed on a given area and determines how thick

the oxide layer will be. If one considers that the growth and final thickness of the anodic oxide is proportional to the number of electrical charges that have generated cations (e.q. Ti^{4+}) and have combined them with anions (e.q. $2O^{2-}$), one can estimate the final thickness of anodic oxide layer as [35],

$$d = \left(\frac{1}{\rho F}\right) EW \int_0^t i_{\mathrm{ox}} \mathrm{d}t \tag{1-31}$$

Hence, with equation 1-31 and the current density measured during potentiostatic polarization, one can estimate the thickness of the oxide layer on pure titanium or on a Ti-Zr alloy.

1.3.4 Electrochemical Impedance Spectroscopy (EIS)

Electrochemical impedance spectroscopy (EIS) is a sensitive analysis methods using AC signal to evaluate the electrochemical behavior of a dielectric medium. Since it was suggested by O. Heaviside in the late 19th century [37], it has been used to study of a great variety of electrochemical reactions, including corrosion, batteries, corrosion inhibitors, biomaterials, fuel cells as well as electrolytic and electrochemical capacitors [38] [39] [40].

While other electrochemical testing method uses DC potential/current as input signals, EIS is based on the acquisition of measured-current response to a sinusoidal

perturbation with small amplitude and variable frequency on top of a dc bias voltage. EIS results can be plotted in the form of Nyquist, Cole-Cole (similar to Nyquist plot) and/or Bode plots. They are analyzed by fitting the recorded spectra to an equivalent circuit model using software. Through fitting analyses, the electrochemical behavior of the metal surface or the anodic thin oxide layer can be described by an "equivalence model" that consists of electronic components (capacitors, resistors, inductors) and electrochemical elements (such as Warburg impedance elements, constant phase elements). From the components of the equivalent circuit models, values of film resistance and capacitance can be estimated. Electrochemical impedance, modulus, and even dielectric loss tangent can be obtained from EIS analysis. EIS is sensitive, non-destructive and a highly informative method for analysis of frequency-dependent properties of oxide films [38] [39] [40].

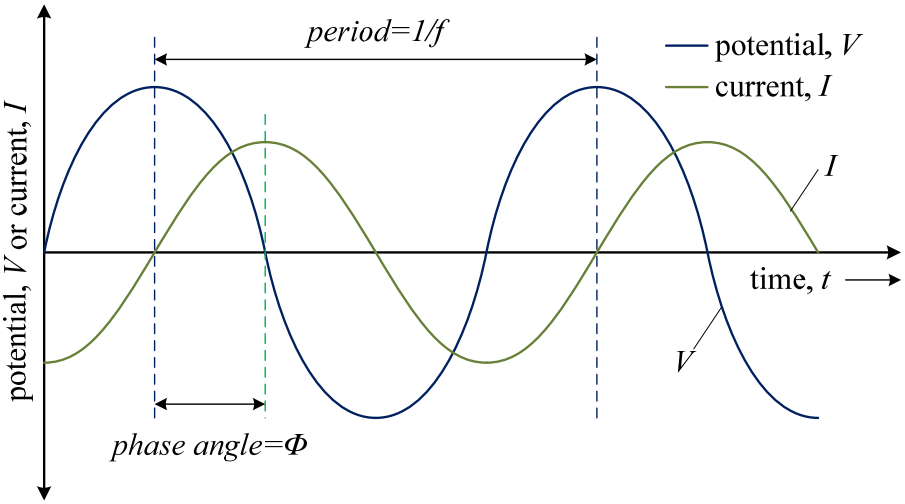

Figure 1-7. Sinusoidal waveforms of potential $V(t)$ and current $I(t)$

1.3.4.1 Time Dependent Current Response for Sinusoidal Alternating Potential Input

The term of impedance in alternating current (AC) circuit plays a similar role to resistance in direct current (DC) circuit; In the AC circuit, both potential and current show time-dependent sinusoidal signals as shown in figure 1-7. Taking account of potential $V(t)$ and resistance R, Ohm's Law can be applied to obtain the current (I) in an AC circuit.

$$V(t) = I(t)R \tag{1-32}$$

For a series circuit with a resistance R and capacitance C, the total potential drop is obtained by summation of the potential drops in each component. The time dependence of voltage in a capacitor-containing circuit can be expressed as [41],

$$V(t) = I(t)R + \frac{q(t)}{C} = I(t)R + \frac{1}{C}\int_0^t I(t)\mathrm{d}t \tag{1-33}$$

In order to solve complicated integral-differential equations, Heaviside suggested using a Laplace transform to convert them into algebraic equations [37]. It transforms the time-dependent function of $f(t)$ to a new frequency-dependent function, $F(s)$, the Laplace transform. By the inverse Laplace transform the frequency (s) domain function can be returned to the time domain function. Heaviside's suggestion was criticized when he first suggested the process [42]. However, today the Laplace

transform is widely used in circuit analysis for electrical engineering.

Let $f(t)$ be a function defined on $[0, \infty)$. Using Laplace transform;

$$\mathcal{L}[f(t)] = F(s) = \int_0^{\infty} e^{-st} f(t) \mathrm{d}t \tag{1-34}$$

and,

$$\mathcal{L}\left[\int_0^t I(t) \mathrm{d}t\right] = \frac{I(s)}{s} \tag{1-35}$$

where s is complex frequency (or Laplace frequency [37]). Thus, from the Laplace transform, the following equations about potential $V(s)$ and current $I(s)$ are obtained.

$$V(s) = I(s)R + \frac{1}{C} \cdot \frac{I(s)}{s} = I(s)\left(R + \frac{1}{sC}\right) \tag{1-36}$$

$$I(s) = \frac{V(s)}{\left(R + \frac{1}{sC}\right)} \tag{1-37}$$

From the definition of the capacitance above, impedance equals to a ratio between potential and current. Therefore [41] [40],

$$Z(s) = \frac{V(s)}{I(s)} = R + \frac{1}{sC} \tag{1-38}$$

The SI unit of the impedance is Ohm [Ω]. In the EIS the applied input signal shows time-dependent sinusoidal waveform that was explained in Figure 1-7. Thus, it is able to be described by

$$V(t) = V_0 \sin(\omega t) \tag{1-39}$$

where V_0 means maximum amplitude. ω is the angular frequency of the sinusoidal waveform in radians/second (unit of s^{-1}), which is,

$$\omega = 2\pi f \tag{1-40}$$

f is AC signal frequency. Thus, the period of AC cycle is described as follows

$$period = \frac{1}{f} = \frac{2\pi}{\omega} \tag{1-41}$$

Using the Laplace transform of the sine function,

$$\mathcal{L}[\sin(\omega t)] = \frac{\omega}{(s^2 + \omega^2)} \tag{1-42}$$

equation 1-37 can be rewritten with equation 1-39 as follows

$$I(s) = \frac{V_0}{\left(R + \frac{1}{Cs}\right)} \cdot \sin(\omega t) = \frac{V_0}{\left(R + \frac{1}{Cs}\right)} \cdot \frac{\omega}{(s^2 + \omega^2)} \tag{1-43}$$

which can be rearranged,

$$I(s) = \frac{V_0}{R\left(1 + \left(\frac{1}{sRC}\right)\right)}\left(\frac{\omega}{s^2 + \omega^2}\right) = \frac{V_0}{R}\left(\frac{\omega}{s^2 + \omega^2}\right)\left(\frac{1}{\frac{1}{s}\left(s + \left(\frac{1}{RC}\right)\right)}\right)$$

$$I(s) = \frac{V_0}{R}\left(\frac{\omega}{s^2 + \omega^2}\right)\left(\frac{s}{s + \left(\frac{1}{RC}\right)}\right) \tag{1-44}$$

$$= \frac{V_0}{R\left[\omega^2 + \left(\frac{1}{RC}\right)^2\right]}\left[\left(\frac{\omega}{s^2 + \omega^2}\right)\left(\omega^2 + \frac{s}{RC} - \frac{(s^2 + \omega^2)}{RC\left(s + \left(\frac{1}{RC}\right)\right)}\right)\right]$$

$$= \frac{V_0}{R\left[\omega^2 + \left(\frac{1}{RC}\right)^2\right]}\left[\omega^2\left(\frac{\omega}{s^2+\omega^2}\right) + \frac{\omega}{RC}\left(\frac{s}{s^2+\omega^2}\right)\right.$$

$$\left. - \left(\frac{\omega}{RC}\right)\left(\frac{1}{\left(s + \left(\frac{1}{RC}\right)\right)}\right)\right]$$

taking the inverse Laplace transform, $\mathcal{L}[\sin(\omega t)] = [\omega/(s^2+\omega^2)]$,

$$I(t) = \frac{V_0}{R\left[\omega^2 + \left(\frac{1}{RC}\right)^2\right]}\left[\omega^2 \sin(\omega t) + \frac{\omega}{RC}\cos(\omega t)\right.$$

$$\left. - \left(\frac{\omega}{RC}\right) exp\left(-\frac{t}{(RC)}\right)\right] \tag{1-45}$$

The third term in the above equation is zero since it is related to a transitory response of the AC signal. Thus, it would be re-arranged,

$$I(t) = \frac{V_0}{R\left[1 + \left(\frac{1}{\omega RC}\right)^2\right]}\left[\sin(\omega t) + \frac{1}{\omega RC}\cos(\omega t)\right] \tag{1-46}$$

By introducing tan $\Phi = 1/\omega RC$, above equation is described as below.

$$I(t) = \frac{V_0}{R\left[1 + \left(\frac{1}{\omega RC}\right)^2\right]} \cdot [\sin(\omega t) + \tan\phi \cos(\omega t)] \tag{1-47}$$

It is arranged into simpler form [41];

$$I(t) = \frac{V_0}{\sqrt{R^2 + \frac{1}{(\omega C)^2}}} \cdot \sin(\omega t + \phi) = \frac{V_0}{|Z|}\sin(\omega t + \phi) \tag{1-48}$$

where Φ is phase angle between potential V and current I. In the AC circuit, there must be phase difference between potential and current by the phase-shifted angle Φ. $|Z|$ is length of vector obtained by two perpendicular vectors, R and $1/\omega C$. It can be represented with potential input, V_0, and current response I_0,

$$|Z| = \frac{V_0}{I_0} \tag{1-49}$$

Therefore, the time-dependent current response, *I(t)*, in figure 1-7 can be derived from equation 1-48 and 49,

$$I(t) = I_0 \sin(\omega t + \phi) \tag{1-50}$$

recall equation 1-39, the sinusoidal alternating potential input, *V(t)* is,

$$V(t) = V_0 \sin(\omega t) \tag{1-39}$$

1.3.4.2 Impedance of Electrical Circuit

So far, the periodic perturbation of AC current with sinusoidal wave form has been expressed with phase angle, Φ, and angular frequency, ω. Now we can approach to describe the complex impedance, Z^*, using complex notation.

$$Z^* = Z(j\omega) = \frac{V(t)}{I(t)} = \frac{V_0 \sin(\omega t)}{I_0 \sin(\omega t + \phi)} = |Z| \frac{\sin(\omega t)}{\sin(\omega t + \phi)} \tag{1-51}$$

also,

$$Z(j\omega) = Z' + Z'' = R + \frac{1}{j\omega C} = R - j\frac{1}{\omega C} \tag{1-52}$$

where,

$$Real\ part\ of\ impedance = Z' = R \tag{1-53}$$

$$imaginary\ part\ of\ impedance = Z'' = \frac{1}{\omega C} \tag{1-54}$$

The modulus, $|Z|$, can be expressed,

$$|Z| = \sqrt{(Z')^2 + (Z'')^2} = \sqrt{R^2 + \left(\frac{1}{\omega C}\right)^2} \tag{1-55}$$

Using Euler's formula, it can be described by cosine and sine,

$$Z(j\omega) = |Z|exp(j\phi) = |Z|[cos(\phi) + j\sin(\phi)] \tag{1-56}$$

Impedance complex expressed above equation is illustrated in figure 1-8 with Euler's relation.

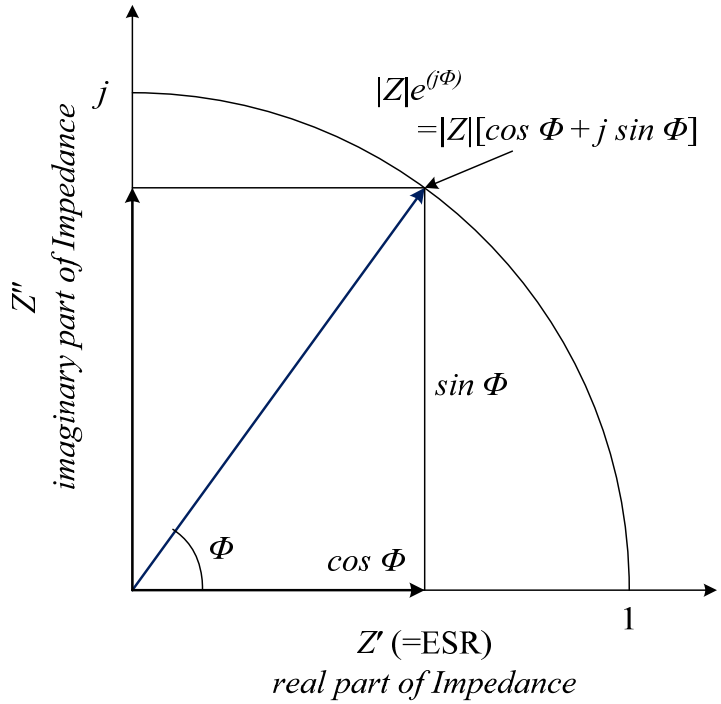

Impedance Plane

Figure 1-8. Impedance in the complex plane

1.3.4.3 Data Representation of Impedance

Using the complex plane mentioned above, impedance can be plotted against the variable frequency. In this chapter, impedance of basic and common electrical circuits that have ideal resistor and capacitor is introduced. Also, the case that electrical circuit consists of non-ideal components is also reviewed.

1.3.4.3.1 Impedance Data for Ideal capacitor-Electrical Circuits

Almost all examples in real experimental work on corrosion or other electrochemical study cannot be represented by ideal electrical components. However, it is worth to know the graphical representation of electrical circuits by ideal components. Here is two of very basic graphical example of impedance representation; parallel combination (R|C) and series-parallel combination (R-(R|C).

1.3.4.3.1.1 Parallel Combination of Ideal Resistor and Capacitor

Figure 1-8 shows a basic circuit of parallel combination with ideal resistor and capacitor. At high frequency, entire current flows through the capacitor where the phase angle, Φ, is -90º (*tan* δ=0). From Kirchhoff's Law for a parallel circuit, the total current in the simple parallel circuit is defined by the sum of currents that flow through each electrical component. Thus, it can be described by following equations,

$$I(t) = \frac{V(t)}{R} - \frac{\omega C V(t)}{j} = V(t)\left[\frac{1}{R} - \frac{\omega C}{j}\right] = V(t)\frac{(1 + (\omega RC)^2)}{R - j\omega R^2 C} \qquad (1\text{-}57)$$

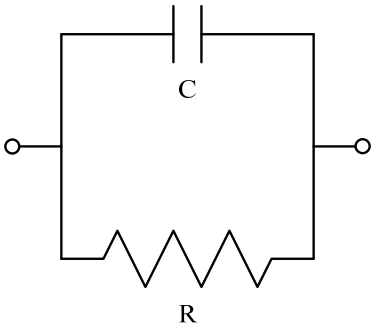

Figure 1-9. Equivalent circuit of a capacitor

Rearrange above equation as a function of impedance, then we can get,

$$Z(j\omega) = \frac{R}{1+(\omega RC)^2} - j\frac{\omega R^2 C}{1+(\omega RC)^2} \tag{1-58}$$

Impedance can be separately expressed as the part of real and imaginary, thus equation 1-53 and 1-54 can be re-expressed as impedance with function of ω. Using equation 1-58,

$$Z'(\omega) = \frac{R}{1+(\omega RC)^2} \tag{1-59}$$

$$Z''(\omega) = \frac{\omega R^2 C}{1+(\omega RC)^2} \tag{1-60}$$

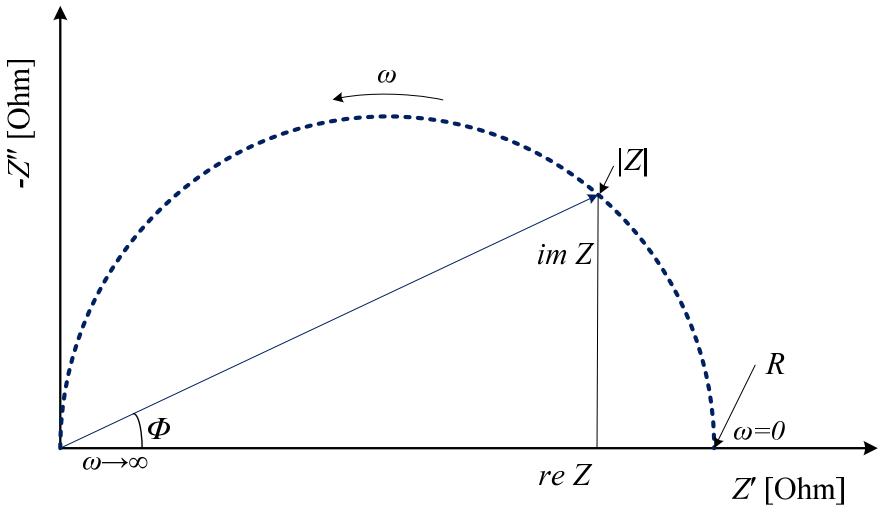

(a) Nyquist plot

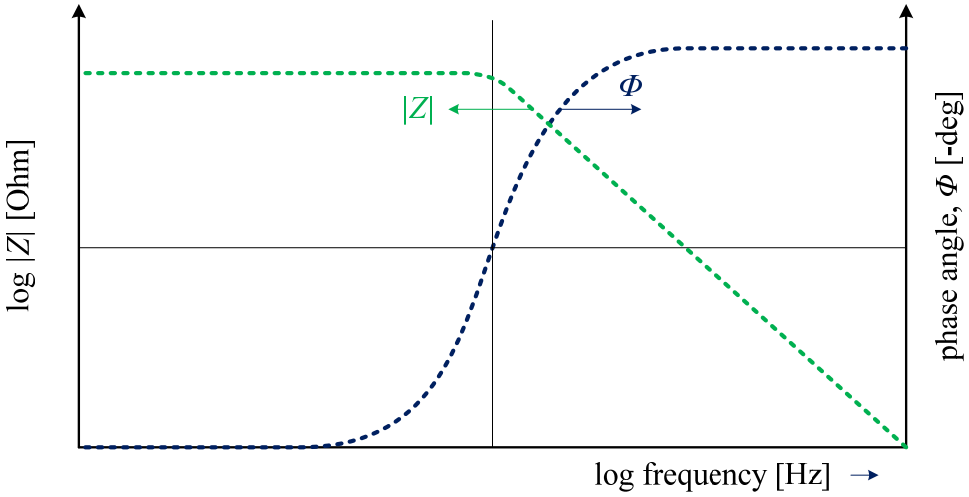

(b) Bode plot

Figure 1-10. Plots of the impedance vector for the R|C circuit
(a) in a Nyquist plot, and (b) in a Bode plot

A Nyquist plot represents EIS results with variable frequency in the complex plane. It is one of the most common methods of the graphical representation in EIS analysis. The real part of the measured impedance is plotted on the x-axis and the imaginary part on the y-axis. The impedance data derived from equation 1-59 and 1-60 can be plotted by the Nyquist and Bode plot, and it is shown in figure 1-10. In general, the Nyquist plot shows a semi-circle: $|Z| = R$ at $\omega = 0$, and $|Z| = 0$, at $\omega \rightarrow \infty$. The Bode plot (figure 1-10-(b)) is a graphical representation method, which plots modulus of the impedance, $|Z|$, and phase angle, Φ, against frequency. In capacitor research, this plot is useful to investigate loss tangent, *tan* δ, which is calculated from *tan* (90-Φ) (derived from equation 1-23). Thus, via Bode plot, we can estimate the dielectric loss tangent of specific frequency.

1.3.4.3.1.2 Series R + parallel R | C circuit

In the electrochemical cell system, the ion-conductive electrolyte acts as a medium to transfer charge between the anode and cathode. Therefore, the resistance of the electrolyte must be considered. Assuming that a homogeneous and uniform film is formed in the electrolyte on the metal substrate, the equivalent model can be described by a parallel combination of a layer resistance, $R_{L,}$ and a layer capacitor, C_L, and it also includes the solution resistance R_S (Figure 1-11).

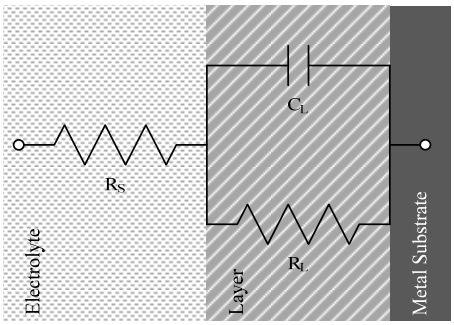

Figure 1-11. Equivalent circuit of R_S-(R_L|C_L)

It is called a "Randles" circuit, which is widely used for analysis of case that has an 3D single layer on metal substrate in ion-conductive aqueous solutions. Theoretically, the layer in the model could be an electrochemical double layer [38] [40] [41], painting or coating with organic materials for corrosion protection [43], and even a natural oxide layer [44]. The complex impedance is described as follows,

$$Z(j\omega) = R_{\mathrm{S}} + \frac{R_{\mathrm{L}}}{1 + (\omega R_{\mathrm{L}} C_{\mathrm{L}})^2} - j\frac{\omega R_{\mathrm{L}}^2 C_{\mathrm{L}}}{1 + (\omega R_{\mathrm{L}} C_{\mathrm{L}})^2} \tag{1-61}$$

That is, the semicircle in Nyquist plot always has additional contribution of the resistance R_L. Thus, phase angle, Φ, changes,

$$\phi = arc\,tan\left(\frac{Z''}{Z'}\right) = arc\,tan\frac{\left(\frac{R_{\mathrm{S}}}{2}\right)}{\left(\frac{R_{\mathrm{S}}}{2 + R_{\mathrm{L}}}\right)} \tag{1-62}$$

Figure 1-11 shows schematic diagram of both Nyquist and Bode plot for R_S-($R_L|C_L$) circuit [41] [40].

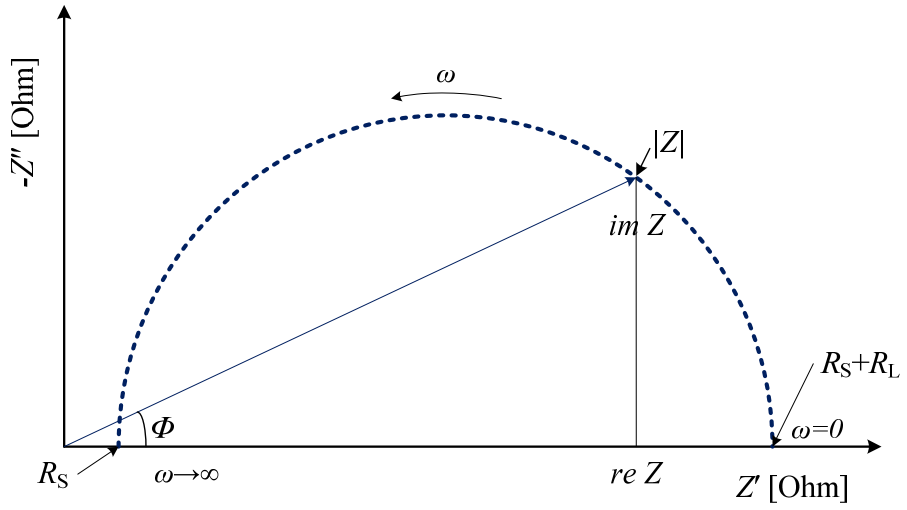

(a) Nyquist plot

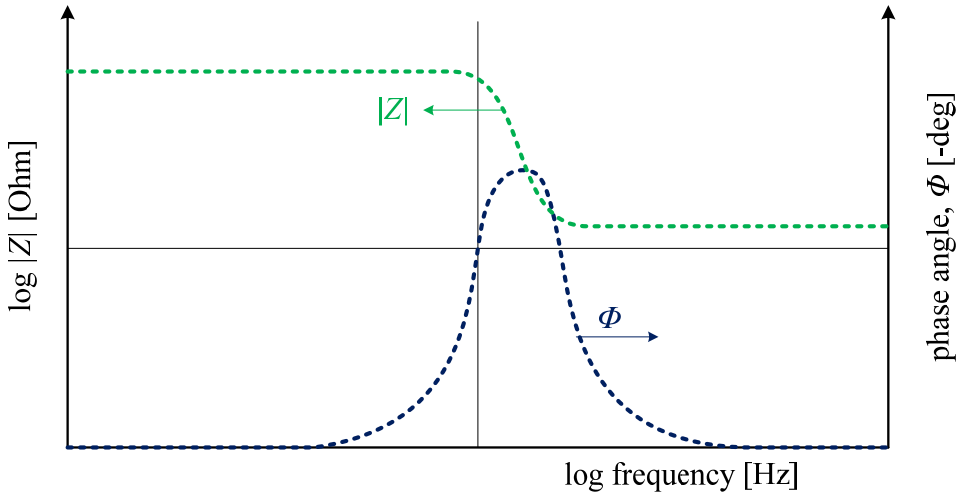

(b) Bode plot

Figure 1-12. Plots of the impedance vector for the R_S-($R_L|C_L$) circuit
(a) Nyquist plot, (b) Bode plot

From the Nyquist plot of the Randles circuit, $|Z| = R_S + R_L$ at $\omega = 0$, and $|Z| = R_S$, at $\omega \rightarrow \infty$. That is to say, we can calculate the solution resistance at high frequency as well as the layer resistance at low frequency. In the Bode plot, dielectric loss tangent can be estimated from the relation between the phase angle, Φ, and the loss angle, δ. From the case of Randles model in the figure 1-12, the plot shows resistive behavior ($\Phi = 0^o$ and $\delta = 90^o$) at both high and low frequencies, but partially capacitive behavior at medium frequencies. The relation between the phase and loss angle, and non-ideality of the circuit elements is discussed in the next chapter and also in the chapter 2 with practical examples.

1.3.4.3.2 Impedance Data for Non-Ideal Capacitor-Electrical Circuit Elements

In the practical electrochemical cell system, most of the capacitors' behavior does not always satisfy the theory of the ideal capacitor. It is influenced by the non-ideality caused by imperfection or inhomogeneous of the electrochemical response on the surface of the electrode. The non-ideality of dielectric is related to the equivalent series resistance (ESR) that is mentioned in the above chapter, which represents the real part of the impedance. If it is 0, the phase angle, Φ, is -90º, the loss angle, δ, is 0º, and the capacitor behaves like the ideal capacitor. On the other hand, large ESR leads small phase angle and large loss angle, and thus it has bigger dielectric loss tangent ($tan\ \delta$). It is described by a tilted or depressed arc on the Nyquist plot in figure 1-13.

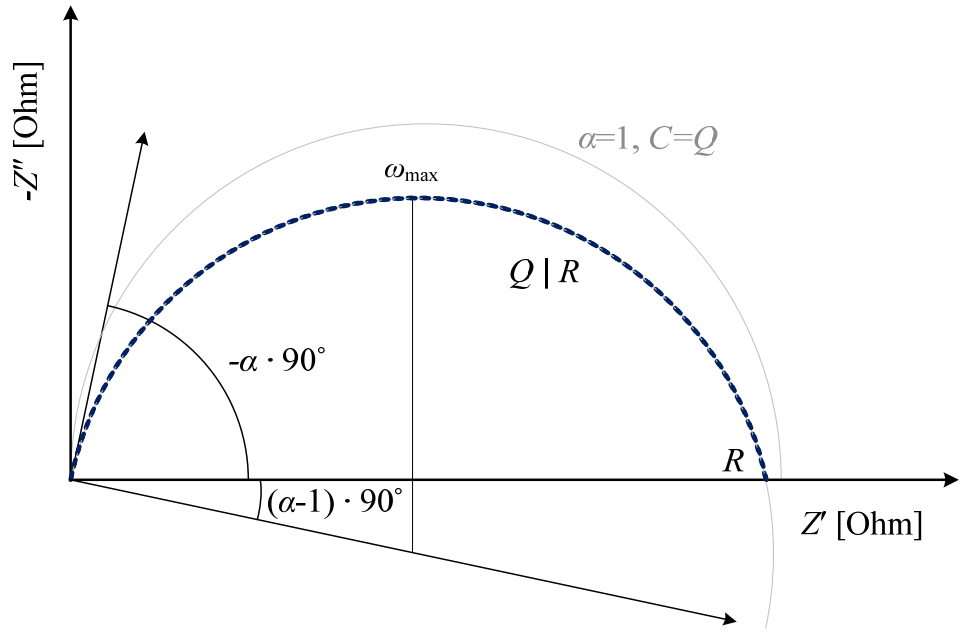

Figure 1-13. Nyquist plot of CPE(Q) | R circuits.

Considering the capacitor's non-ideality, a special electrochemical component of the equivalent circuit model, called constant phase element (CPE), is suggested to reflect the practical impedance data on the ideal equivalent model. The coefficient of CPE, Q_{CPE}, is defined as,

$$Z_{\mathrm{CPE}} = \frac{1}{Q_{\mathrm{CPE}}(j\omega)^{\alpha}} = \frac{1}{Q_{\mathrm{CPE}}\omega^{\alpha}}\left[cos\left(\frac{\alpha\pi}{2}\right) - j\sin\left(\frac{\alpha\pi}{2}\right)\right] \tag{1-63}$$

The unit is $ohm^{-1}s^{\alpha}$. α is the CPE exponent. If the exponent $\alpha = 1$, then, ESR is 0, the phase angle, Φ, is -90º, the loss angle, δ, is 0º, and Q_{CPE} equals the ideal capacitor, C_{ideal}. If $\alpha = 0$, then $Q_{CPE} = R^{-1}$, then which means that it would have response of the ideal resistor. With value of α=0.5, the electrode shows behavior of semi-infinite linear diffusion that is known as a Warburg impedance element in equivalent circuit. There is a relation between the CPE exponent, α, and the phase angle, Φ,

$$\Phi = -\alpha \cdot 90^{\circ} \tag{1-64}$$

The CPE exponent, α, could be converted to a degree of slant. In the case that $0.8 < \alpha < 1$, an effective equivalent capacitance, C_{eff}, can be estimated from the relation of Q_{CPE}, α and imaginary part of impedance, Z'', in the Nyquist plot [45];

$$C_{eff} = Q_{\mathrm{CPE}}(\omega_{max})^{\alpha-1} \tag{1-65}$$

ω_{max} is frequency where Z'' is at maximum. However, this equation cannot be used in the case of high capacitive film that the maximum peak for the Z'' value doesn't appear in the Bode plot [39] [46]. Brug et al. suggested another method to calculate a value of effective capacitance in the R-(R_1|C) circuit (Randles circuit) model [47]. Its application has been studied by several researchers for various oxide layers [48] [49] [50] [51] [52]

$$C_{eff} = Q_{\mathrm{CPE}}^{\left(\frac{1}{\alpha}\right)} \left(\frac{1}{R_1} + \frac{1}{R}\right)^{\left(\frac{\alpha-1}{\alpha}\right)} \tag{1-66}$$

Therefore using above equations, we can analyze the Nyquist plot and calculate effective equivalent capacitance, C_{eff}, in the equivalent circuit model for the given layer. Also, from the relation between the CPE exponent, α, and phase angle, Φ, change of dielectric loss tangent of the layer over frequency can be estimate.

Chapter 2 Electrochemical and Dielectric Properties of Anodic TiO_2 Layer on Pure Titanium Substrate

2.1 Introduction

Titanium is able to form a self-grown thin oxide on its surface when exposed to air or aqueous solutions. It is chemically passive and protects the titanium substrate as soon as a nm-oxide film is formed on the surface. It makes Ti or its alloys useful for a number of applications including for dental/bio materials [53] [54] [55] [56] [57], corrosion protection [58] [59] [60]. In solutions with ionic conductivity, such as sulfuric or phosphoric acid, the oxide layer can grow thicker than the initial natural (or native) oxide layer by application of an electric field. This is called “anodization”. An anodic oxide layer is more useful as a capacitor dielectric than the air-formed film because it can sustain higher voltage. It is a candidate for electric energy storages [4] [22] [23] [44] [61] .

One parameter that influences the energy density of a dielectric is its relative permittivity ε_r. It depends on the phase and structure of the TiO_2 phase. Its value varies from 7 to 160 [4] [5] [62]. The permittivity values for TiO_2 polymorphs are 110 for rutile, 48 for anatase, 78 for brookite [63] and a value of 13.7 has been reported for amorphous titania [64]. In comparison to other dielectrics on valve metals, such as Ta_2O_5 (ε_r =11~27.6), Nb_2O_5 (ε_r =41~46) and Al_2O_3 (ε_r =7.0~15) [5] [62], most TiO_2

phases have higher values and should be considered as an alternative dielectric for capacitor applications.

Table 2-1 lists the relative permittivity and band gap energies of various metal oxides reported by [4] [5] [62] [65]. In the figure 2-1 the oxide's band gap energies are plotted versus their relative permittivity. An inverse relation between the band gap energy and the relative permittivity is observed. That is, oxide with high band gap energy often has a relatively low permittivity, while oxide with small band gap energy often shows a high relative permittivity.

Table 2-1. Relative permittivity and band gap energy of various metal oxides [4] [5] [62] [65].

		relative permittivity (ε_r)	band gap energy (eV)
SiO_2		3.8-3.9	9
Al_2O_3		7.45-15	7-9.5
HfO_2		14-34	5.1-5.8
ZrO_2		12.3-31	4.6-8
Ta_2O_5		11.6-28	4-4.6
Nb_2O_5		41-46	3.4-5.3
TiO_2		7-160	3.2-3.8
	anatase	48	
	rutile	110	
	brookite	78	
	amorphous	13.7	

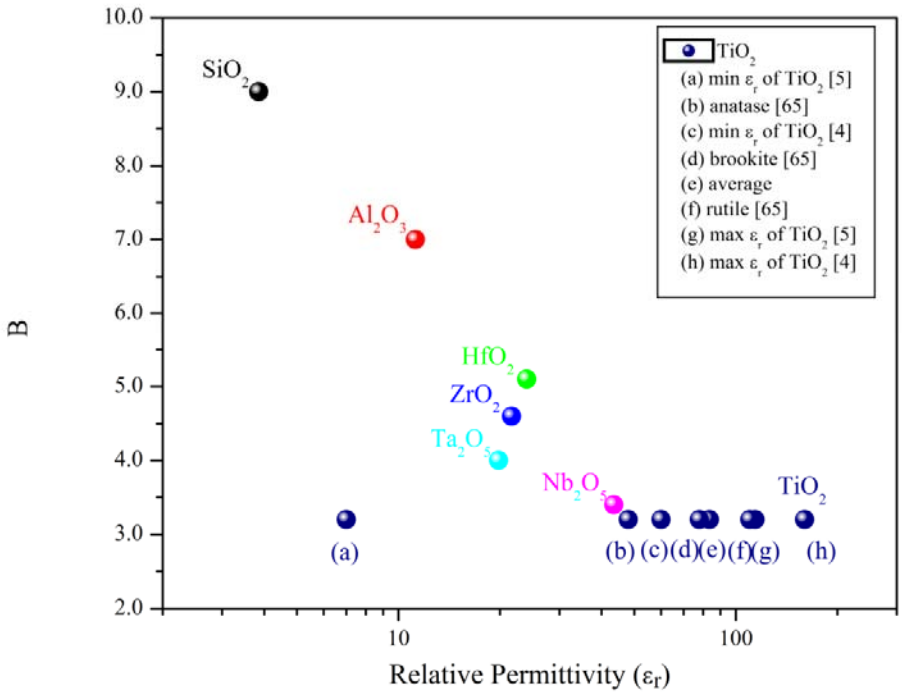

Figure 2-1. The band gap energies and the relative permittivities of various metal oxides [4] [5] [62] [65].

To obtain electric field strength and permittivity in anodic thin oxide film, appropriate anodization conditions are needed to generate the dielectrics. Numerous studies of the effects of anodizing conditions on morphology, microstructure and electrochemical behavior of anodic TiO_2 films have been carried out. For example, Shibata and Zhu [66] reported nanocrystallites in an amorphous matrix in a 9 V anodized TiO_2 film. Similar results have also been reported by Marsh and Gorse [67]. In

their TEM study, the oxide films were homogeneous as well as amorphous up to 10 V-anodizing potential. On the other hand, crystallized regions were found after anodizing to higher applied potential (84V) although there were still remaining regions of amorphous oxide phase. Lee and Pyun found crystallized structure at 20V and at 30V while they observed amorphous phase at 5V anodization [68]. Mantzila discussed a relation between anodizing potential and structure using results of Raman spectroscopy: oxide film formed by anodizing to 65V in H_2SO_4 solution resulted primarily in anatase phase, whereas at potentials below 10V the amorphous phase occurred [65]. According to TEM analysis by Mazzarolo et al., diffraction pattern of anodic oxide film formed by anodizing at 12V showed sharp rings mixed with broad rings, indicating a microstructure of nanocrystals in an amorphous matrix [69]. Jaeggi et al. discussed that crystallization occurred in a porous outer region while the inner region of the oxide film remained amorphous when 20V was used for anodization in H_2SO_4 solution [70]. Using Atomic Force Microscopy (AFM), Xing et al. observed a porous surface layer that consisted of crystallized nodules after 30V anodization [71].

Table 2-2. Structures of anodic thin films formed by anodizing at selected voltages

Authors	Max. Anodization Voltage [V]	Structure	Reference
Shibata et al.	9	nanocrystallites in amorphous matrix	[66]
Marsh et al.	84	crystalline structure with small amorphous	[67]
Lee et al.	5	amorphous	[68]
	20	crystalline structure	
Mantzila et al.	10	amorphous	[65]
	65	anatase	
Mazzarolo et al.	12	nanocrystallites in amorphous matrix	[69]
Jaeggi et al.	20	crystallized porous outer layer dense amorphous inner layer	[70]
Xing et al.	30	porous outer region by crystallized nodules	[71]

In summary, it appears that nanocrystalline structure is dominant at anodizing voltages above about 10V, however other factors may also affect the outcome (phase and microstructure) of the final anodic oxide film (Table 2-2). It appears that the anatase phase of TiO_2 forms mainly at higher anodization voltages. A comprehensive understanding of the growth mechanism(s) of titanium oxide film is not yet available, especially the time-dependent evolution of the oxide structure is not known. This is addressed in the present work by the preparation of thin oxide films by potentiostatic anodization. The electrochemical experiments (EIS) were used to comprehend how anodic titanium oxide grows as function of time. The oxide film phases, structures and morphologies were further characterized by optical and electron-microscopic analyses (SEM, TEM).

2.2 Experimental Procedure

2.2.1 Specimen Preparation

Commercially pure titanium (ASTM CP Grade 2; 99.2% purity, Table 2-3) was used as solid anode material. A rod of 2 cm diameter was sliced into several discs of 0.5 cm thickness. Small copper blocks were attached to back of each disc with conducting silver paste (Canemco). Each of discs with attached copper block was then mounted in epoxy resin (EpoFix resin, Struers) and cured in air for 24 hours. After mounting, a hole with a threaded connection was made through the epoxy resin into the copper block to make an electrical connection with the working electrode of an electrochemical cell (Figure 2-2-(a)). The free surface of the mounted specimens were consecutively polished with 320, 600, 1200, 4000 grit silicon carbide paper, then with 3, 1, 0.25μm powder and, finally, with a suspension of 0.05μm of Al_2O_3 particles on a polishing cloth for micro-polishing. Subsequently, chemical polishing was carried out using a titanium etching solution of 20:1:1 H_2O : HF (49%) : H_2O_2 (30%) : H_2O [72] for 10 seconds. The specimens were then cleaned with acetone in an ultrasonic bath for 20 minutes and rinsed with ethanol after wet etching. Then, as illustrated in Figure 2-2 (a), the periphery of the specimen surface was painted with sealant (Silicone Sealant, 3M) but leaving an exposed area of 1×1 cm^2.

Table 2-3. Chemical composition of CP grade 2 titanium

CP Titanium	Composition (max. wt.%)					
	Ti	C	Fe	H	N	O
grade 2	Bal.	0.1	0.3	0.015	0.03	0.25

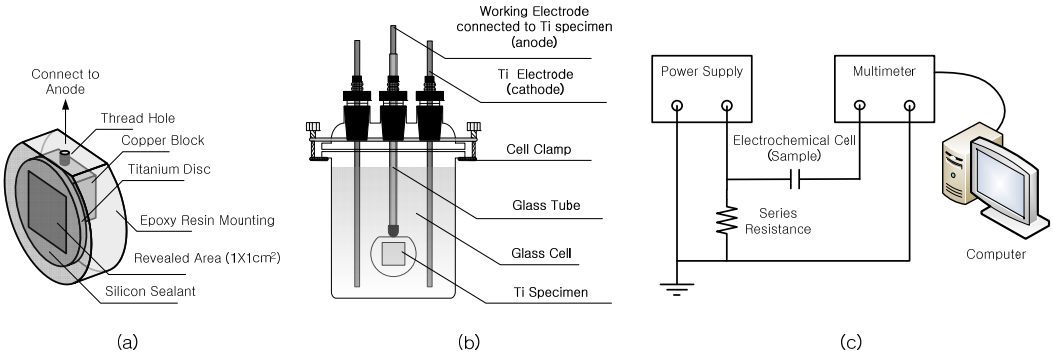

Figure 2-2. Schematics of specimen and electrochemical anodization system (a) of a specimen, (b) of an electrochemical cell containing the specimen (c) of a circuit for potentiostatic anodization and measuring current.

2.2.2 Anodization of Titanium and Electrochemical Studies of the Anodically Formed TiO_2 Dielectric

All electrochemical works in this study—anodization, dielectric/electric measurements, and electrochemical tests—were carried out in 1% H_3PO_4 solution (0.17M, 1.42 pH). The solution was used as the electrolyte of Ti-anodization in the several former studies with good performance of reducing leakage current [4] [22]

[23] [61] [73] [74]. A ‘two-electrodes’ system of working electrode (anode) and counter electrode (cathode) was used for anodizing (figure 2-2-(b)); pure titanium rods (0.5cm diamter×25cm length) were used for cathodes. (A ‘three-electrodes’ system was used for analyzing.) The potentiostatic anodization method was used to form anodic oxide film; constant potential was applied to the working electrode (anode) by a DC power supply. Current was measured and logged with a digital multi-meter (DMM 2000, Keithley) connected to a desktop computer (figure 2-2-(c)). Before anodization each titanium specimen was immersed into the anodizing electrolyte (1% H_3PO_4 solution) for two hours to measure the equilibrium potential at open circuit in the phosphoric acid solution. A potential of 30V was then applied at constant maximum current of 20mA between anode and cathode. Anodizing times of 9, 90, 300, 1500, 3600 seconds were chosen.

When the potentiostatic anodization was finished, electrochemical impedance spectroscopy (EIS) was performed to investigate electrochemical properties of the anodic oxide film. A potentiostat (PARSTAT 2273, Princeton Applied Research) was used. A traditional electrochemical cell with three electrodes system was used for the EIS measurements; graphite rods served as the counter electrode, and saturated calomel electrode (SCE) served as a reference electrode. EIS was performed on post-anodized specimens at the open circuit potential (OCP) with an amplitude of the perturbation signal being 10 mV at frequencies in the range of 10^{-2} to 10^{5} Hz. A software (ZView, Scribner) was used to analyze the impedance data and to fit them to an equivalent circuit model.

2.2.3 Method of Estimating Film Thickness of Anodic Oxide

To understand about relation between thickness and color of anodic oxide film color of anodized surface was observed. Using a digital optical microscope (LEICA DFC 450), images of specimen surfaces were obtained from a continuous (white) spectrum. The colors of specimen images were then compared with colors in a standard color chart of visible rays. From the 2D plane the interference wavelength can be approximately estimated, and afterwards, thickness of the oxide film was calculated from the approximate wavelength using equation for the relation of thickness and refractive index.

2.2.4 High-Resolution Investigation of the Surface and Cross-Section of Anodically Formed Oxide Films

Scanning electron microscopy (SEM; FEI Helios Nanolab 650) was used to investigate the surface morphology of the anodic films. Also cross-section changes of the oxide layers were measured on specimens sectioned with Focused Ion Beam (FIB). Platinum and palladium was deposited on the TiO_2 surface to protect the oxide surface during FIB work. After that, a cross-sectioned specimen was prepared by FIB milling and lifted out for Transmission electron microscopy (TEM) examination in a FEI Tecnai F30 instrument. High resolution bright field and dark field micrographs were taken and also selected area electron diffraction patterns were obtained.

2.3 Results and Discussion

2.3.1 Potentiostatic Formation of Anodic Film on Pure Titanium

Figure 2-3-(a) shows a schematic of the current density change during typical potentiostatic anodization. During the initial stage of anodization, stage-0 (zero), the current maintains its maximum limit while the voltage increases until it reaches the set maximum limit. During this stage the oxide film grows rapidly in thickness in proportion to the increase in voltage. It takes normally just few seconds to reach the limit voltage corresponding to the formation of the full oxide thickness. At this time the fully developed oxide begins the stage-I self-repair. During this stage the applied voltage is kept constant. The current decreases rapidly with a logarithmic time dependence, owing to resistance increase in the oxide film. Figure 2-3-(b) shows an actual experimental data curve of the current density change during potentiostatic anodization of pure Ti. The anodic oxide film was formed by 30V anodization. It reveals three different well distinguished stages showing how current density changes over anodizing time. Stage-0 is too short to be seen. The anodization current density dropped rapidly during stage-I (~90 seconds) of 30V anodization, reaching a minimum current density of 0.18 mA/cm^2. The titanium anodization treatment has additional stages-II and stage-III. During the second stage, up to 1500 seconds, the anodizing current density increased gradually until it reached a maximum current density of 3.2 mA/cm^2. During the final stage-III, the current density decreased slightly over time (~3600 seconds). As shown in figure 2-3-(c), five different titanium

specimens were anodized in the potentiostatic mode with each of them having a different anodization time. Dielectric and electrochemical properties were measured and analyzed for each after the potentiostatic oxide film formation. The results can be compared with the topography or microstructure of the oxide films as recorded by optical microscopy, SEM. and TEM.

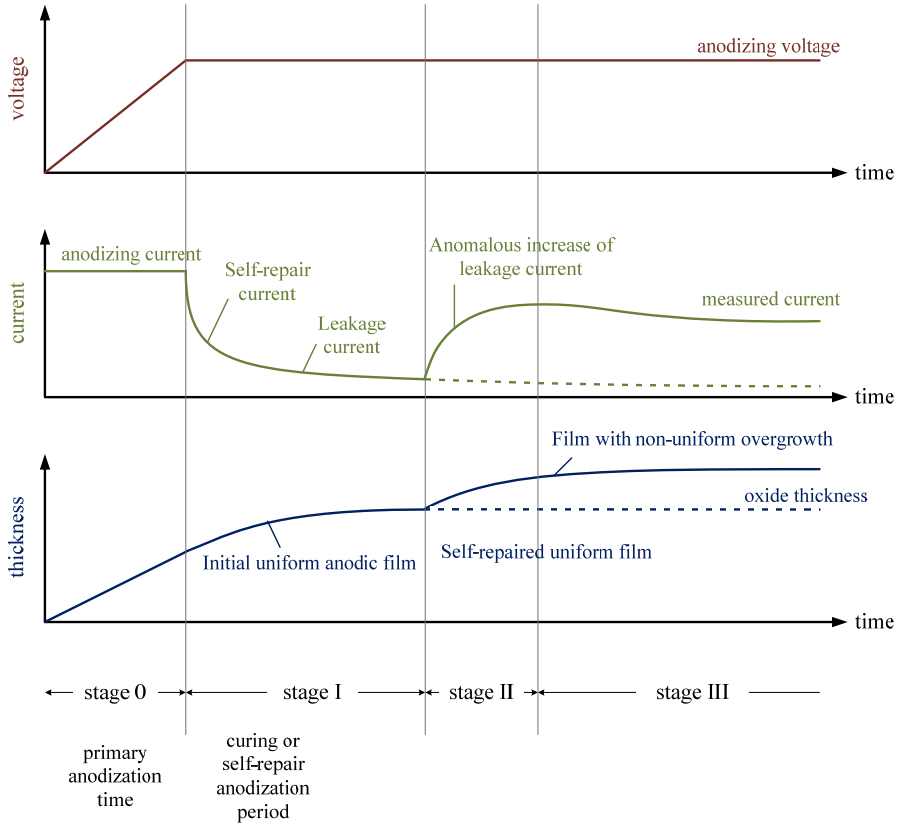

(a)

Figure 2-3. (a) Schematic graphs of voltage, anodizing of current and oxide film thickness during anodic oxide growth on titanium.

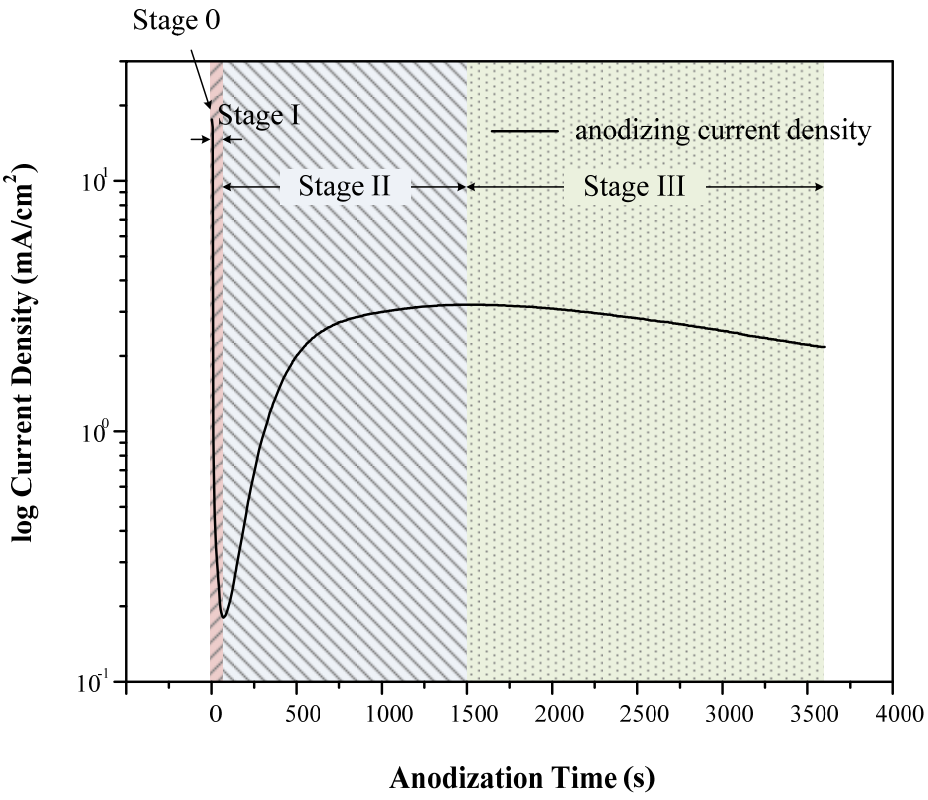

(b)

Figure 2-3. (b) Measured anodizing current showing a sharp drop of current density during stage-I film repair. In stage-II an anomalous re-increase of leakage current is due to localized formation of oxide islands containing crystal defects.

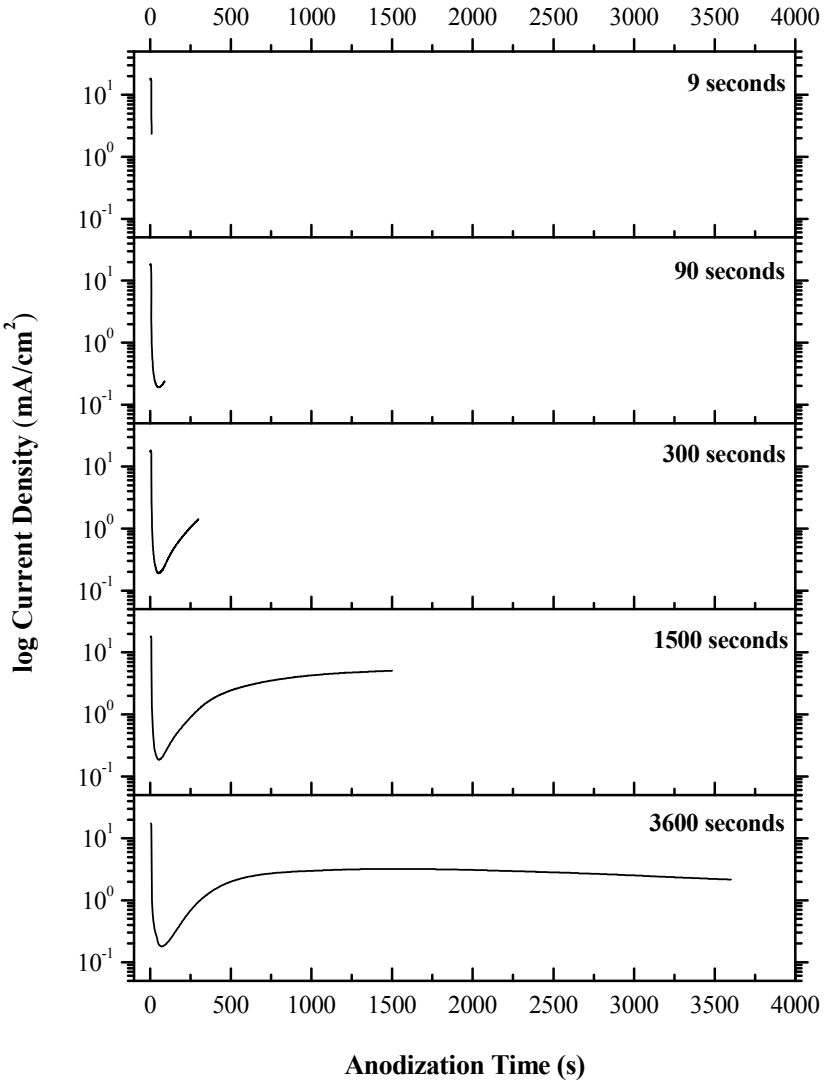

(c)

Figure 2-3. (c) Measured anodizing currents of five different titanium specimens; all show the formation of initially self-repairing oxide film and re-increase of leakage current due to permission along new current paths through newly-formed defective portions of the oxide film

2.3.2 Change of Interference Color and Growth of Anodic Oxide Films on Pure Titanium

Many metals and alloys that form thin passive oxide films on their surface show color change. It appears when incident white light (of continuous wavelength spectrum) is reflected at the air/oxide and oxide/metal interfaces, and a certain wavelength is omitted from the reflected spectrum because of destructive interference. This is known as thin film interference, which is a prominent feature of anodized titanium surface. The interference color is determined by thickness and refractive index of thin oxide films. Therefore, one can estimate thickness of anodic TiO_2 films from color of oxide film surface.

Assuming that the oxide layer is very thin, and uniform plane wave is incident on its surface (Figure 2-4), the optical path difference of the reflected light, Γ, can be expressed with refractive index of thin oxide film, n, as follows [75] [76];

$$\Gamma = \mathrm{n}(\overline{\mathrm{AB}} + \overline{\mathrm{BC}}) - \overline{\mathrm{AD}} \tag{2-1}$$

and,

$$\overline{\mathrm{AB}} = \overline{\mathrm{BC}} = \frac{d}{\cos\beta} \tag{2-2}$$

$$\overline{\mathrm{AD}} = 2d\tan\beta \cdot \sin\alpha = 2d\tan\beta \cdot \mathrm{n}\sin\beta \tag{2-3}$$

Collecting terms from equation 2-2 and 2-3, Γ is,

$$\Gamma = 2nd\left(\frac{1}{\cos\beta} - \tan\beta\sin\beta\right) = 2nd\left(\frac{1-\sin^2\beta}{\cos\beta}\right) = 2nd\cos\beta \qquad (2\text{-}4)$$

thus,

$$\Gamma = 2nd\cos\beta \qquad (2\text{-}5)$$

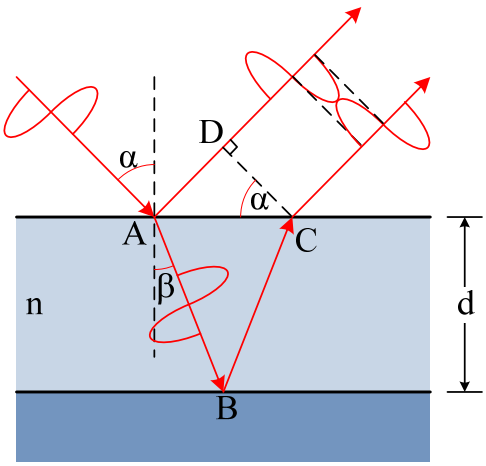

Figure 2-4. Illustration of destructive interference of a certain wavelength by reflection and recombination of light at the metal/oxide and oxide/air interfaces [77].

The characteristic color that depends on the thickness of the oxide layer will be represented by the absence of a specific wavelength of the reflected light from an oxide layer that has a certain thickness. If the angle of incident light equals zero (β=0), i.e., it is normal to the film surface, then reflected waves of certain wavelength will be completely out of phase, and interference of reflected wave will be destructive. Thus, for a given oxide thickness and refractive index the visible color is that of the continuous spectrum minus the interference-removed wavelength. The oxide film thickness, *d*, is able to be expressed with wavelength of complementary color from oxide, λ, [78] [79],

$$\mathrm{n}d = \left(\frac{2\mathrm{m}-1}{4}\right)\lambda \tag{2-6}$$

where m is the order of the interference and can be substituted by a certain integer. n is refractive index.

Several research studies about color-thickness relation of anodic TiO_2 films have been reported. Color of anodized film surface on titanium was blue and its thickness was about 80 nm when it was anodized at 30V [57] [76]. Halary-Wagner et al. reported that the interference color of anodic TiO_2 film changed from blue to light blue as its thickness increased from about 55 nm to 75 nm [80]. Karambakhsh and colleagues observed that oxide film thickness varied from 50 nm to 75nm when titanium was anodized at 30V depending on anodization solutions [81] [82]. It can be

inferred from previous studies that the interference color of anodic TiO_2 films formed by 30 V-anodization looks blue color, and its thickness is approximately in the range between 50 nm to 80 nm.

To understand color and thickness change of anodic oxide films during anodization interference color of each anodized titanium specimen was observed. It was compared with color of visible spectrum that can be approximately divided into six broad color regions; violet, blue, green, yellow, orange and red [83]. Approximate range of wavelength of complementary color was obtained from the comparison of observed color of oxide surface with the color spectrum. Refractive index, n, varies with oxide crystal structure. Due to the uncertainty of structure or crystallinity in the given thin anodic oxide film, the thickness range of the anodic TiO_2 film was determined from two boundary values of the refractive index, assuming that the thin film consists of amorphous and anatase phase; using the value of 2.2 for the amorphous and 2.56 for the anatase phase [84] [85] [86] [87]. Both air/oxide and oxide/metal interfaces were assumed to have low interfacial roughness in order to calculate the oxide thickness.

Table 2-4 shows change of interference color of anodic TiO_2 films formed on pure titanium during anodizing in 1% phosphoric acid solution at 30V applied potential. The observed color of oxide surface changes from blue to greenish blue. The complementary color canceled by destructive interference of specific oxide films changes from orange to reddish orange, and the approximate wavelength range of complementary color is 610 nm to 670 nm [88]. The minimum and maximum value

of oxide thickness by an approximate calculation is shown in table 2-4. Change of interference color shows that the anodic TiO_2 oxide grows during continuous anodization at 30V. To obtain more precise value of oxide thickness a numerical value of wavelength has to be measured by reliable methods and considered with other factors that can affect reflection and refraction of light, such as surface roughness, defects in the film [75].

Table 2-4. Change of color, wavelength and thickness of anodic titanium oxide film formed on commercially pure Ti during anodizing in 1% H_3PO_4 solution at 30V applied potential.

Anodizing time [seconds]	9	90	300	1500	3600
Color Chart*					
Color	blue ←——————————→ greenish blue				
Complementary Color [88]	orange ←——————————→ reddish orange				
Wavelength of complementary color [nm] [88]	610				670
Approximate thickness [nm]	60 ~ 69				65 ~ 74

*Optical micrographs of titanium surface anodized at 30V are shown in Appendix A.

2.3.3 SEM Analysis of Surface and Cross-Section of TiO_2 Films

To gain insight into the structural changes in the anodic titanium oxide films over time, the topography of the TiO_2 surface was studied by SEM (Figure 2-5). After the stage 0 and I of the potentiostatic anodization, a uniform flat oxide layer is observed with small oxide nodules or islands that were also observed in another study (Figure 2-5 (a), (b)) [71]. Each nodule starts growing up and spreading across the surface during stage-II (Figure 2-5 (c)). Bigger nodules can be observed; they cover more than half of the surface (Figure 2-5 (d)). Eventually the nodules cover the entire surface and form a rough upper layer (Figure 2-5 (e)).

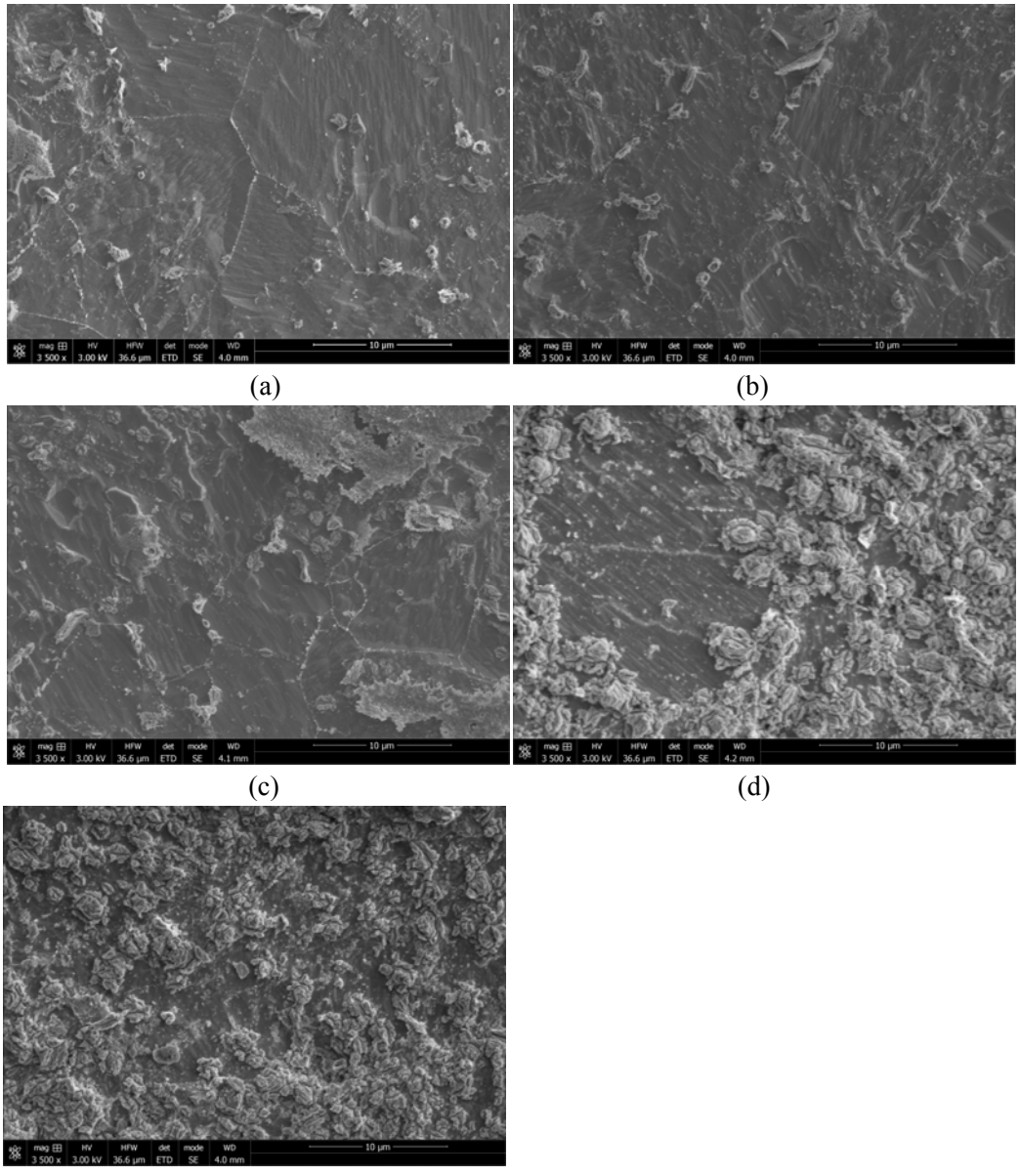

Figure 2-5. SEM images (3,500×) of the evolution of surface topography of anodic titanium oxide after (a) 9 seconds, (b) 90 seconds, (c) 300 seconds, (d) 1500 seconds, and (e) 3600 seconds of formation.

The topography change of the TiO_2 film surface is indicating an accumulation of new oxide due to ion transport forming part of leakage current. In the results of potentiostatic anodization in figure 2-3 (c), the rapid increase of the current density is observed at stage-II of the anodization when the nodules or islands grow and spread across the surface in the SEM images. Considering a logarithmic current reduction during anodization, the metal oxide grows homogeneously to form a uniform passive oxide layer. However, Ti shows abnormal current change during its anodization, forming nodules and islands rather than homogeneous and uniform passive oxide layers. It is related to repassivation of the anodic TiO_2 films, and the charge transfer for repassivation is counted as leakage current during anodization.

The cross-section of the oxide film was investigated in a transverse cut by focused ion beam (FIB) milling (Figure 2-6). Nodules (or islands) are observed after 1500 seconds of anodization (Figure 2-6 (d)(e)). The amount and size of nodules increase with increasing anodization time. The nodule size and shape are irregular and complicated. The oxide layer is turning more complex with nodules over time (Figure 2-6 (c)(d)(e)).

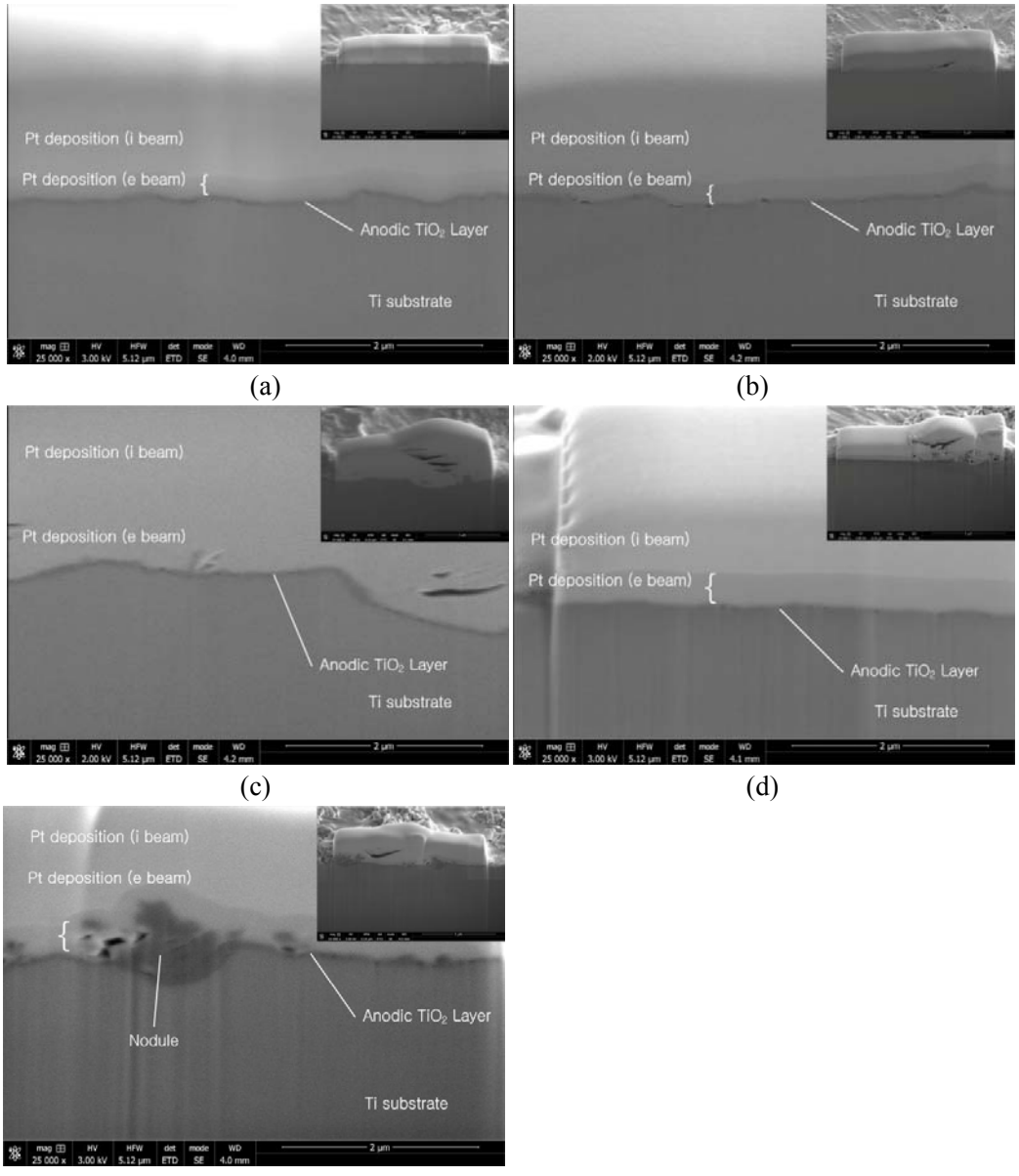

Figure 2-6. SEM images of cross-sections of anodic titanium oxide films after (a) 9 seconds, (b) 90 seconds, (c) 300 seconds, (d) 1500 seconds, and (e) 3600 seconds of formation.

2.3.4 TEM Analysis of Anodic TiO_2 Films

Transmission electron microscopy (TEM) was used for observation of structural change of the anodic TiO_2 layer. Two specimens were selected; 90 seconds (after stage-I) and 1500 seconds (after stage-II) of anodization. TEM micrographs are shown in Figure 2-7 with fast Fourier transform (FFT) results. The oxide layer seems to be uniform after stage-I and stage-II (Figure 2-7 (a)(b)). Nano-crystallized structures are found in figure 2-8 (c)(d), which shows lattice fringes clearly. On the other hand, it shows homogeneous amorphous structure near the outer surface (Figure 2-7 (e)(f)). The selected area diffraction (SAD) could not be obtained owing to crystallization; the amorphous phase crystallized and transformed to nano-crystalline structures during taking the SAD (The snapshots of movie clip of amorphous-crystal transformation are shown in Appendix B). The oxide consists of two sub-layers that have different structure; dense and homogeneous amorphous in outer layer and partially nm-crystallized inner layer. Thus from the results of SEM and TEM, it could be assumed that the homogeneous amorphous oxide is formed preferentially by initial anodic oxide growing before nanocrystallites appear in the inner sub-layer during the initial stage of anodization.

TEM micrographs of 1500-second-anodized specimen show more and larger region for nanocrystallites (Figure 2-8 (a)(b)), compared to the one of 90 seconds anodization. Lattice fringes are observed in the nanocrystalline region (Figure 2-8 (c)(d)), but there is still some amorphous phase (Figure 2-8 (e)(f)). One could say the 1500-seconds-anodized oxide film is one layer that has nanocrystals in an amorphous

matrix. However, big nodules are also found in the layer as it is shown in figure 2-5 (d), and figure 2-6 (d). TEM images show the nodule and its porosity in figure 2-9. It shows lattice fringes very clearly (Figure 2-9 (c)(d)).

Anatase TiO_2 was identified by the selected area diffraction (SAD) in figure 2-9 (e). Therefore, the 1500-seconds-anodized oxide has two layers; one layer contains an amorphous oxide matrix with nanocrystallites. The other layer is porous nodules or island-shaped anatase phase. The anatase nodules are evidence of a secondary anodic oxidation, namely, repassivation. They seem to be formed by self-repair during repassivation or during continued anodization. That is, the nanocrystals in the inner layer can be grown up and become a path of leakage current during anodization. It allows electronic and ionic migration in the oxide layer. This may occur repassivation of oxide layer occurs (Figure 2-9 (f)). It is represented as an increase of anodic current density in the time vs current density curve in the stage II (Figure 2-3 (b)), and possibly by a sharp current spike that was not recorded.

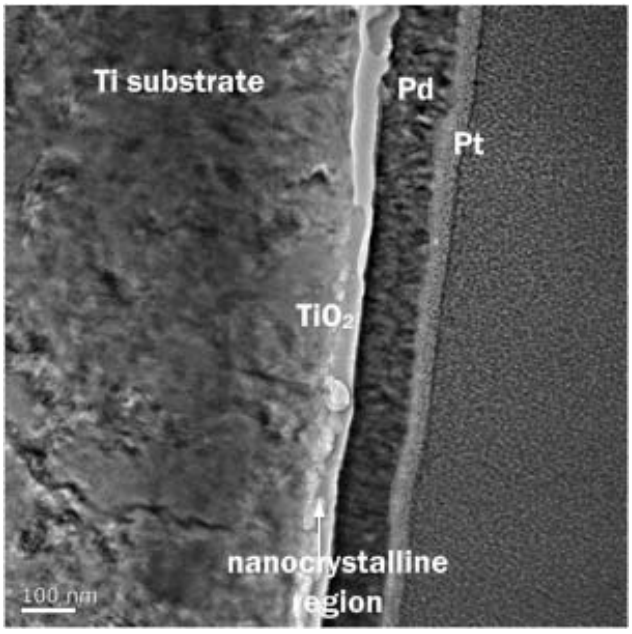

(a)

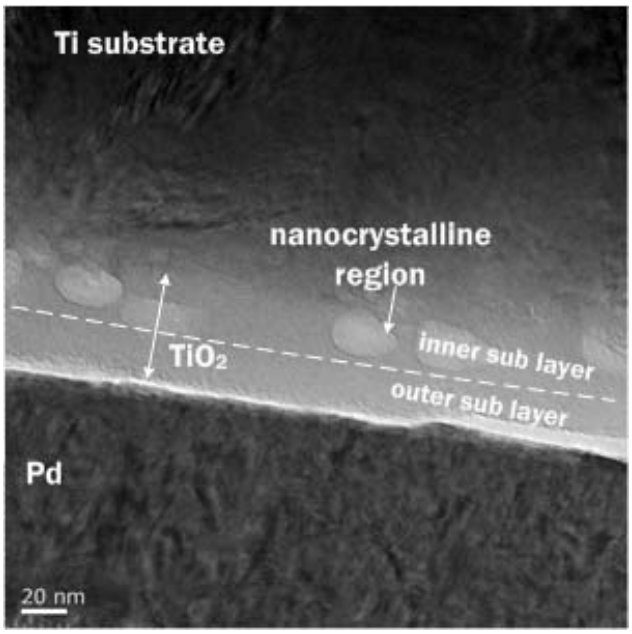

(b)

Figure 2-7. TEM images of the oxide film cross section formed after 90 seconds of formation; (a), (b) the cross section images of the oxide film

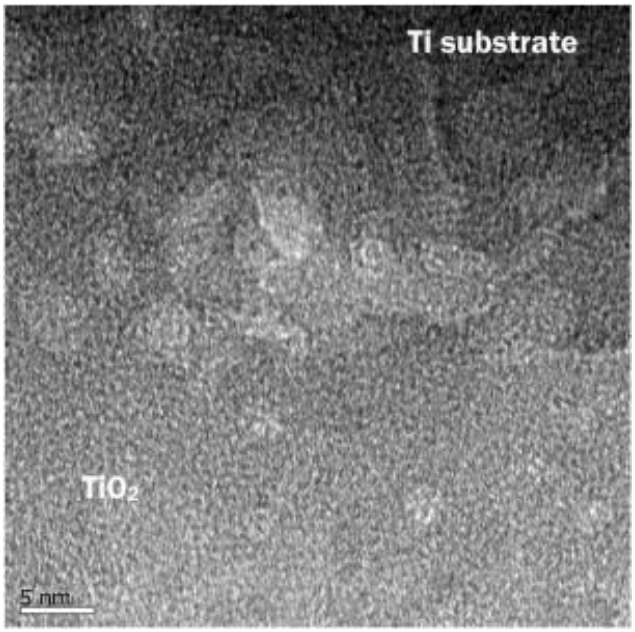

(c)

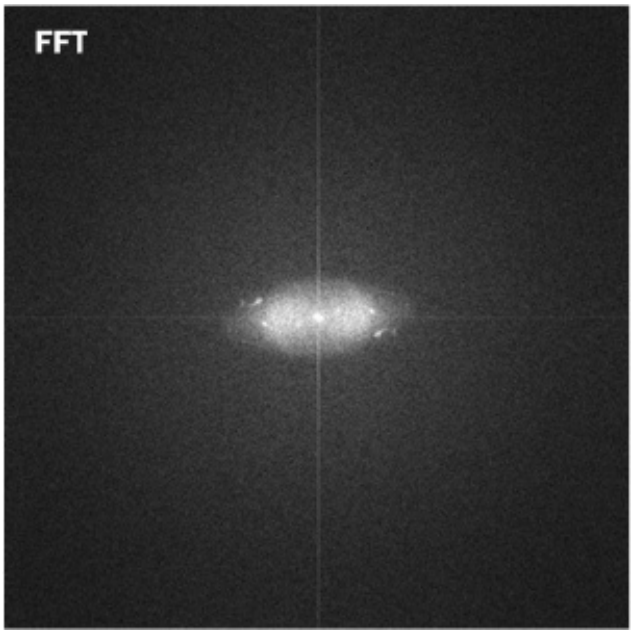

(d)

Figure 2-7. (continued) (c) the inner layer of the TiO_2 film shows lattice fringes and (d) a diffraction pattern by FFT method

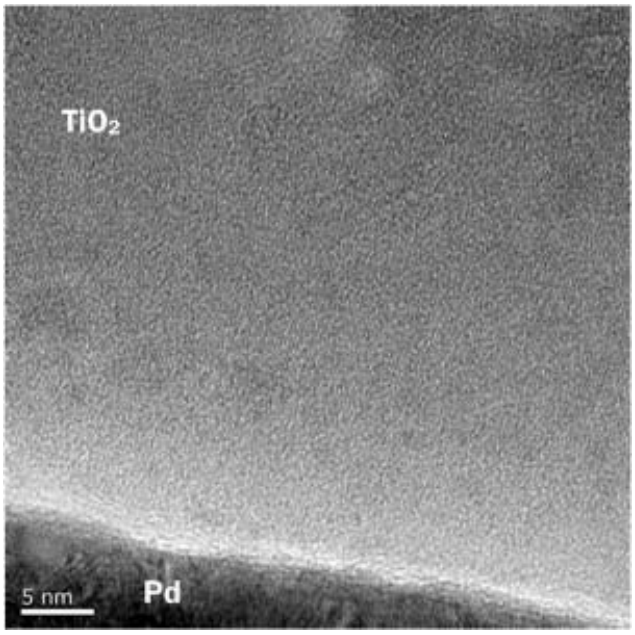

(e)

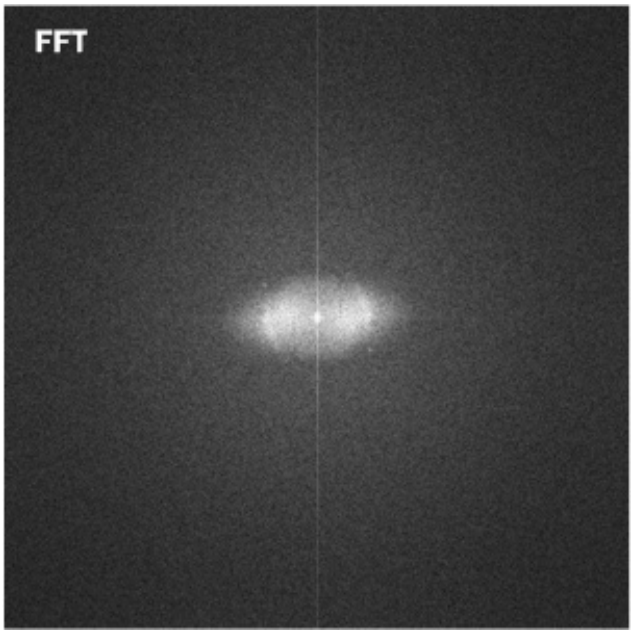

(f)

Figure 2-7. (continued) (e) the outer layer of the TiO_2 film,
(f) a diffraction pattern by FFT method

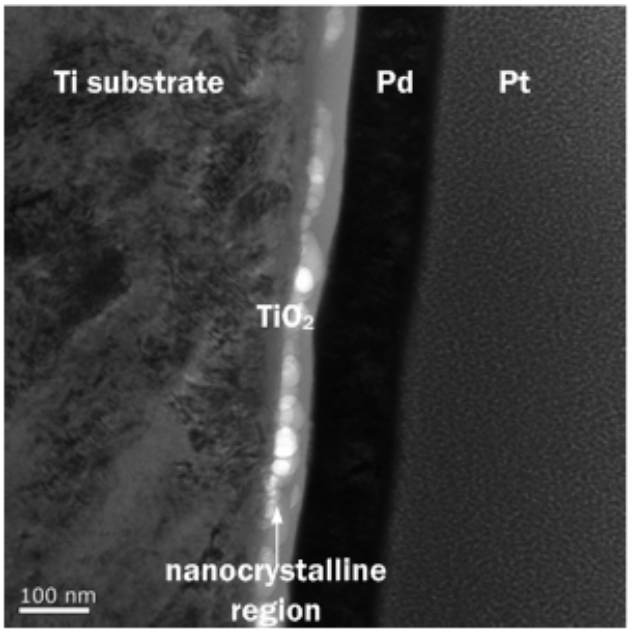

(a)

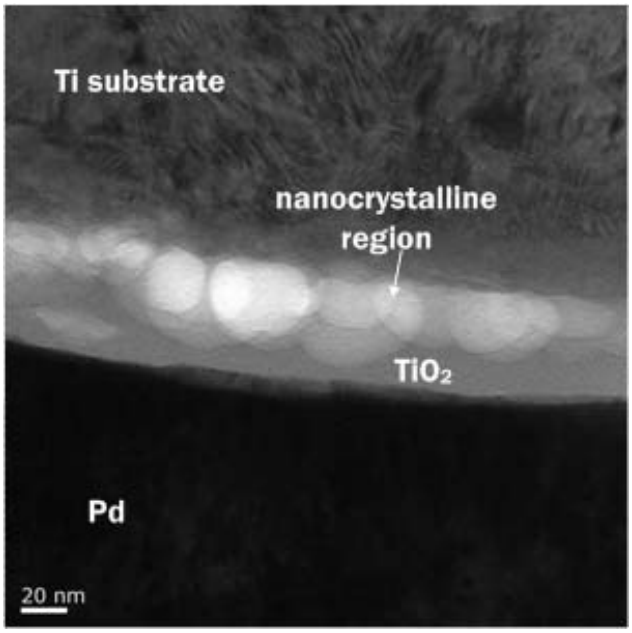

(b)

Figure 2-8. TEM images of the oxide film cross section after 1500 seconds of formation; (a), (b) the cross section image of oxide film

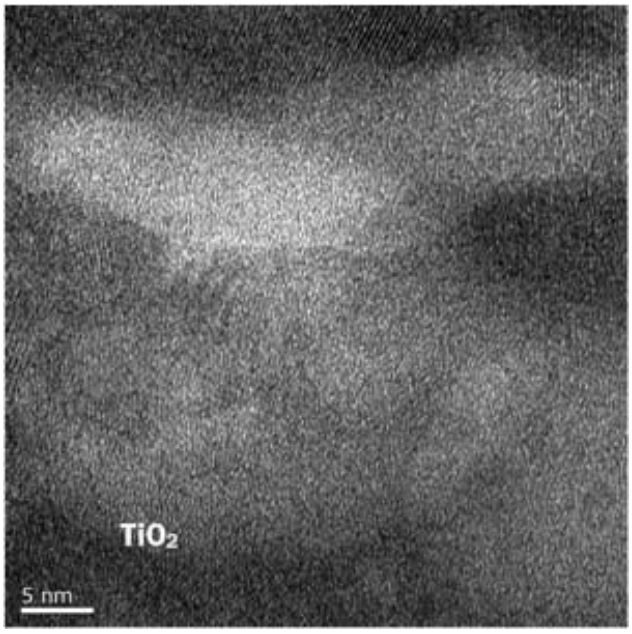

(c)

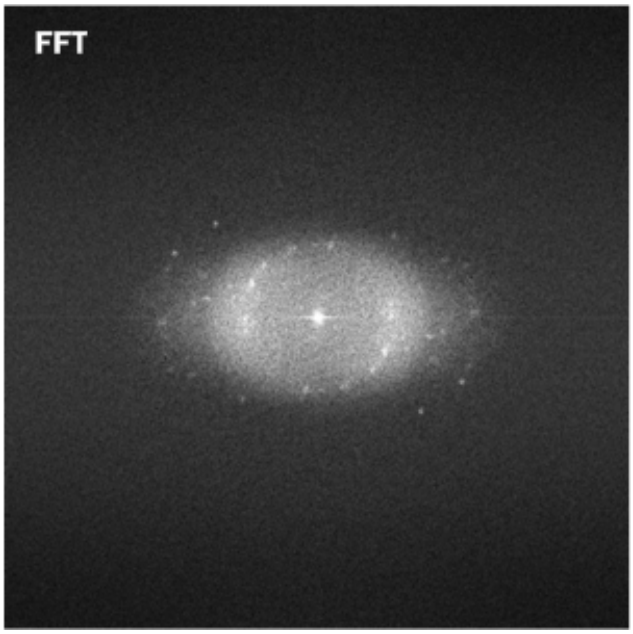

(d)

Figure 2-8. (continued) (c) low contrast features in the inner portion of the TiO_2 film, (d) a diffraction pattern by FFT method

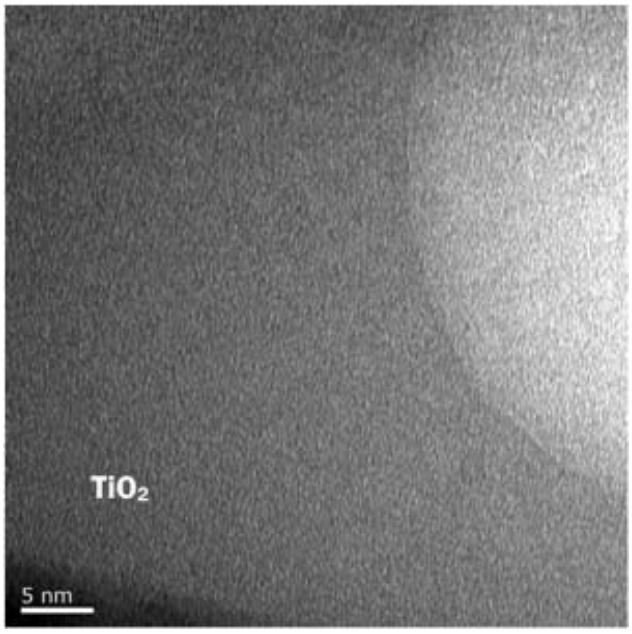

(e)

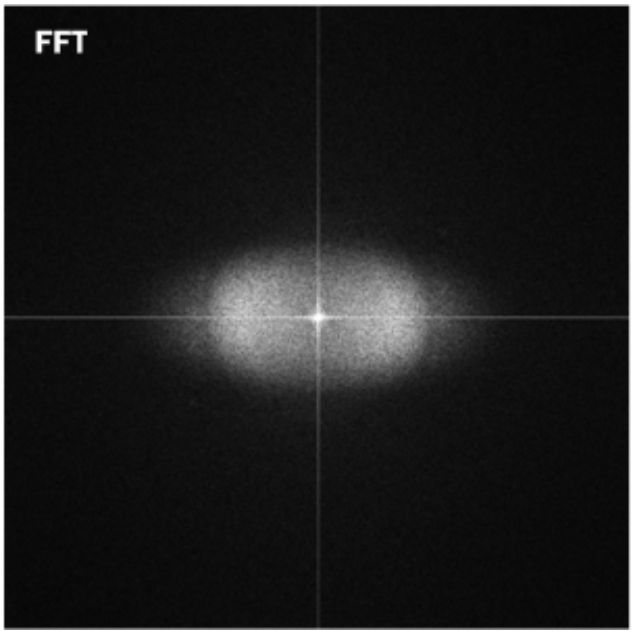

(f)

Figure 2-8. (continued) (e) relatively homogeneous part of oxide,
(f) a diffraction pattern by FFT method

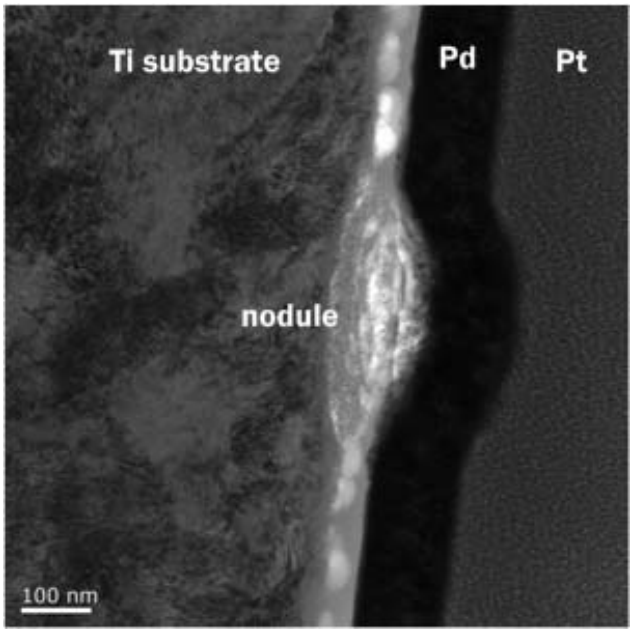

(a)

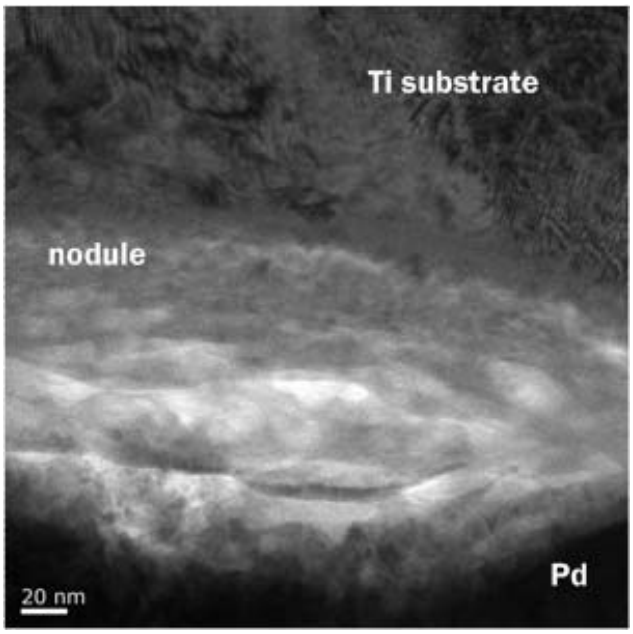

(b)

Figure 2-9. TEM images of the oxide film cross section after 1500 seconds of formation near nodule; (a), (b) the cross section images of oxide film

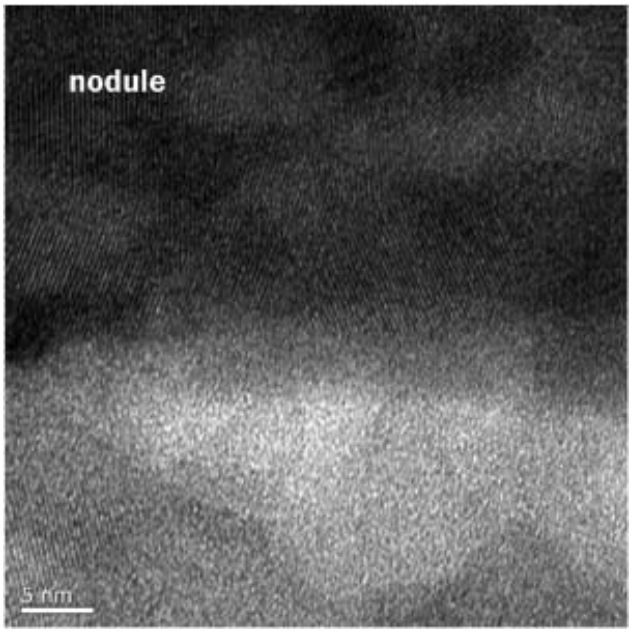

(c)

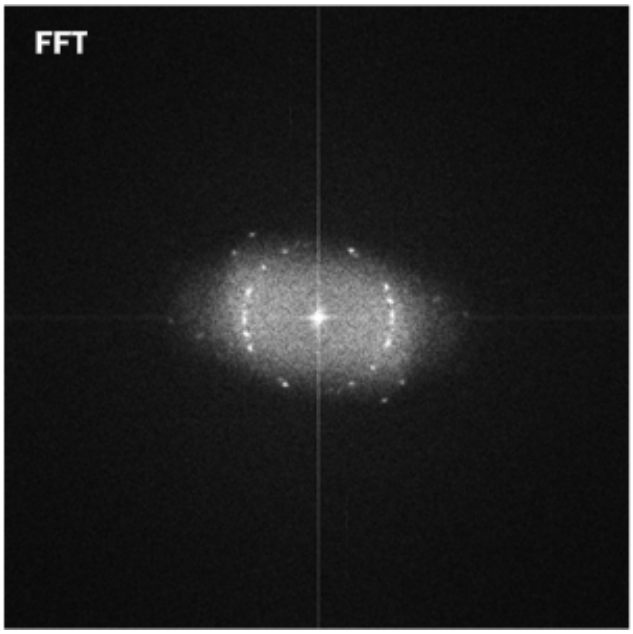

(d)

Figure 2-9. (continued) (c) a pattern of the crystallized nodule, (d) and a diffraction pattern by FFT method

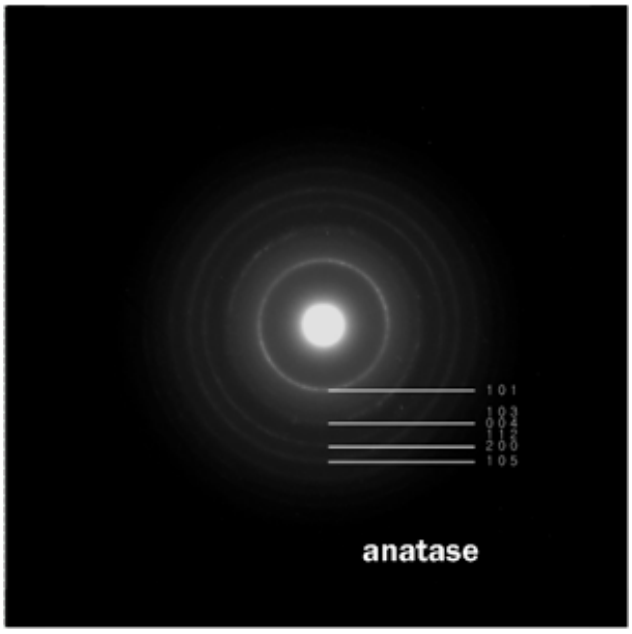

(e)

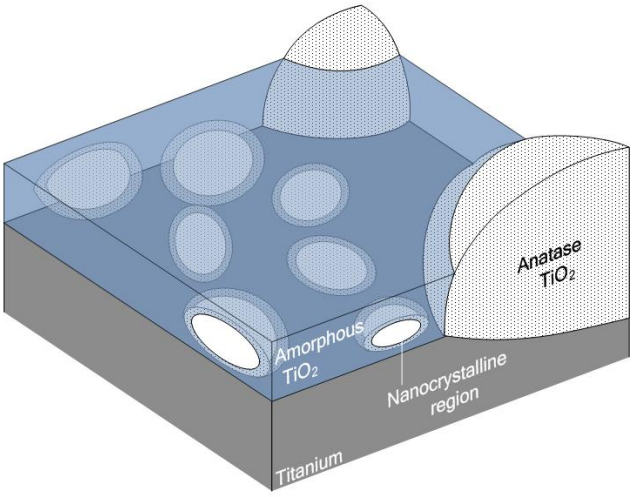

(f)

Figure 2-9. (continued) (e) selected area diffraction pattern of the nodule,
(f) illustration of anodic TiO_2 layer anodized after 1500 second based on TEM results;
nanocrytallites are in amorphous matrix with anatase nodules

Considering increase of size and amount of nanocrystallites, it seems there is a relation between crystallization and continuous anodization. According to Habazaki et al., crystalline nuclei of size about 1 nm at the oxide/metal which already present in the thin native oxide film contribute initial crystallization of amorphous oxide layer during anodization [91]. Shibata et al. reported that crystallization was induced near the metal/oxide interface owing to high internal stress during anodic oxidation [66]. It was also mentioned in other studies [89] [90].

In the present research, nanocrystalline regions were found in an amorphous matrix near the metal interface. It gives the appearance of two oxide sub-layers (Figure 2-10 (c)). After 90 seconds of anodization (stage II), some of the lump of nanocrystals are grown by high internal compression by volume expansion of oxide (Figure 2-10 (d)). Repassivation occurs and dissolved Ti cations form anatase titania crystal structure (Figure 2-10 (e)). This repassivation will continuously occur until the oxide surface will be covered by porous anatase phase nodules. This continued repassivation eventually results in complete coverage of the oxide with porous anatase nodules.

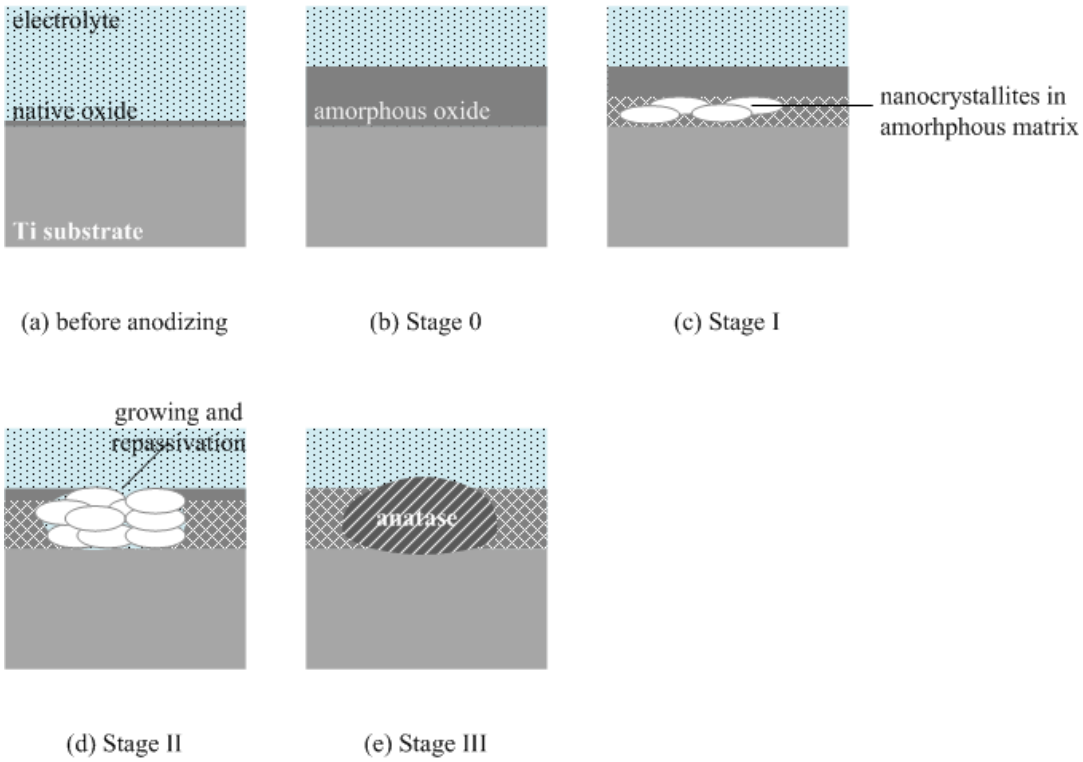

Figure 2-10. Model illustrating TiO_2 film growth during anodization

2.3.5 EIS Analysis of Anodic TiO_2 Films and Equivalent Model

In the EIS an oxide film shows ideal capacitive behavior, when the phase angle is -90˚. In the reality, however, it is not ideal. Thus, the closer the phase angle is to -90˚, the closer to the ideal capacitor it will be. The phase angle changes for different anodizing times. It is shown in the Bode plots in figure 2-11 (Nyquist Plots are shown in Appendix C). All plots for the anodic oxide layer exhibit two RC time constants with anodizing time, except the non-anodized specimen. The oxide layer that is naturally formed on pure Ti surface at the open circuit potential shows a single RC time constant. It represents a single layer. Two RC time constants represent two sub-layers in the dielectric film [38] [39] [40].

During stage-I of potentiostatic anodization (~90 seconds) the oxide films do not show clear capacitive behavior. A large phase angle is observed in the high frequency measurement region (f > 1 kHz) whereas a relatively small phase angle is obtained in the low frequency region. The phase angle decreases in high frequency region while it increases gradually in low frequency region for stage-II, anodic oxide grown for 1500 seconds. Finally, for stage-III, anodic oxide layer formed during 1500s to 3600s anodization shows a high plateau-like phase angle in the measurement region below 1 kHz region (figure 2-11). The phase angle is higher than 80˚ but did not reach -90˚ of a theoretically ideal capacitor. It means the oxide film eventually represents near-ideal-capacitive behavior in low frequency region after one hour of anodization [92]. Thus, one can conclude from the EIS results that the anodic titanium oxide film in phosphoric acid solution likely consists of two sub-layers—an inner and an outer

layer, and these layers show different capacitive behaviors during anodic oxide growth. The model is supported by the results of the electron-microscopic analyses.

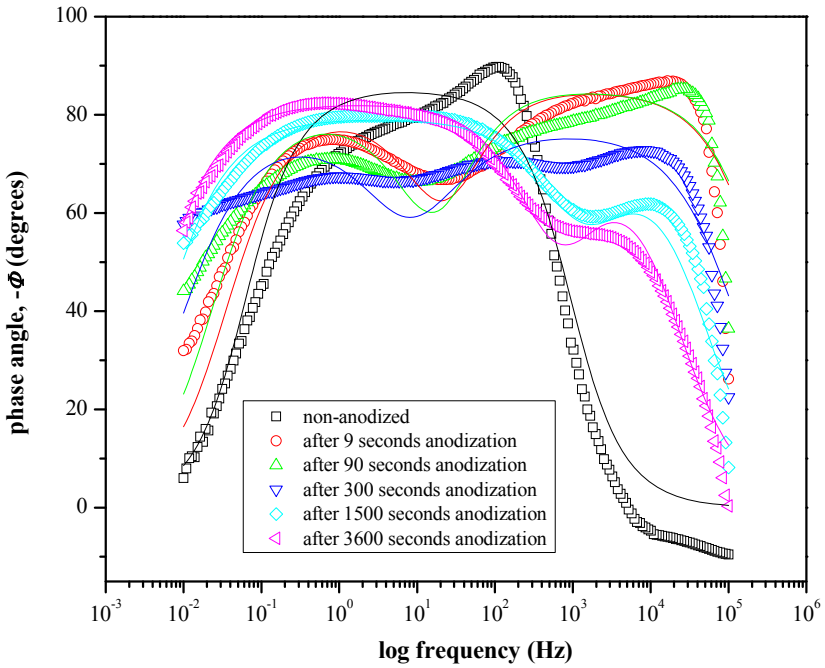

Figure 2-11. Bode plots for the anodic titanium oxide films after different anodizing time. The plots show the phase angle Φ as a function of applied charging/discharging frequency.

In order to explain electrochemical behavior of the anodic TiO_2 film, several equivalent circuit models have been suggested. The anodic oxide films with homogeneous structure can be represented by an equivalent circuit named Randles circuit model, R─(R│C) (Figure 2-12 (a)). The circuit model can be applied to the natural (or native) oxide layer. It is also used to analyze anodic films formed under conditions of low voltage anodization [44]. Badawy showed two RC time constants may be considered to explain the EIS results of a passive TiO_2 layer rather than a single time constant [13]. Equivalent circuit models with two RC time constants were considered to explain the complexity of the anodic film growth as well as the structural changes during prolonged anodizing time; they are series and nested circuits in figure 2-13-(b) and (c).

A constant phase element (CPE) was used to better describe the impedance data. Here, R_s is the resistance of the electrolyte solution, R_{outer} is the resistance of an outer oxide sub-layer, while R_{inner} is the resistance of an inner oxide sub-layer. Q_{outer} and Q_{inner} represent effective CPE coefficients of each layer. The CPE coefficient, Q_{CPE}, is used to describe imperfection of capacitive behavior or pseudo-capacitive depression factor, α in the Nyquist plot [93]. Recall the previous equation 1-63, regarding Q_{CPE},

$$Z_{\mathrm{CPE}} = \frac{1}{Q_{\mathrm{CPE}}(j\omega)^{\alpha}} = \frac{1}{Q_{\mathrm{CPE}}\omega^{\alpha}}\left[cos\left(\frac{\alpha\pi}{2}\right) - j\sin\left(\frac{\alpha\pi}{2}\right)\right] \qquad (1\text{-}63)$$

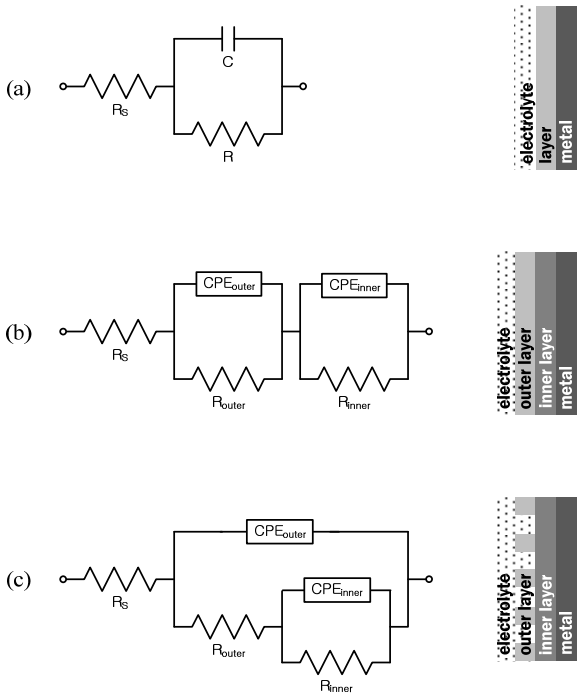

Figure 2-12. Equivalent circuit models used in this research
(a) equivalent circuit—"Randles circuit" for a general single-layer oxide system,
(b) two RC time constants connected in series, (c) nested two RC time constants

A combination of two parallel RC circuits is described in figure 2-12 (b). It showed the best fits for the oxide layer formed after 9 seconds and 90 seconds of anodization. It is in agreement with the TEM result that shows the oxide layer may consist of two sub-layers during stage-I; an outer mostly amorphous sub-layer and an inner sub-layer with nanocrystals in an amorphous matrix. The two parallel RC circuit model can also be used for fitting of 300 seconds-anodized specimen (stage-II) that has thin outer amorphous sub-layer and grown up nanocrystalline regions.

However, for oxide films formed during more than 1500 seconds of anodization,

the nested two-time-RC circuit model (figure 2-12 (c)) is more proper to analyze the impedance results. This model represents porous outer anatase nodules/islands and inner layer that is composite oxide of two phases, fully-developed nanocrystal phases in amorphous matrix. According to results of TEM, the two oxide sub-layers in early anodization become a single layer with increased volume fraction of nanocrystalline regions in amorphous matrix (Figure 2-9). Additionally, there are anatase nodules reaching all the way from metal to the outer surface, which can behave as a semi-porous outer layer in the impedance analysis of the stage-III anodic film.

Fitting results of each oxide layer and related equivalent circuit model are listed in table 2-5. These best-fitted values of equivalent circuit show how electrochemical properties, including resistance, depression factor, and capacitance, vary with microstructural change during oxide film growth by anodization.

Resistance for given area ($\Omega \cdot cm^2$) of anodic TiO_2 film can be expressed as a product of resistivity of the titanium oxide and its thickness ($(\Omega \cdot cm) \cdot cm$). Since resistivity is an intrinsic property that strongly depends on given material, it is determined by oxide phase. Amorphous oxide is generally expected to show higher resistivity than crystalline oxide phase due to the lacks of crystalline defects and grain boundaries [35]. Hanini et al. observed decrease of resistivity with developing anatase polycrystalline phase in the amorphous matrix [94]. It is associated with rising donor level more closely to the conduction band due to increase of the amount of TiO_2 oxygen vacancies, the main type of point defects in TiO_2 [95]. Expansion of nanocrystalline regions in the oxide layer during anodization decreases a ratio of

amorphous to nanocrystallites, and it results in decrease of resistivity of composite oxide. If anodic oxide layer keeps almost same thickness and transforms into nanocrystalline structure during anodization, measured resistance will decrease with decreasing resistivity. However, if oxide has same microstructural phase under constant temperature condition, then resistance will be a thickness-dependent property.

At zero seconds the resistance for given area of non-anodized specimen is about 9 $k\Omega cm^2$ (table 2-5). It is less resistive than the one in phosphate buffer saline solution, $\approx$100 $k\Omega cm^2$ [96] but more resistive than the one in sulfuric solution, $\approx$3 $k\Omega cm^2$ [97]. Resistance of non-anodized specimen at OCP is thought to depend on anodizing solution. The natural TiO_2 oxide formed in the air with a few nanometer-thickness [97] grows immediately after immersion into aqueous solution. When it is immersed into phosphoric acid solution, the open circuit potential and resistance are increased by forming and growing passive oxide layer [98]. Considering time needed for EIS test (about 0.5 hours), oxide layer on the non-anodized specimen could be thicker than natural oxide layer formed in the air, which results higher resistance at OCP.

Resistance increases rapidly during anodizing (table 2-5). As discussed above, the anodic TiO_2 layer during early anodization (stage-I) can be considered as two sub-oxide layers; outer amorphous layer and inner layer that has nanocrystalline phases in amorphous matrix. As anodic oxide layer grows, resistance of inner sub-layer increases during stage-I of anodization (1.62E+06 $\Omega cm^2 \rightarrow$ 2.27E+06 Ωcm^2). During this stage 'amorphous to nanocrystal' transition begins occurring near oxide/metal

interface. Despite of resistivity decrease during this stage resistance increases. It is thought to be due to increase of thickness by rapid growth of inner oxide layer. The minimum value of resistance can be associated with the results of potentiostatic anodization. After 90 seconds of anodization (stage-I) the measured leakage current during anodization reached a minimum value (Figure 2-3 (b)).

The resistance of inner sub-layer then decreases during stage-II anodization (2.27E+06 Ωcm^2 → 1.83E+06 Ωcm^2). At this point phase transformation occurred and formed many nanocrystalline regions in the amorphous matrix. It makes resistivity of composite oxide smaller, and thus resistance decreases in spite of thickness increase. The resistance is maintained at a relatively constant level during stage-III anodization (1.83E+06 Ωcm^2 → 1.68E+06 Ωcm^2 → 1.73E+06 Ωcm^2). During stage-III anodization most of the remained amorphous phase transform to nanocrystalline phase (or anatase) in the inner oxide.

Resistance change in outer oxide layer is more complicated. During stage-I it is remained as a homogeneous amorphous layer while inner oxide layer has nanocrystalline regions near oxide/metal interface (see TEM observations in figure 2-7 (e),(f), and illustration figure 2-10). The resistance increase due to the rapid oxide growth (3600 Ωcm^2 → 5100 Ωcm^2). However, it decreases after 300 seconds of anodization (5100 Ωcm^2 → 4500 Ωcm^2). It is because the nanocrystalline regions encroach upon the amorphous phase as they grow during anodization. After 1500 seconds of anodization (stage-III) resistance of outer layer drops rapidly showing relatively small value of resistance (4500 Ωcm^2 → 60 Ωcm^2 → 90 Ωcm^2). The

anatase nodules/islands are considered as an outer porous oxide layer by equivalent circuit model (table 2-5) that the electrolyte can penetrate through. Therefore the resistance of outer oxide layer is small.

The depression factor, α, indicates non-ideality of capacitive layer (equation 1-64) reflecting loss angle, δ (equation 1-23). It shows how coefficient of constant phase element is close to (or far from) ideal capacitor. Its range varies between 0 and 1 ($0 < \alpha < 1$). If the loss tangent (energy loss) of capacitive oxide layer is big, then, α will be small. It would become an ideal capacitor with $\alpha=1$, while perfect resistor with $\alpha=0$. When $\alpha=0.5$, it is defined Warburg impedance, which is used to represent semi-infinite linear diffusion of the electrodes. Mostly in many systems, the CPE element would be regarded as capacitors, if $0.8 < \alpha < 1$ [40]. Although all of the sub-layers show $\alpha > 0.8$ in the table 2-5, it varies with growth of anodic oxide and microstructural change. Particularly, the outer out-layers in early stage of anodization show $\alpha = 0.99$, i.e., they are almost ideal capacitors with very small energy loss. It is because the outer layers in early stage of anodization mostly consist of amorphous (figure 2-7). The α_{outer} value drops after 300 seconds-anodization as nanocrystalline regions develop and encroach on the outer oxide layer forming anatase nodules on top of existing outer oxide layer by repassivation. During stage-III of anodization, the oxide surface is covered with semi-porous anatase nodules/islands due to the continuous repassivation, and the α_{outer} now represents non-ideality of the porous outer oxide layers. They are relatively smaller than those of early anodization stage ($\alpha_{outer,\ 1500\ seconds} = 0.90$, $\alpha_{outer,\ 3600\ seconds} = 0.89$), which means the outer layers consist of

less ideal capacitor than amorphous, i.e., anatase TiO_2. Depression factors of inner oxide layer are less than outer oxide layer in early anodization stage because nanocrystalline regions are formed at metal/oxide interface during early stage of anodization. The value of α_{outer} increases and is maintained at a constant level (0.93) after 1500 seconds of anodization (stage-III). It is thought to be associated with its homogeneity. During stage-III anodization, most of the remained amorphous transformed to crystalline phase and made the inner oxide layer more homogeneous.

Change of effective capacitance of each sub-layer can be estimated from table 2-5. From the relation between Q_{CPE}, α, and the imaginary part of impedance, Z_{im}, an effective equivalent capacitance, C_{eff}, can be estimated. Hsu and Mansfeld proposed following equation [99];

$$C_{eff} = Q_{\mathrm{CPE}}(\omega_{max})^{\alpha-1} \tag{1-65}$$

ω_{max} is frequency when Z_{im} reaches maximum. However, this equation is not appropriate for films with high capacitance since it doesn't show a peak that represents maximum value of Z_{im} in Z_{im} vs. log f graph [100]. Therefore other equation for effective circuit capacitance was used in this research. Brug et al. developed following equation for R_1─(CPE │ R) circuit (Randles circuit) [101], and its application was widely studied by several researchers for various oxide layers [48] [49] [50] [51] [52].

Table 2-5. Equivalent circuit parameters for anodic growth of titanium oxide films changing with anodizing time; R_s is solution resistance. R_{outer} and R_{inner} are resistances of inner and outer oxide sub-layer. Q_{outer} and Q_{inner} represent effective CPE coefficients of each layer. α_{outer} and α_{inner} are depression factors of each layer. χ^2 is a goodness of fit.

Anodization Time [s]	Equivalent Circuit Model	R_s [Ωcm^2]	Q_{outer} [$\Omega^{-1}cm^{-2}s^{\alpha}$]	α_{outer}	R_{outer} [Ωcm^2]	Q_{inner} [$\Omega^{-1}cm^{-2}s^{\alpha}$]	α_{inner}	R_{inner} [Ωcm^2]	χ^2
0	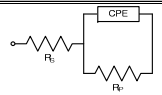	0.614				2.80E-04	0.99	9017	1E-2
9	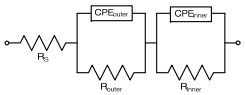	1.284	1.32E-06	0.99	3583	2.38E-06	0.91	1.62E+06	1E-2
90		1.293	1.17E-06	0.99	5088	2.49E-06	0.90	2.27E+06	2E-2
300		3.261	5.18E-06	0.85	4524	6.18E-06	0.85	1.83E+06	9E-3
1500	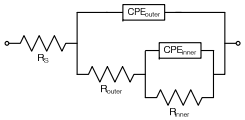	3.972	5.63E-06	0.90	64	5.87E-06	0.93	1.68E+06	2E-2
3600		4.071	6.57E-06	0.89	85	8.51E-06	0.93	1.73E+06	2E-3

$$C_{eff} = Q_{\mathrm{CPE}}^{\left(\frac{1}{\alpha}\right)} \left(\frac{1}{R_1} + \frac{1}{R}\right)^{\left(\frac{\alpha-1}{\alpha}\right)} \tag{1-66}$$

Assuming that the outer and inner oxide sub-layers are superposed, the total effective capacitance of anodized titanium dioxide layer can be obtained from the following equation [102];

$$\begin{aligned} \frac{1}{\mathrm{C_{total}}} &= \frac{1}{\mathrm{C_{double\ layer}}} + \frac{1}{\mathrm{C_{natural\ oxide}}} + \frac{1}{\mathrm{C_{inner}}} + \frac{1}{\mathrm{C_{outer}}} \\ &\cong \frac{1}{\mathrm{C_{inner}}} + \frac{1}{\mathrm{C_{outer}}} \end{aligned} \tag{2-7}$$

where $C_{double\ layer}$ is capacitance of the Helmholtz double layer that is potentially developed at the solid/electrolyte interface. $C_{native\ oxide}$ is the capacitance of the native oxide, and C_{inner} and C_{outer} represent the capacitances of the inner and outer oxide sub-layers. Because the capacitances of a double layer and/or of a native oxide are much larger than the capacitance of inner and outer oxide layers, their reciprocals are small enough to be neglected in equation 2-7 [102]; thus the inverse of the total capacitance can be calculated. It is approximately equal to the summation of the individual inverse capacitances of two anodic oxide sub-layers ($C_{total}^{-1} = C_{inner}^{-1} + C_{outer}^{-1}$). Table 2-6 shows the capacitances of outer sub-layer, inner sub-layer, and the net capacitance

of the anodic film. Initially effective capacitance of non-anodized specimen was about 256 μF, which is due to its very thin oxide. The net capacitance as well as the two sub-layer capacitances decreased during the early stage of anodization (~ 90 seconds). It is consistent with the resistance, leakage current and microstructure change. After the stage-I anodization, the oxide layer consists of amorphous outer sub-layer and small amount of nanocrystallites in amorphous matrix. At this point, the resistance was in maximum and leakage current density was in minimum. However, after 90 seconds i.e., at the lowest point of current density in figure 2-3 (b), the total effective capacitance increased again. It increased continuously up to about 1.3 μF with increasing anodization time. Capacitance of inner oxide layer continuously increases due to increasing nanocrystalline regions in amorphous matrix. After forming anatase nodules/islands on oxide surface capacitance of outer oxide layer increases. The total effective capacitance also increases while it was small during early stage of anodization because of the amorphous-based microstructure.

Table 2-6. Estimation of capacitance of two dielectric layers and total capacitance

Anodization Time [s]	C_{outer} [nFcm^{-2}]	C_{inner} [nFcm^{-2}]	C_{total} [nFcm^{-2}]
0	-	256000	256000
9	1151.5	1472.8	646.3
90	1020.9	1565.7	617.9
300	767.5	3346.7	624.3
1200	1700.2	3433.3	1137.1
3600	1914.5	4906.4	1377.1

Considering TEM results and meaning of used equivalent circuits for analysis, it can be concluded that amorphous to nanocrystalline transition occurs at metal/oxide interface during early stage of anodization, showing different electrochemical properties on the inner and outer region of anodic oxide layer. With continuous anodization, nanocrystalline region in the inner sub-oxide layer develops, and the entire oxide layer transformed into nano-crystals. Therefore, resistance of outer sub-oxide is high during early anodization and become very small due to porous nodules on the surface. On the other hand, resistance of inner sub-oxide is really high and constant since titanium forms thick oxide film on its surface.

2.4 Conclusions

The passivation current to grow an initial oxide film and the repassivation current to repair and grow more oxide were recorded during potentiostatic anodization in order to investigate micrsostructural and effective capacitance changes in anodic TiO_2 films. Anomalies were discovered, namely, the anodizing current decreases during the early repassivation, then it temporarily increases before it decreases during long-time anodization to a steady state leakage current.

SEM and TEM micrographs show that the TiO_2 oxide film is mostly amorphous initially, then quickly develops regions of recrystallized phase embedded in the amorphous parent phase. Electrically it behaves as an oxide consisting of two sub-layers, an outer amorphous layer and an inner sub-layer in which nanocrystals are embedded in the amorphous parent oxide. Void-like (light-contrast in TEM) features were also found with the nanocrystalline regions. The interpretation of whether they are voids or recrystallized oxide pockets having low electron absorption in TEM is inconclusive at this time. With increased anodization time, the inside layer grows, diminishing the outer amorphous. Regions where the voids reduce the voltage-bearing cross-section, e.q. by forming cracks in the oxide film, nearly instantaneous repassivation must occur, equivalent to rapid localized self-repair. However, the repaired nm-crystalline oxide continues with an unpredictably high leakage current. This represents an overall current increase during potentiostatic anodization.

Oxide nodules formed by repassivation consist of anatase phase. They form a non-uniform porous oxide on top of earlier formed dense anodic film. Thus, after such repassivation, the oxide layer exhibits two layers; an inner amorphous oxide matrix with nanocrystallites and an outer porous anatase phase.

Electrochemical equivalent circuit models were applied to describe the impedance results. In correspondence with the two sub-layers observed in TEM, two time constant models are used. They are consistent with the impedance results. The EIS data and fitting results show how the electrochemical properties change with the microstructural evolution. It is consistent with the evolution of the oxide layer from amorphous to nanocrystals in an amorphous matrix to a nanocrystalline sub-layer covered by porous and nodular anatase phase.

Chapter 3 Electrochemical and Dielectric Properties of Anodic Oxide Layer on Ti-Zr Binary Alloys

3.1 Introduction

Zirconium, one of the early transition metals, also can form chemically protective, passive thin oxide layer when it is in contact with air or aqueous solutions. Compared to anodic TiO_2 films, ZrO_2 has smaller relative permittivity and larger band gap energy [5] [62] [92]. It affects the electrochemical properties of the oxide layer on the alloy materials to which Zr is added. According to Santamaria, the band gap energy of the oxide film grown on the Ti-Zr binary alloy increases with increasing Zr content [103]. The oxide film on the binary alloy behaves like an insulator rather than a semiconductor. Also, reduction of the relative permittivity of the oxide layer is observed as Zr content concentration is increased [104]. Therefore, it is expected that the anodic oxide layer formed on Ti-Zr alloy has lower leakage current density than the one on pure titanium.

The electrochemical advantages of the Ti-Zr alloys have attracted considerable attention since the mid-20th century. The initial studies focused on the effect of Zr content in the Ti-Zr binary alloy on corrosion resistance of the passive oxide film. According to Andreeva and Glukhova, zirconium is a very effective alloying element for titanium alloys to reduce corrosion rate and increase corrosion resistance in HCl based solutions [105] [106]. Results of potentiostatic polarization and galvanostatic

tests show that the corrosion resistance of the Ti-Zr binary alloys increased with increasing Zr contents. However, severe pitting corrosion occurred on the surface of the binary alloys that have Ti concentration less than 50%. Only the binary alloy containing 50% of Zr contents and 50% of titanium showed low current density over a wide range of potential. Thus, the researchers concluded that near-stoichiometric Ti–50at.%Zr is the most interesting alloy to form a passive oxide layer. Olivera et al. [107] also reported that Ti-50at%.Zr alloy had high corrosion resistance in physiological solution, and the passive oxide film of the alloy was even more resistant to fitting corrosion by chloride ions. Clearly, the existence of Zr atoms in the anodic passive oxide layer is helpful to improve the corrosion resistance. Ti-Zr alloys have been applied to bio and dental materials, owing to their high corrosion resistance and biocompatibility [24] [107] [108] [109] [110].

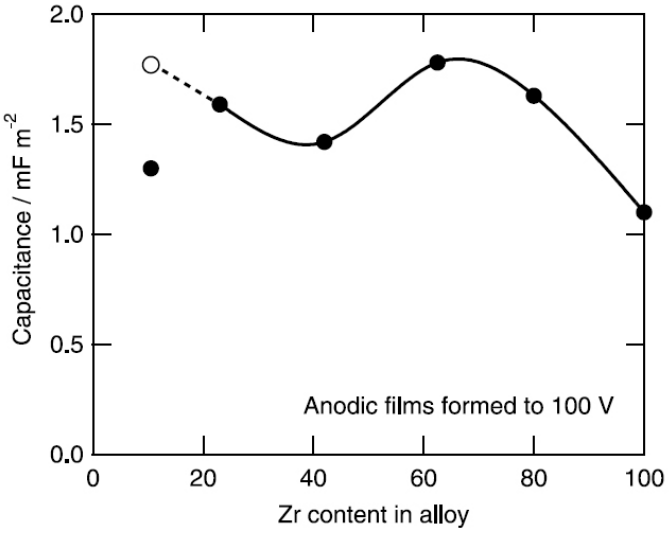

Figure 3-1. Dependence of capacitance on composition and relative permittivity of the anodic oxide layer formed on sputtering-synthesized Ti-Zr alloys formed in ammonium pentaborate solution [111].

Habazaki et al. reported on the structure and dielectric properties of the passive oxide film on Ti-Zr alloys prepared by high voltage (100 V) anodization in ammonium pentaborate electrolyte [91] [111]. In their TEM analysis, the anodic oxide layer showed amorphous structure in alloys with low Zr-content. With increasing Zr-content in the alloy, ZrO_2 nano-crystals (with monoclinic structure) were observed in anodically formed oxide films. They were embedded in an amorphous oxide matrix. Thus, the anodic oxide film on such alloys consists of two phases. The crystalline phase grew with added zirconium, and eventually the

oxide showed a fully crystalline structure on alloys with high Zr contents. Alloy with around 62.5 at.% Zr concentration produced an oxide with a high value of relative permittivity (ε_r =42) (figure 3-1). It was reported that Ti may have a role as a stabilizing cation to increase the relative permittivity of monoclinic zirconia in similar way to other cations such as yttrium, magnesium, calcium and cerium [112].

3.2 Experimental Procedure

3.2.1 Specimen Preparation

Ti-Zr binary alloy buttons with various concentration (Ti_{100-x}-Zr_x, x=0, 10, 20, 40, 50, 60, 80, 90, 100 at.%) were prepared from highly pure titanium slugs (≥ 99.98 %, Alfa Aesar) and zirconium slugs (99.95 %, metal basis excluding Hf, Hf of nominal 3%, Alfa Aesar) using a laboratory vacuum arc-melter with ultra high purity Ar atmosphere added. A chilled water-cooled copper hearth and tungsten rod cathode were used for arc-melting. The buttons were turned over and re-melted three times to obtain a thoroughly mixed composition.

The upper curved face of each button was ground flat, and a small copper block was attached to the ground surface with silver conducting paste (Canemco) (Figure 3-2-(a), (b), (c)). The buttons with the copper block were then mounted in epoxy resin (EpoFix resin, Struers), which was cured for about 12 hours. To make an electrical connection with the working electrode a threaded hole was made through the epoxy resin into the copper block (Figure 3-2-(d)).

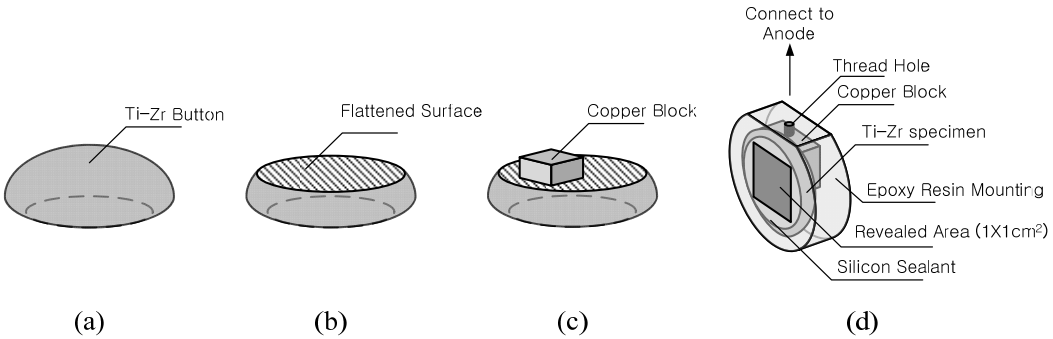

Figure 3-2. Schematics of specimen preparation; (a) a button, (b) polished upper curved surface, (c) attachment of a copper block, (d) a mounted specimen with threaded hole for electrical connection to the copper block

The mounted specimens were polished mechanically for electrochemical test. Silicon carbide papers with grit numbers (320, 600, 1200, 4000 grit) were used in this order. After the mechanical polishing, alumina powder suspensions with particle sizes from 3 μm to 0.05 μm were used for micro-polishing. Specimens were cleaned by ethanol in an ultrasonic bath for 20 minutes and then rinsed by ethanol. Specimens were painted with silicone sealant (Silicone Sealant, 3M) to expose target areas of $1\times1cm^2$ for electrochemical testing (Figure 3-2-(d)).

3.2.2 Anodization of Ti-Zr Alloys and Electrochemical Studies of (Ti-Zr)O_2 Anodic Oxide Films

Potentiodynamic tests were carried out. A potentiostat was used to apply a continuously increasing voltage starting at open circuit potential (OCP) to +10V_{SHE} of OCP. The scan rate was 0.166mV/s. The test was accomplished in the three electrode cell system with saturated calomel electrode (SCE) and graphite rod electrodes. Mounted Ti-Zr alloy specimens (Figure 3-2) were used as anodes for the test.

After the potentiodynamic test, the anodic oxide film was prepared on another group of the specimens by potentiostatic polarization at 30V. A schematic of circuit is shown in Figure 2-2-(c). During the anodization, the current response was measured and logged with a digital multi-meter (DMM 2000, Keithley) and a connected desktop computer. A two electrodes system was used, and pure Ti rods (Φ0.5cm×25cm) were used for the cathode. A 1% phosphoric acid solution (0.17M, 1.42 pH) was used as the electrolyte for the anodization process.

Each Ti-Zr alloy specimen was immersed into the phosphoric acid solution for two hours before anodization to measure the equilibrium potential at open circuit. A potential of 30V was applied to the working electrode (specimen) at constant current (max. 20mA) and was held for 3600 seconds.

Leakage current and dielectric loss tangent were measured after the anodization in the same electrolyte. The cell was switched to the two-electrodes cell with a titanium rods cathode. Leakage current was recorded as a singular value two minutes after re-applying voltage to the anodized specimens. The voltages for leakage current

measurements were 3V, 5V, 10V, 15V, 20V, and 30V. Capacitance was measured at 1 kHz with 6V DC bias using an LCR meter (Hewlett Packard model 4262A).

3.3 Results and Discussion

3.3.1 Potentiodynamic Tests

The results of potentiodynamic polarization tests on Ti-Zr alloys are presented. Figure 3-3 shows that the measured current density as voltage is increased from zero to 10 V_{ocp}. All specimens show passive behavior, i.e., they exhibit regions of constant current density called 'passive regions'. With little deviation, the values of current density of the specimens are in the range of 10^{-3} mA to 2×10^{-3} mA. The potential range of the passive region ranges from 0 V_{SCE} to about 1.3 V_{SCE}, where V_{SCE} is voltage measured by the saturate calomel electrode.

The electrochemical properties of the specimens changed in the transpassive region in which oxygen evolution occurs. At around $1.3V_{SCE}$, current densities of some specimens begin to increase. Especially, the current density of pure Ti increases rapidly as potential is increased. A measured current density is 0.27 mA/cm^2 when the potential reaches +10V. The specimen of pure zirconium shows a gradual increase of current flow. The final current density at $+10V_{OCP}$ is 0.01 mA/cm^2.

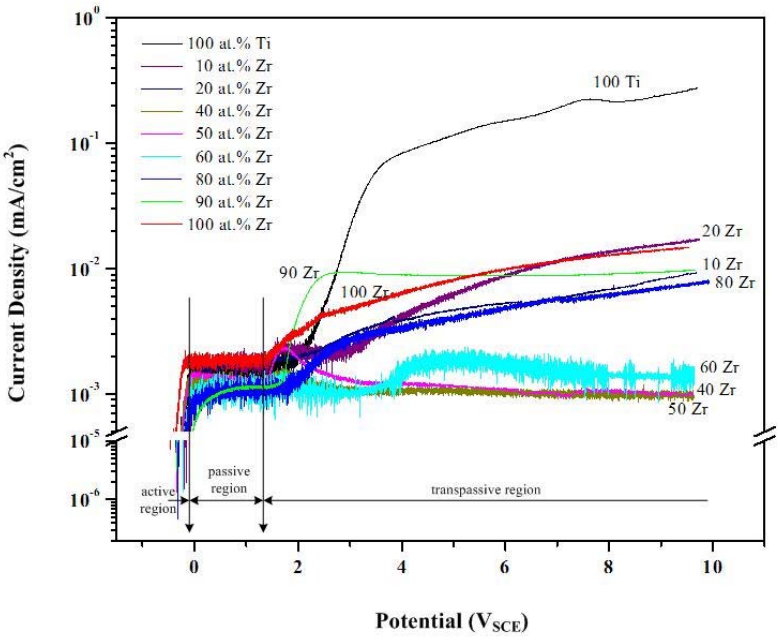

Figure 3-3. Potentiodynamic polarization curves obtained from Ti-Zr alloys with Zr contents from 0 to 100%

The binary alloys exhibit lower current density than pure titanium. The current density for anodization of pure titanium increases with increasing potential. The current density for the binary alloys in the transpassive region is decreased by the addition of Zr as an alloy element. The Ti-20 at.% Zr alloy shows lower current density than pure titanium and Ti-10 at.% Zr specimens. The lowest current density curve is observed from Ti-40at.% Zr specimen. It keeps its current density at a constant level with increasing potential. That is to say, only a small current (about 10^{-3} mA/cm^2) flows through the oxide layer on Ti-40 at.% Zr in the passive and even in the transpassive region. Ti-50at.% Zr and 60at.% Zr specimens also exhibit low

current densities during applied potentials. However, the current density for the binary alloy gradually increased at Zr-concentrations in excess of 80at.%.

Habazaki et al. reported that anodization ratio of (Ti-Zr)O_2 film decreased with increasing Zr content in Ti alloy or increasing Ti content in Zr alloy [91]. It showed a minimum value on the Ti-Zr binary alloy that has about 60at.% of Zr content. The anodization ratio (nm/V) is a coefficient that depends on applied anodizing voltage and oxide thickness [113]. Although the anodization ratio can also be affected by other anodizing factors, such as electrolytes, temperatures, etc. [113], we are inferring this is completely due to thickness variation if the applied anodizing voltage is constant. In Habazaki's study, lower anodization ratio of Ti-60at.% Zr alloy could be resulted from formation of thinner oxide layer in comparison with other Ti-Zr alloys. It is inferred that Ti-60at.% Zr alloy forms relatively denser oxide, which is associated with low current density of Ti-Zr alloys containing 40at.% to 60at.% Zr in potentiodynamic test results. It shows compositional effect on resistance of anodic oxide film on Ti-Zr alloy. The potentiodynamic results of this work are supported by previous studies that were performed under different electrochemical test conditions and electrolytes [105] [106] [107] [111].

The transpassive region in the potentiodynamic curve is related to oxygen evolution during the oxidation reaction [95] [114] [115] [116] [117] [118]. Theoretically, water dissociation or oxygen evolution reaction (OER) occurs on the anode surface at 1.229 V_{SHE} in aqueous solutions at pH = 0, at room temperature (chapter 1.3.2), see also equation 1-c,

$$H_2O(l) \rightarrow O_2(g) + 4H^+(aq) + 4e^- \quad (1\text{-c})$$

Electrolyte used in this study is 1% phosphoric acid, and its estimated pH is 1.42. Thus, using the Nernst equation (equation 1-24),

$$E_{O/OH^+,1\%\ \text{phosphirc acid}} = 1.229 - \frac{0.059}{4}\log\frac{1}{[10^{-1.42}]^4} = 1.145$$

The oxygen evolution reaction may occur at 1.145 V_{SHE} in this solution. Considering the relation between saturated calomel electrode and standard hydrogen electrode, the half cell reaction of saturated calomel electrode is [35],

$$Hg_2Cl_2 + 2e^- \rightarrow 2Hg + 2Cl^- \qquad (+0.241V_{SHE}) \quad (3\text{-a})$$

1.145 V_{SHE} is converted to 0.904 V_{SCE}. Oxygen evolution occurs, and the oxygen bubbles are observed on the anode surface at voltage over 0.904 V_{SCE} in 1% phosphoric solution at room temperature. The inflection point of current density in figure 3-3 is at around 1.300 V_{SCE}. This point is already beyond the potential of oxygen evolution condition in this solution ($E_{O/OH^+,1\%\ \text{phosphirc acid}}$ = 0.904 V_{SCE}). Oxygen evolution takes place on the anode surface, and the electron charges flow to

the cathode. In the figure 3-3 it is observed as an increase of current density.

Pure titanium shows passive behavior during the initial potentiodynamic anodization. At the high potentials (higher than the E_{O/OH^+}), the current density increases due to electric charge flow caused by oxygen evolution during the reaction. Some of the binary alloys, Ti-40 at.% Zr and Ti-50 at.% Zr, keep a constant current density even in the 'transpassive region'. The oxygen reduction reaction is less on the surfaces of the Ti-40 at.% Zr and Ti-50 at.% Zr binary alloys. Their oxides are more resistive and may be better dielectrics than the anodic oxides on pure Ti and pure Zr.

3.3.2 Potentiostatic Anodization of Ti-Zr Alloys and Measurement of Leakage Current

Figure 3-4 shows the results of current response versus applied voltage during potentiostatic anodization. They are similar to the results of potentiodynamic tests. Pure Ti specimen shows a high current increase during the secondary passivation. A logarithmic oxide growth behavior is observed for the Ti-Zr alloys with the current density dropping rapidly in the early stage of anodization and decreasing gradually in the later stage. The Ti-40 at.% Zr, Ti-50 at.% Zr and Ti-60 at.% Zr alloy show the lowest levels of current density. Combined with the results of potentiodynamic testing in 1% H_3PO_4 solution (Figure 3-3), one can conclude that the anodic oxide film on the 50Ti-50Zr binary alloy has the highest resistance and may be best suited as a dielectric.

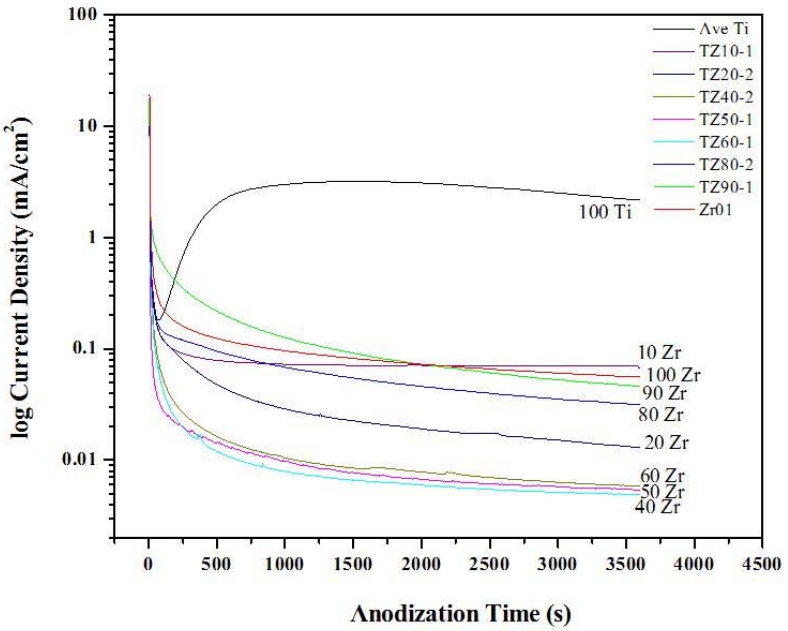

Figure 3-4. Potentiostatic polarization curves obtained from Ti-Zr binary alloys with various Zr contents

The results of measured leakage currents exhibit similar trends. The alloy with 50at.% of Zr shows the lowest leakage current (Figure 3-5). The leakage current through the oxide on pure Ti specimen is really high (about 2mA for a 30V-formed anodic film). On pure Zr the 30-Volts-formed anodic ZrO_2 film allows a relatively high leakage current while the Ti-Zr alloys show significantly reduced leakage currents.

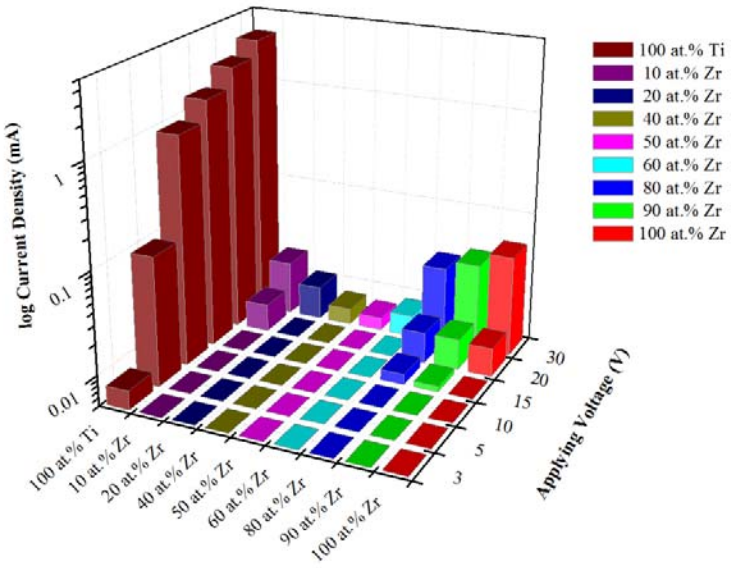

Figure 3-5. Leakage current through 30V-formed anodic oxide films on Ti-Zr binary alloys measured at full and derated voltages

The anodic oxides on Ti-40 at.% Zr and Ti-50 at.% Zr are more resistive than those of the other binary alloys. It may be due to the stabilized amorphous structure in the oxides formed on these alloys. In general, the low electron conductivity may be caused by the amorphous oxide structure. The amorphous anodic TiO_2 film has low anodizing current in its early stage of anodization (chapter 2). Habazaki et al., reported that the amorphous oxide can be formed on Ti-37.5 at.% Zr alloy. It can be assumed that the Ti-40 at.% Zr and Ti-50 at.% Zr specimen may also have developed the amorphous oxide film in a 1% phosphoric acid electrolyte. It is subject that merits further investigation.

3.4 Conclusions

Zirconium was used as an alloy element with titanium to increase the resistivity of thin anodic oxide on binary Ti-Zr alloy. A series of anodizing and leakage current measurements in DC potentiodynamic polarization, potentiostatic polarization experiments were performed to investigate the electrochemical properties of the anodic oxide films on binary alloys with various Zr contents.

The results that all Ti-Zr binary alloys as well as pure Ti and Zr show passive behavior at low potential, i.e., under about 1.3 V_{SCE}. However, in the transpassive region that is affected by oxygen evolution the anodizing and leakage current vary significantly. Whereas pure Ti exhibits a rapid current increase in the transpassive region, the oxide films on Ti-Zr alloys exhibit only a gradual increase with applied potential. In particular, the Ti-40at.% Zr and Ti-50at.% Zr alloys show little increase in current density, which means their oxides are good electric insulators and may be suitable as low-leakage-current dielectrics.

In potentiostatic polarization tests all Ti-Zr alloys as well as pure zirconium exhibit passive anodic oxidation; upon reaching the pre-selected anodization voltage (30V) the current drops rapidly with logarithmic time dependence. Ti-50at.% Zr showed the smallest passivation current, that is, its oxide has the highest resistivity.

Chapter 4 Synthesis of NM-Porous Ti-Zr Alloys

4.1 Introduction

The energy density of an electrolytic capacitor is controlled by the volume fraction of its energy-storing dielectric [119]. The dielectric is an oxide film formed by anodizing whose thickness is proportional to the anodizing voltage and inversely proportional to its dielectric strength. For a typical electrolytic capacitor, e.g., one that is anodized to 30 Volts, the oxide thickness is of the order of 50nm. To achieve a high volume fraction of such oxide film one must provide a metal substrate that is surface-enhanced and provides a large anodizable surface area. Optimal geometrical forms of capacitor anodes are in the range from thin films to interconnected thin fibers or fine-porous metallic sponges. In each case the cross-sections of the film, fibers or sponge branches must satisfy a minimum thickness on which a stable oxide film can be grown by anodic conversion of the metal's surface layer. Empirically, the metal substrate film or fiber or branch cross-sections should have a thickness between two- to ten-times the anodized film thicknesses. For the example of a 30V-anodized Ti-Zr alloy electrolytic capacitor, this means branch diameters of the order of 100 to 500nm. Additionally, to preserve paths for interpenetrating electrolyte an interconnected pore structure of similar dimensions is desired. A proven form for a capacitor anode is that of an open-porous,

interconnected metal sponge. Our objective was/is to synthesize such anode geometries of Ti-Zr alloy.

Sintering of fine-branched sponge-powder is one method to fabricate a porous structure. It is a process to fabricate metal or ceramic objects by bonding individual particles at their contact points by diffusion. At certain temperature, which is sufficiently high to bond but not to cause melting down, the particles contact and form necks at their junction by diffusion [120]. In order to sinter Ti anode material with high porosity, spacers materials such as polymers [121], salt particles [122] or other insoluble metals [123] [124] can be used to preserve interstices between the Ti particles. After sintering, the spacer substances are removed by vaporization or selective dissolution. The “spaces” that were occupied by spacers remain as pores. The pore size and the neck diameter of bonded Ti particles is influenced by factors of the sintering process such as temperature, time, and the amount and size of spacers used [125] [126] [127]. Sintering process is the process used in commercial fabrication of Ta capacitor anodes. The porosity as well as the size of the tantalum particle branches depends on the initial particle size of starting powder. To sinter nano-porous structure with high surface/volume ratio, one needs to start from metal-sponge particles that have nano or sub-micrometer size.

Calciothermic reduction can also be used to form a porous anode for the electrolytic capacitor. Since it is a pyrometallurgical process that reduces or extracts metal from metal compounds, pure surface-enhanced metal particles can be obtained. It is normally accomplished at high temperature using calcium's very high affinity to

oxygen. Titanium can be reduced from TiO_2 by calciothermic reduction;

$$TiO_2(s) + 2Ca(v) \rightarrow Ti(s) + 2CaO(s) \quad \text{(4-a)}$$

Fabricating Ti sponge anode for the capacitor by calciothermic reduction is based on the above reaction (4-a). Ki oxidized pure titanium wires in the air to form a polycrystalline TiO_2 layer on its surface. Subsequently, the oxide layer on the Ti wire was reduced by calcium in the hermetically sealed Ti retort [73]. Open porous structure of titanium was consequently formed on the titanium wire substrate. Chen used sintered porous Ti bar as a frame structure instead of titanium wires to obtain even higher porosity [74].

An electrochemical reduction process to extract pure Ti from TiO_2 is another option to synthesize the porous Ti structure. According to Chen and colleagues [128] [129], the externally applied potential can be a driving force of reducing TiO_2 in electrochemical cell system. They constructed electrochemical cell that can be heated up to melt $CaCl_2$ salt. Graphite rods were used as anode, and TiO_2 as a cathode. At the temperature of 900-1100˚C, calcium chloride was melted down and electrocalciometric reduction (reaction (4-a)) took place on the cathode; TiO_2 was reduced to form Ti sponge structure. Calcium oxide was also formed, and yet oxygen ionization occurs. Thus, it could be described as follows;

$$x\,CaO \rightarrow x\,Ca^{2+} + x\,O^{2-} \quad (4\text{-b})$$

$$x\,Ca^{2+} + 2x\,e^{-} \rightarrow x\,Ca \quad (4\text{-c})$$

On the anode, the oxygen ions produced from above reaction (b) had a reaction to produce either CO or CO_2 or mixture on the surface of carbon anode.

$$C + 2\,O^{2-} \rightarrow CO_2 + 4\,e^{-} \quad (4\text{-d})$$

$$C + O^{2-} \rightarrow CO + 2\,e^{-} \quad (4\text{-e})$$

Thus, the net reaction for the electrochemical reduction process to synthesize Ti sponge structure is,

$$TiO_2 + C \rightarrow Ti(s) + CO_2(g) \quad (4\text{-f})$$

Therefore, from the electrochemical reduction process, pure titanium can be obtained. Chemical conversion of halides could be one of the methods to extract pure titanium metal. Since Kroll proposed the very effective pyrometallurgical process that was named after the inventor [130], several modified processes have been suggested to make the Kroll process better. Including the original Kroll process ($Mg+TiCl_4$), the combination of alkaline earth metal and halogenated titanium compounds could be very efficient method to extract titanium metal, especially for purity and economical

efficiency aspects.

In the Kroll process a porous pure metal structure with micrometer-sized particles and branches can be obtained. Considering that titanium sponge materials with microscale particles has been widely applied in various engineering applications, synthesizing Ti porous structure is very important process in modern metallurgy, and calcio or magnesio-thermic reduction method using titanium halides could be one of the easiest way to synthesize the porous structure.

The Kroll process uses volatile liquid of $TiCl_4$ that is obtained from mineral ores via chlorination. By magnesiothermic reduction, $TiCl_4$ can be reduced.

$$\mathrm{TiCl_4}(v) + 2\mathrm{Mg}\ (l) \rightarrow \mathrm{Ti}\ (s) + 2\ \mathrm{MgCl_2}\ (s) \qquad \text{(4-g)}$$

The reduced pure Ti metal is subsequently separated from remained $MgCl_2$ by vaporization or leaching or acid treatment. During reduction process the space occupied by $MgCl_2$ becomes porosity after its removal. The Kroll process is to extract pure titanium as a porous Ti sponge. Similar method has been developed by Kapoor using $ZrCl_4$ instead of $TiCl_4$ to form porous zirconium [131].

In this study, magnesiothermic reduction process was used to form porous capacitor anode. Not only titanium tetraiodide but also zirconium tetrachloride was used to reduce pure Ti-Zr alloy material. In order to form the porous anode with high specific surface area, particle size was controlled by reduction temperature and time. After finishing CVD process, pyro-vacuum distillation was carried out in order to get rid of byproducts and remained molten magnesium. The morphology and particle of the porous structure were observed by scanning electron microscopy (SEM), and chemical composition was analyzed by energy dispersive X-ray spectroscopy (EDS) and X-ray diffraction (XRD).

4.2 Experimental Process Design

4.2.1 Magnesiothermic Reduction of TiI_4 and $ZrCl_4$

Magnesium was used as the reducing agent. Titanium tetraiodide (TiI_4) and zirconium tetrachloride ($ZrCl_4$) were used as pre-starting materials. Both are solid at ambient temperature and pressure, although somewhat volatile and corrosive in the air, they were relatively easy to control and were placed together into a reaction chamber. The magnesiothermic reduction in this research is described by reaction 4-h,

$$\begin{matrix} 0.5\ \mathrm{TiI_4}(v) \\ 0.5\ \mathrm{ZrCl_4}(v) \end{matrix} + 2\ \mathrm{Mg}\ (l) \rightarrow \begin{matrix} 0.5\ \mathrm{Ti}\ (s) \\ 0.5\ \mathrm{Zr}\ (s) \end{matrix} + \begin{matrix} \mathrm{MgI_2}\ (l) \\ \mathrm{MgCl_2}\ (l) \end{matrix} \qquad (4\text{-h})$$

where *v*, *l*, and *s* mean vapor, liquid, and solid phases. The halides salts, TiI_4 and $ZrCl_4$, were used to form Ti-Zr alloy sponge. The temperature and the thermochemical data of the substances in the reactions are shown in table 4-1 [132]. The Gibbs free energies of the reduction reactions are negative when molten magnesium is used. The reduction temperature in this study was chosen to form a range of morphological dimension in the final sponge products. Selected temperature conditions in table 4-1 are lower than those of industrially-used Ti or Zr extraction process to decrease growth rate of reduced Ti-Zr alloy particles and to form coarse-porous final product.

Table 4-1. Thermochemical data of substances used in the magnesiothermic reduction of TiI_4 and $ZrCl_4$ [132]

		temperature (K)	$\Delta G^{\circ}_{reaction}$ (kJ/mol)	$\Delta H^{\circ}_{reaction}$ (kJ/mol)
magnesiothermic reduction	TiI_4	1000	-266.636	-392.306
		1100	-254.361	-386.221
		1200	-242.766	-376.034
	$ZrCl_4$	1000	-209.819	-327.310
		1100	-198.280	-322.971
		1200	-187.361	-314.818

4.2.2 Vapor Pressure of Titanium and Zirconium Halides

According to equation 4-h, both halides are transformed to gas phase during the heating process. Several studies exist on the vapor pressure of liquid titanium tetraiodide and zirconium tetrachloride [133] [134]. According to these studies, the vapor pressures of the liquid halides are represented by equation 4-i and 4-j.

Titanium tetraiodide [133]:

$$\log \mathrm{P(mmHg)} = -\left(\frac{3054}{\mathrm{T}}\right) + 7.5773 \tag{4-i}$$

Zirconium tetrachloride [134]:

$$\log \mathrm{P(mmHg)} = -\left(\frac{26000}{4.57\mathrm{T}}\right) + 12.30 \tag{4-j}$$

The curves of vapor pressure of each salt are plotted in figure 4-1. For plotting process, Wolfram Mathematica 8.01 was used. The boiling and melting points of both salts are indicated in figure 4-1. Also, the crossover point of the vapor-pressure curves is marked in the graphs. Numerical information is shown in table 4-2.

Table 4-2. Vapor pressure of TiI_4 and $ZrCl_4$ as a function of temperature

	TiI_4	$ZrCl_4$
Melting Point	423K(150˚C)	710K(437˚C) (19,000 torr, vapor pressure)
Boiling Point	650K(377˚C)	604K(331˚C) (760 torr, vapor pressure)
Crossover Point	557.99K(284.99˚C) @127.05 torr* for each salts	

*calculated from eq. 4-i, and eq. 4-j.

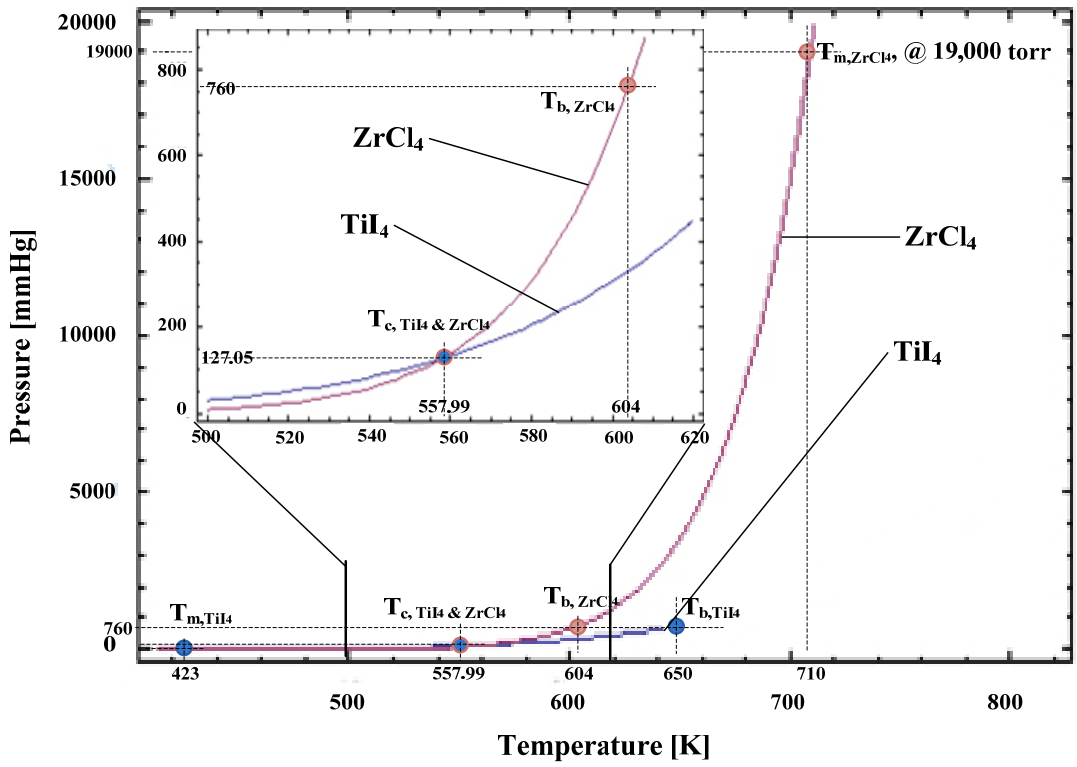

Figure 4-1. Vapor pressure curves of TiI_4 and $ZrCl_4$ as a function of temperature

As shown in figure 4-1 and table 4-2, the vapor pressure curves of TiI_4 and $ZrCl_4$ crossed at 557.99 K(284.99 ˚C) and 127.05 torr. This temperature (558 K) was chosen as a vaporization temperature for the halides to obtain an initially equal vapor pressure for each substance in the reaction chamber.

4.2.3 Process Description for Ti-Zr Alloy Synthesis from TiI_4 and $ZrCl_4$ Starting Materials

Schematic diagrams of the process are shown in the figure 4-2. During the initial stage of the process, all reactants, TiI_4, $ZrCl_4$ and Mg, are at room temperature in an evacuated chamber (figure 4-2 (a)). They have low vapor pressures (less than 20 mtorr). The following procedure was developed:

i. The temperature was increased to the crossover point, 558K (285 ˚C) to vaporize each halide. Each could form a partial vapor pressure as high as 127.05 torr. After 3 hours of temperature hold at 558 K the halides were fully vaporized and in the gas phase.

ii. Argon gas was now filled into the chamber until the total gas pressure in the chamber increased to 760 torr (1 atm) (figure 4-2 (b)).

iii. The temperature in a small reaction zone holding the magnesium substrate was increased to 923 K (650˚C) to melt the magnesium (figure 4-2 (c)). The remainder of the retort chamber remained at the lower temperature. The total gas pressure increased to slightly more than 1 atm. The reduction reaction now proceeded between the molten Mg substrate and the TiI_4 and $ZrCl_4$ vapors (equation 4-h).

iv. Metallic titanium and zirconium or Ti-Zr alloy particles nucleated most likely at the surface of the molten magnesium and being wetted by the liquid magnesium may drop below the surface of the Mg (figure 4-2 (d)). Concurrently, MgI_2 and $MgCl_2$ were formed as by-products. An excess amount of magnesium, approximately twice the stoichiometric amount of Mg needed for the reduction reaction, was used for the process. The excess molten Mg can act as a liquid bath that can provide surface sites where the reduction reaction takes place and can also serve as a reservoir to hold the reduced Ti-Zr particles/clusters in a temporary suspension.

v. The assumption is made that reduction, nucleation and growth of Ti-Zr particles occur at the surface of the molten Mg and gradually consumes the magnesium starting at the top surface. The reaction continues until all TiI_4 and $ZrCl_4$ vapor is consumed (reduced). During the reaction, Ti-Zr alloy particles are formed with an average 50%/50% composition but the localized

compositions may vary depending on location. It is likely that during aggregation and diffusion-bonding of the local concentration variations could homogenize by inter-diffusion since the diffusion distances are small (ranging from about twenty nm to less than 1 micrometer). The aggregated alloy particles are shown in figure 4-2 (e)(f). After completion of the reaction argon is evacuated from the chamber to about 10^{-3} torr vacuum. This enables vacuum distillation at 923 K from the specimen, i.e., removal of MgI_2 and $MgCl_2$ from the Ti-Zr alloy particle cluster (figure 4-2 (g)) and their deposition on a cooler part of the retort. After 9 hours of distillation, the entire chamber is cooled to room temperature and opened. Disc-shaped specimens of Ti-Zr sponge were obtained and are shown in figure 4-2 (h).

Since the objective of this research was to obtain the open porous structure of Ti-Zr alloy with fine particle or branch-size, relatively low temperatures and times were chosen for the reduction process to restrain the growth and sinter-densification of the alloy particles. Experimental conditions of low reduction temperature with short reaction times were chosen. This is different from commercial Kroll processing, which is ordinarily operated at high temperature for a long time to result in complete reaction in a relatively large volume, and which generally results in a rather coarse-porous final product [135] [136].

According to Murray [137], titanium and zirconium form a continuous range of solid solutions of BCC β-phase at elevated temperature and of α-phase at low

temperature. For Ti-50%Zr the α/β transformation occurs at 808K (535˚C). Luz et al. reported the formation of a solid solution in titanium + zirconium particles during sintering in the β region. At the lower temperatures (in the α-phase field) the rate of inter-diffusion was slow and so-formed alloy was partially inhomogeneous [138]. In the present work the homogenization would taken place in the β-phase filed, well above the transus temperature. In the present work we could experimentally verify that homogeneous Ti-Zr alloy was obtained in the synthesized fine-particle, fine-porous sponge samples even at the lowest processing (reduction) temperature of 923 K.

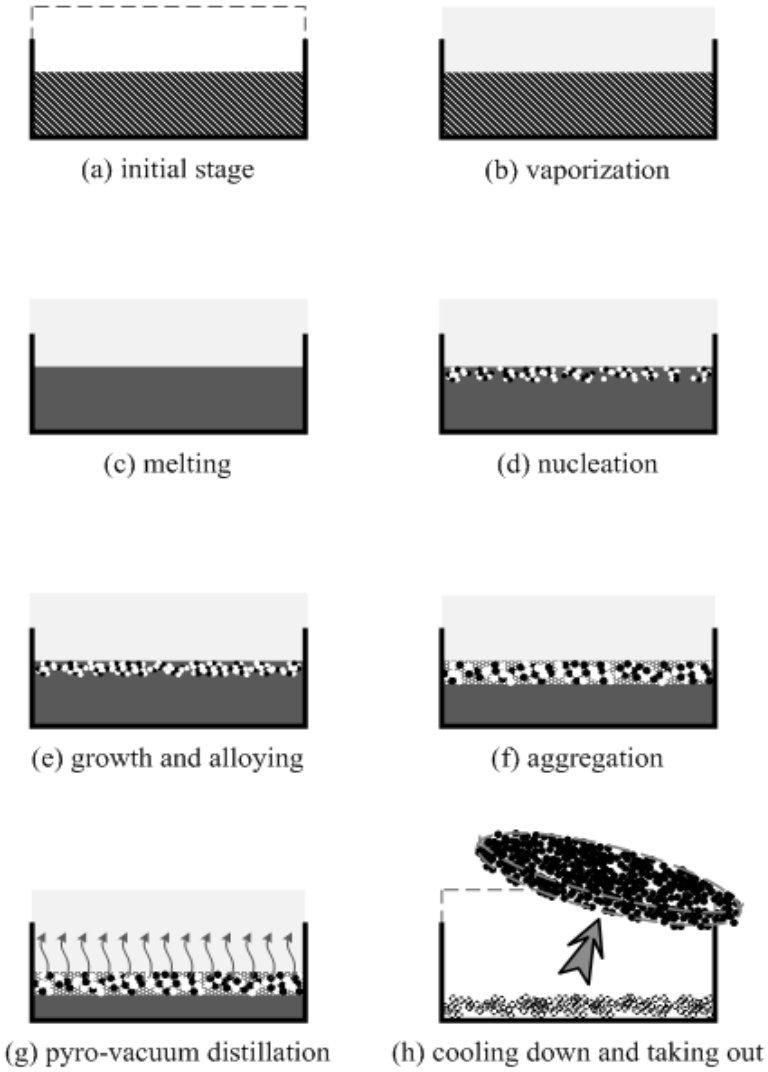

Figure 4-2. Processing stages during magnesiothermic reduction of TiI_4 and $ZrCl_4$

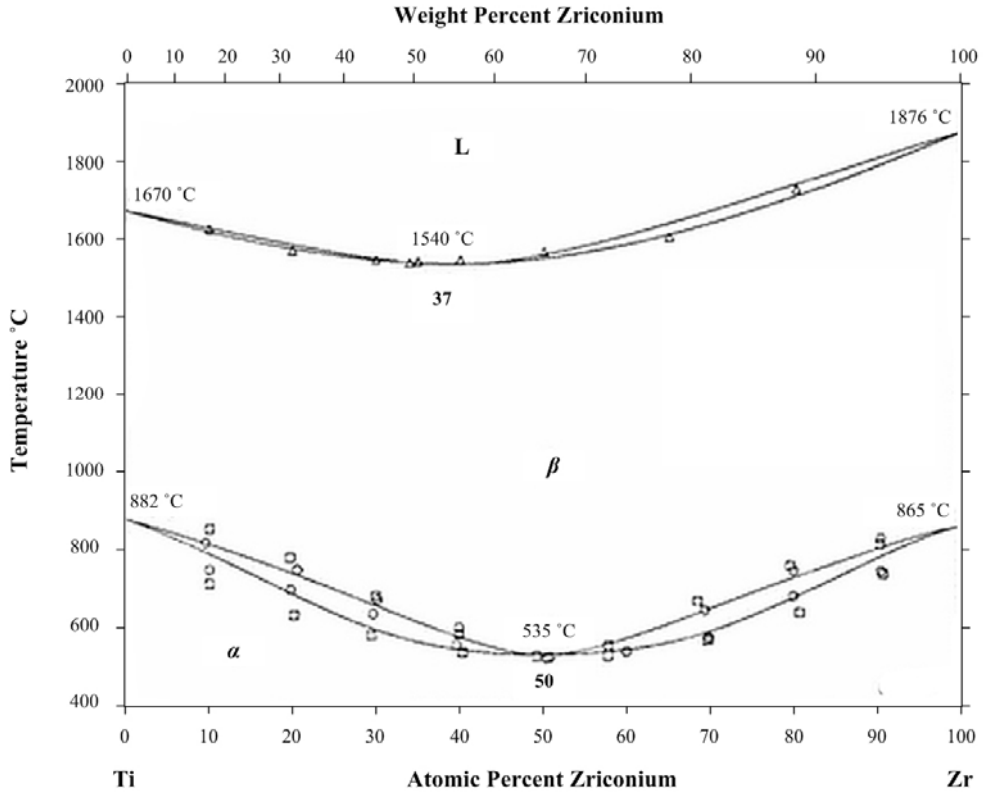

Figure 4-3. Phase diagram of Ti-Zr phase binary alloy [137]. The reduction and aggregation processing of Ti-Zr particles were done between 923 K (650˚C) and 1073 K (800 ˚C)

4.3 Experiments

4.3.1 Sample Preparation

Figure 4-4 shows a process of sample preparation. Mg pellets (99.95%, from Kurt J. Lesker Co.) were filled in a pressing die, and a magnesium disc was molded by die pressing. The Mg disc was mechanically polished with 4000 grit SiC paper to smoothen its surface. A disc-shaped titanium wire mesh (of CP grade 2 Ti-wire, Φ0.299 mm, 24×24 wires/inch, from Unique Wire Weaving Co.) of the same diameter as the molded Mg disc was prepared and pressed into the magnesium disc. The Ti mesh was used as a frame that later supported the reduced alloy sponge. Final dimension of Mg disc with Ti mesh frame is Φ19.05mm×1mm thickness. The weight including mesh frame is about 2.2g on average. Commercially available TiI_4 (99.9%, Alfa Aesar) and $ZrCl_4$ (99.5+%, Alfa Aesar) were used as reactants. 1.25g of TiI_4 (0.00225 mol) and 0.524g of $ZrCl_4$ (0.00225 mol) were weighed in the Ar chamber and put in the tray with Mg disc.

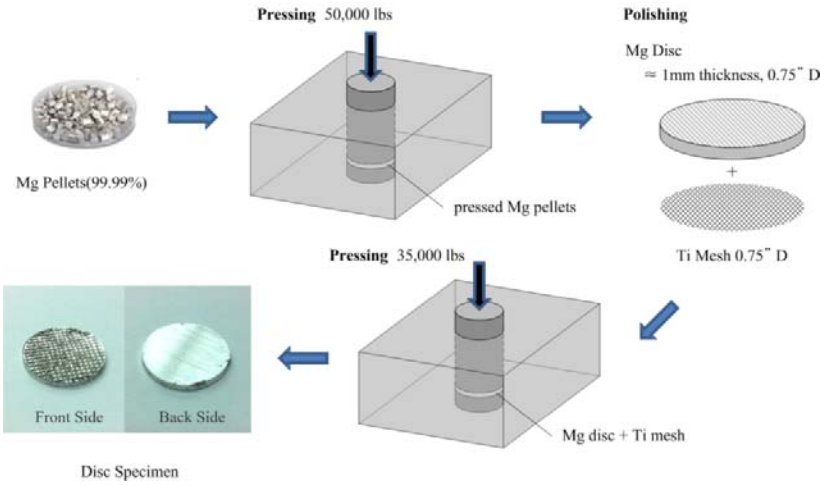

Figure 4-4. Sample preparation of Mg disc with Ti mesh frame

4.3.2 Experimental Apparatus

A schematic diagram of the experimental apparatus for the chemical vapor deposition process is shown in Figure 4-4. Since stainless steel could be attacked by the corrosive halide salts, the body of the vacuum chamber is made up of a double-walled cylinder tube; stainless steel on the outside and titanium for inside. Also, the system has a titanium blocking disc that is controlled by external mechanical feed-through. It can be moved to block or open the entrance of the inside Ti tube. The entrance is opened during pyro-vacuum distillation process.

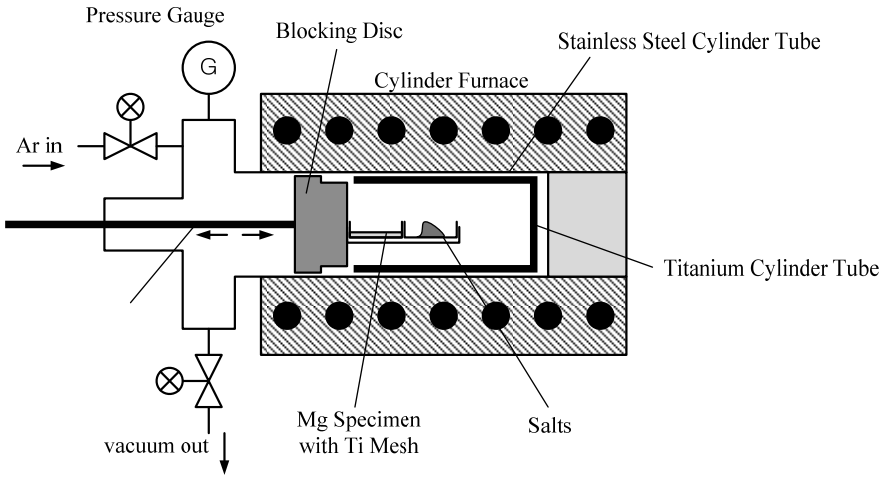

Figure 4-5. Diagram of the experimental apparatus for magnesiothermic reduction of TiI_4 and $ZrCl_4$

4.3.3 Experimental Procedure

Table 4-3 shows experimental procedure and condition. Before starting heating, Mg disc and the Ti- and Zr- halide salts were put on the tray and placed into the heat zone of the chamber. Initially, it was evacuated to 0.02 torr. Then, the inside titanium cylinder tube where the specimens were placed was closed by the blocking mechanism. Simultaneously, temperature of the surrounding cylindrical furnace was heated up to 558K (285˚C). It was held for 3 hours to vaporize the halide salts.

When the halide salts were completely evaporated after 3 hours of temperature holding, the temperature of the cylinder portion with the Mg specimen was heated to the higher reduction temperature. Three temperature conditions were used for reduction: 923K (650˚C), 973K (700˚C) and 1073K (800˚C). To prevent Mg vaporization, the overall chamber pressure was adjusted to760 torr (1 atm) by Ar gas filling.

After 9 hours of reduction, the blocking disc was opened for the vacuum distillation to take place by keeping the temperature constant in the reactor portion and opening an exit to a cooler evacuated chamber portion. The vacuum distillation removes remaining metallic magnesium and the by-products, MgI_2 and $MgCl_2$ from the Ti-Zr sponge samples. The distilled magnesium and by-products were condensed on the internal surface of the chamber's cool zone. Empirically, 9 hours of vacuum distillation was enough to get rid of the unwanted by-products. After finishing the distillation, the chamber was cooled down to room temperature. The samples could then be safely removed.

To investigate the effect of reduction time on the alloy particle size, the 24 hour reduction at 1073K was also carried out. The result was compared with the 9 hour reduction at 1073K.

Table 4-3. Experimental process conditions during Ti-Zr sponge synthesis

Stage	Temperature [K]	Initial Pressure [Torr]	Time [hours]
Initial Vacuuming	298 (25˚C)	0.02	0.5
Vaporization of Halides	558 (285˚C)	0.02	3
Magnesiothermic Reduction	923 (650˚C) /973 (700˚C) /1073 (800˚C)	760	9/24
Vacuum Distillation		0.02	9
Cooling Down	298 (25˚C)	0.02	12

4.3.4 Analyses of Synthesized Alloy Specimens

Scanning electron microscopy (SEM; Helios Nanolab 650) was used to study surface morphology of the sponge specimens. The branch size distribution was performed using analyzing software (Particle Analyzer, ImageJ). Also energy dispersive x-ray spectroscopy (EDS) was carried out. Information on lattice-plane spacings of the spongy alloys was obtained by powder x-ray diffraction (XRD; Discover D8 instrument by Bruker) operating at 35kV and 25mA with Co $K\alpha_1$ source (characteristic $K\alpha_1$ wavelength of 1.789Å). The scan results were recorded over a (2θ)-diffraction-angle range from 30˚ to 90˚ with a 0.05˚/sec scan rate. The measured diffraction patterns were calculated to obtain d-spacing values for Co $K\alpha_1$ relative to

referenced Cu $K\alpha_1$-based data in JCPDS database. The software (PCPDFWIN) was used. Two peaks of interest, (100) and (002), were selected from the patterns to determine the lattice parameters, a and c, of the synthesized Ti-Zr sponge and Ti-Zr bulk alloy specimens. Equation 4-1 was used to calculate the a- and c- lattice parameters, i.e., the interplanar spacing of {100} and (001) planes (Miller notation) or $\{2\bar{1}\bar{1}0\}$ and (0001) planes (Miller-Bravais notation) in the hexagonal structures of the present alloys. These parameters were then compared to the literature values of a and c for Ti-Zr alloys shown in figure 4-16.

$$\frac{1}{d_{(hkl)}{}^2} = \frac{4}{3} \cdot \left(\frac{4h^2 + hk + k^2}{a^2} \right) + \frac{l^2}{c^2} \qquad (4\text{-}1)$$

4.4 Results and Discussion

4.4.1 SEM Study of Surface Morphology of Ti-Zr Alloy Sponge

4.4.1.1 The Overall Shape of the Sponge

A Ti-Zr alloy sponge specimen, synthesized at 923K, is shown in figure 4-6. It was made by magnesiothermic reduction of Ti and Zr halide salts on a pressed magnesium disc with Ti-wire-mesh. After pyro-vacuum distillation process a fine porous alloy sponge was obtained attached to a Ti-mesh frame. Under (white) daylight the color of the reduced sponge is dark gray or black. This is because the incident light is mostly absorbed in the sub-micrometer porosity of the alloy sponge.

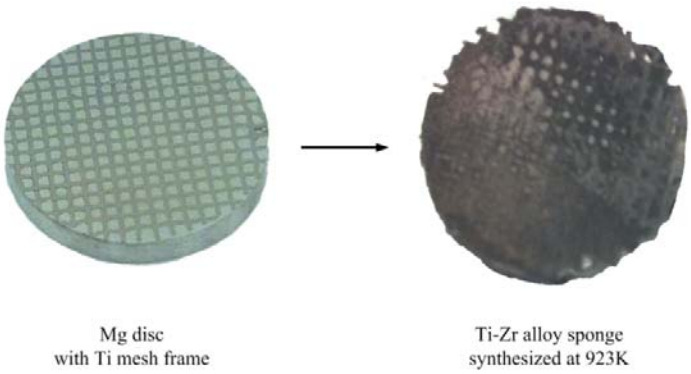

Figure 4-6. Photographs of the Mg disc specimen with impressed Ti-mesh frame before (left) and after (right) synthesis of Ti-Zr alloy sponge.

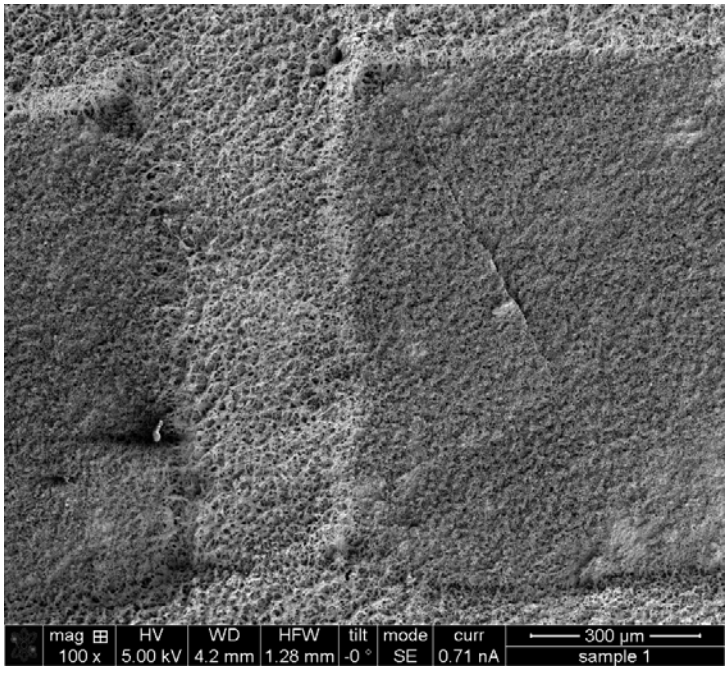

Figure 4-7. SEM micrograph of Ti-Zr sponge synthesized at 973K on a Mg disc that was impressed with a titanium mesh; Magnification ≈100×

Figure 4-7 is a SEM micrograph of synthesized Ti-Zr alloy sponge at a moderate magnification (100×). The Ti-Zr alloy sponge has filled the rectangular (797μm × 797 μm) spaces of the titanium wire mesh and has also grown on top of the framework of the wire mesh. A cross-section of the Ti-Zr alloy sponge was prepared by focused ion beam (FIB) milling; figure 4-8 shows the image of the three-dimensional structure. Thin alloy branches with porosity reach into the interior of the sponge. Particles of various shapes and sizes appear to have accumulated (irregularly) and have formed an interconnected sponge cake through sinter-bonding at the contact points. The pores are also interconnected and form a continuous pore volume that is open to the outer surface. Some tiny pores appear to have remained as closed voids.

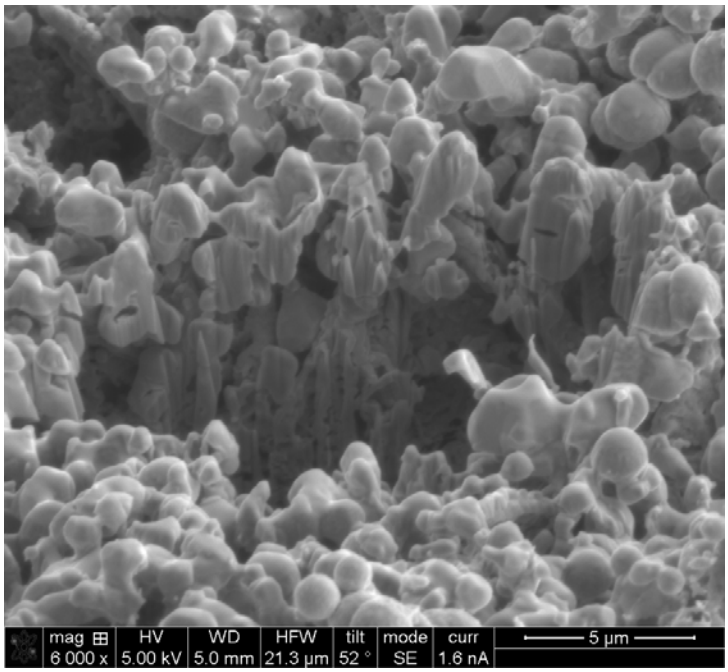

Figure 4-8. View of cross-section through Ti-Zr alloy sponge synthesized at 973K. The cross-section was prepared by FIB milling.

4.4.1.2 The Role of Reduction Temperature on the Alloy Microstructure, in Particular on Branch and Pore Sizes

Figure 4-9, 10 and 11 show SEM micrographs of Ti-Zr alloy sponges synthesized at different temperatures; 923K (650˚C), 973K (700˚C) and 1073K (800˚C). Irrespective of the reduction temperature, most particles have globular or near-spherical shapes. They have bonded together and form clusters. Pores can be regarded as empty space that was formerly occupied by the reaction by-products, MgI_2 or $MgCl_2$, and then removed by distillation. Assuming no volume shrinkage of the sponge structure during vacuum distillation the pore volume would theoretically be the same as the volume of the by-products. With this assumption the volume ratio of Ti-Zr sponge to empty space can be calculated from above equation 4-h to be about 1 : 8.43 for the reduction with magnesium. The observed porosity in figure 4-8 was much less. Although it was not quantitatively measured the ratio appears to be closer to 1:1. One can conclude that the pore volume shrank during the sinter-process that accompanied the vacuum distillation.

Surface morphology and porosity are related to the size (or branch diameter) of alloy particles, which is affected by the processing temperature. Figure 4-9 shows SEM results of Ti-Zr sponge synthesized at 923K. For the magnesiothermic reduction to take place at a relatively rapid rate liquid magnesium is required. 923K is the temperature at which pure Mg can be melted. The so-formed Ti-Zr sponge exhibits a uniform distribution of fine alloy particles. When the processing temperature is increased to 1073 K, the particle size increases (figure 4-9, 10 and 11).

The particle size distribution can also be affected by temperature. While most of the particles in the alloy sponge formed at 923 K are of relatively uniform size and are connected to one another with narrow necks (figure 4-9, 10), the alloy sponge synthesized at 1073 K shows larger and more irregular particle sizes (figure 4-11). Also the packing of the alloy particles is in some areas densely packed and in other areas loosely packed, presumably stemming from non-uniform agglomeration. Table 4-4 and figure 4-12 show the particle size distribution. The particle size distribution of 1073 K synthesized material is wider than the ones synthesized at 923K and 973K. Similar relations between processing temperature and size distribution have been reported in the literature [139] [140]. The irregular particle growth at the higher temperature can be explained in part of grain coarsening when solid/liquid interfaces enable mass transport, such as during 'Ostwald ripening' in which coarser particles grow at the expense of smaller particles [141]. In the present experiments the particles are coarsened in the excess liquid Mg matrix phase. Sahu et al., pronounced on the findings of their research that Ostwald ripening is the dominant mechanism by which particles coarsen more at relatively high temperature and cause the size distribution to be wider [142].

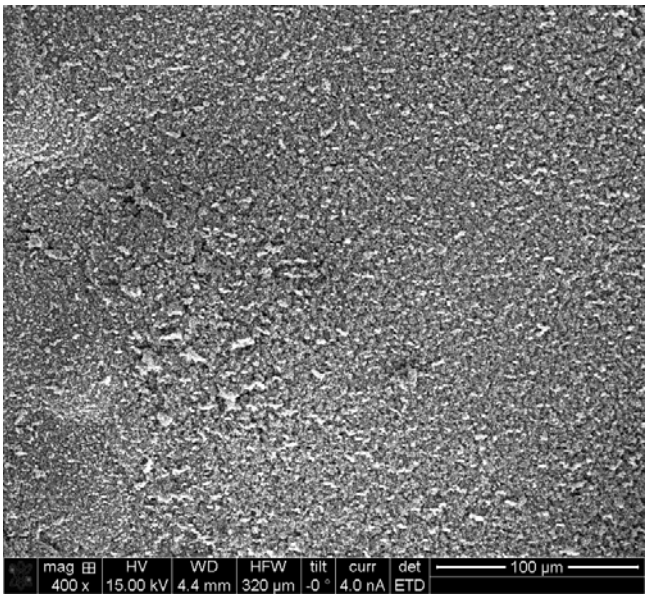

(a)

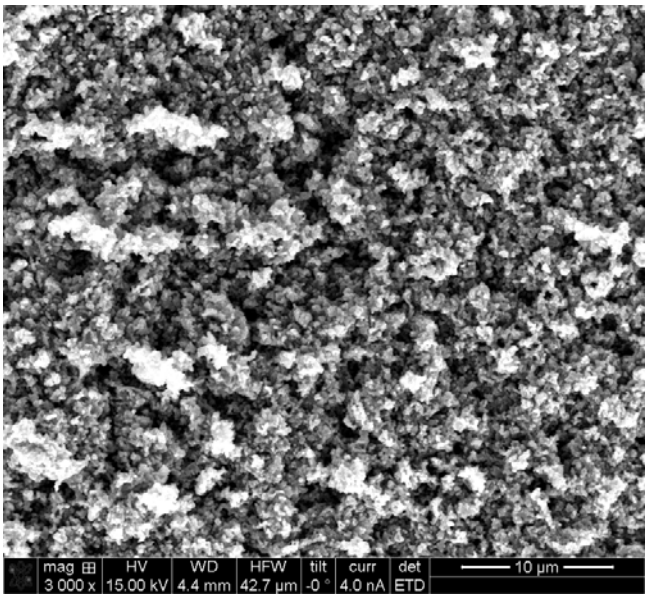

(b)

Figure 4-9. SEM micrographs of Ti-Zr sponge synthesized at 923K;
(a) 400× magnification, (b) 3,000× magnification

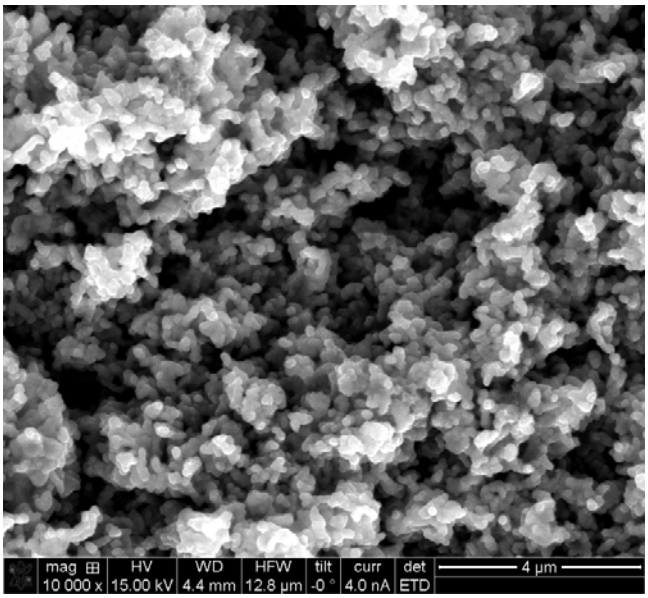

(c)

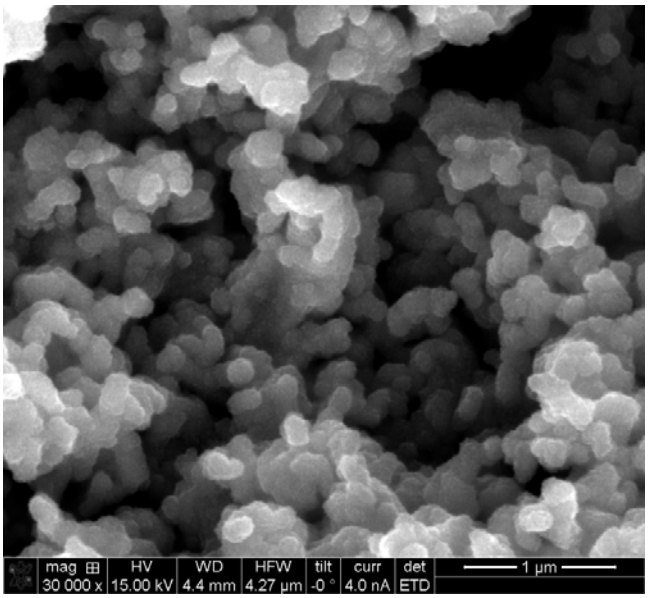

(d)

Figure 4-9. (continued) SEM micrographs of Ti-Zr sponge synthesized at 923K; (c) 10,000× magnification, (d) 30,000× magnification

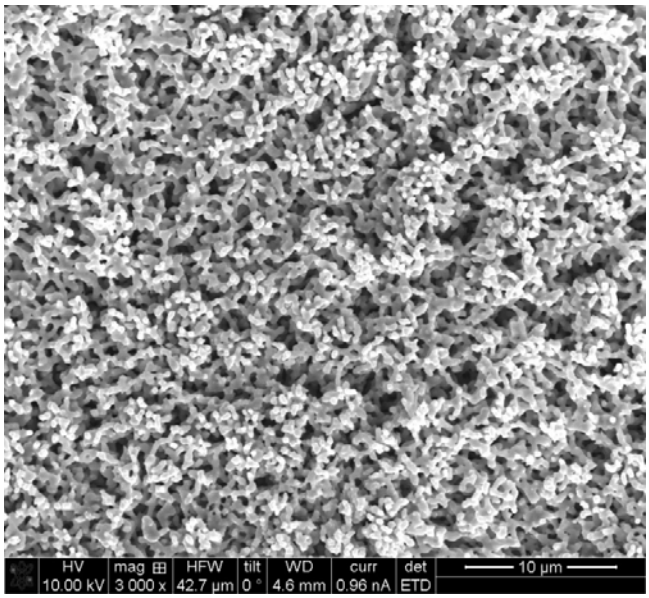

(a)

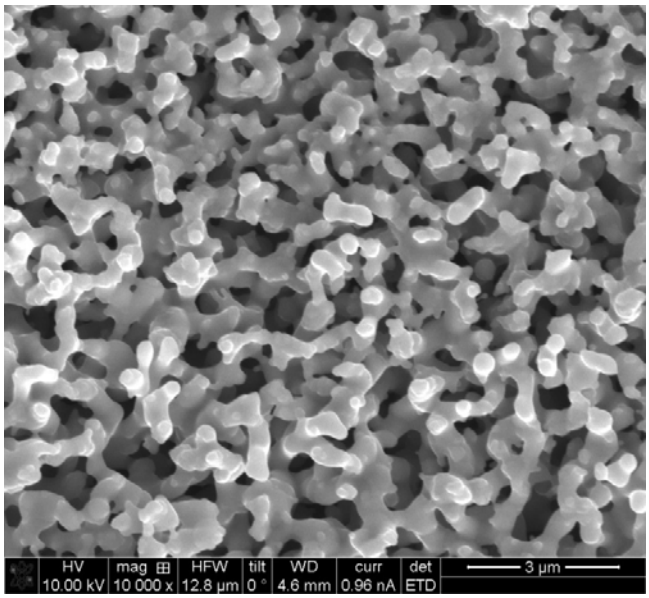

(b)

Figure 4-10. SEM micrographs of Ti-Zr sponge synthesized at 973K;
(a) 3,000× magnification, (b) 10,000× magnification

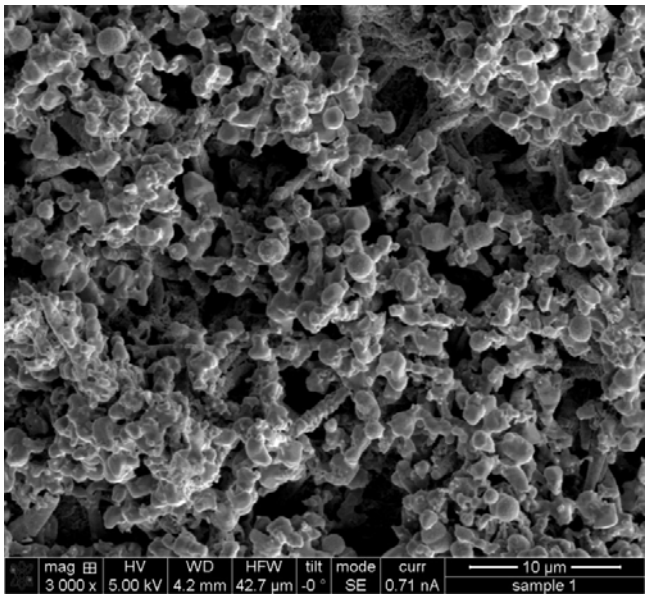

(a)

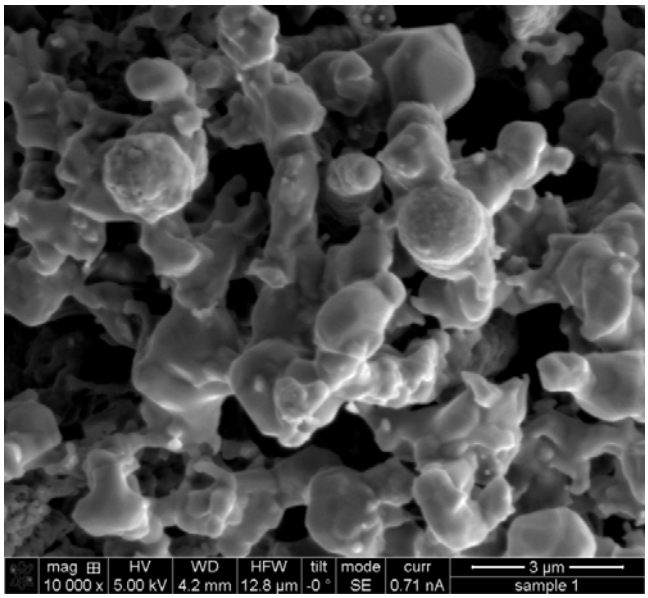

(b)

Figure 4-11. SEM micrographs of Ti-Zr sponge synthesized at 1073K;
(a) 3,000× magnification, (b) 10,000× magnification

Table 4-4. Branch and pore size distribution of Ti-Zr alloy sponges formed at various reduction temperatures

	Processing temperature (K)	Size distribution of sponge branches (μm)		
		Size range	Average size	Standard deviation
magnesiothermic reduction	923	0.059 ~ 0.165	0.103	0.029
	973	0.068 ~ 0.318	0.213	0.042
	1073	0.507 ~ 2.097	1.285	0.364

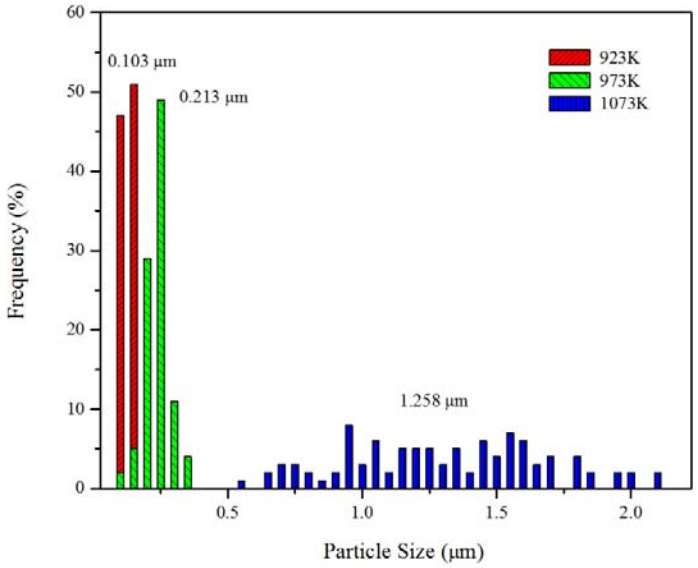

Figure 4-12. Feature size distribution of reduced Ti-Zr alloy sponge

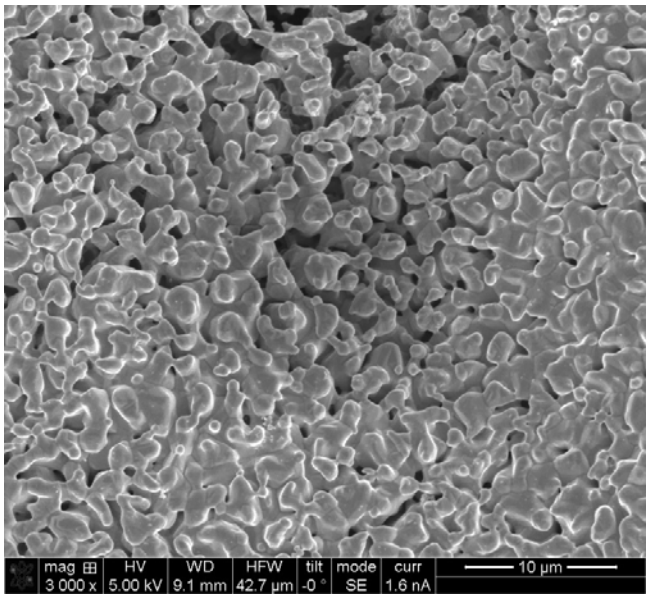

(a)

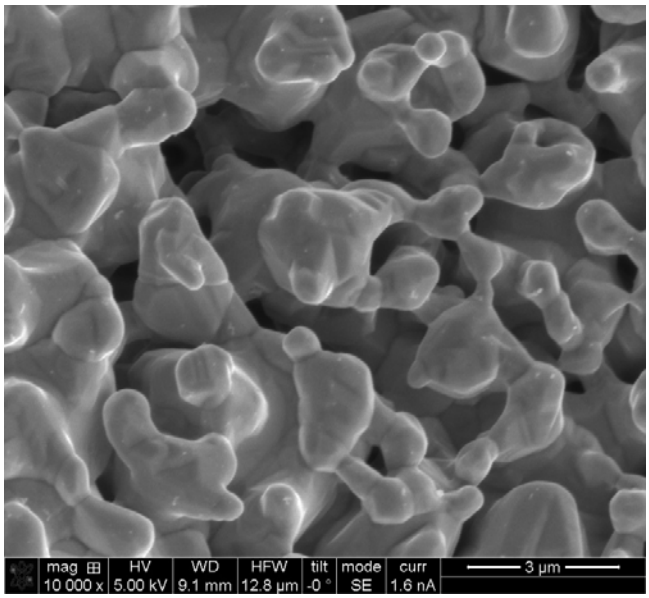

(b)

Figure 4-13. SEM micrographs of Ti-Zr sponge synthesized at 1073K for 24 hours of reduction (a) 3,000× magnification, (b) 10,000× magnification

4.4.1.3 The Role of Reduction Time on the Alloy Microstructure, in Particular on Branch and Pore Sizes

Figure 4-13 shows SEM micrograph of Ti-Zr sponge material synthesized by reduction at 1073K for about 24 hours. The surface morphology is different from the image of the sponge formed during 9 hours of reduction-processing. The alloy particles may have more time to grow, connect and bond to one another during the longer reduction process and form a more-conglomerated structure. Compared with the particles of the 9-hours processed specimen (figure 4-11), the particles in the 24-hours processed specimen (figure 4-13) are more agglomerated, and the amount of pores in the sponge structure has decreased. Sintering process model for the porosity p applied using equation 4-2 [120]. It shows a logarithmic dependence of porosity p on time t at constant temperature.

$$p - p_0 = \ln \frac{t}{t_0} \tag{4-2}$$

where p_0 and t_0 mean porosity and time at the beginning of isothermal sintering. From the initial value of p_0, the porosity decreases logarithmically with sintering time. With increasing time the particles become more agglomerated to form a well interconnected sponge, and the porosity is decreased.

4.4.2 Chemical Analyses of Synthesized Porous Ti-Zr Alloys

Figure 4-14 shows the spectra of energy dispersive x-ray spectroscopy (EDS) of Ti-Zr specimens synthesized at 923 K and 1073 K. In the spectra, intensity peaks are observed that are characteristic of each alloy element, Ti and Zr. A small Al-K peak is caused by the aluminum specimen holder and can be ignored.

XRD analyses were also performed on the synthesized sponges. The XRD diffraction patterns for Ti-Zr alloy sponge synthesized at 923 K and 1073 K are shown in figure 4-15. It also includes a reference diffraction pattern for the Ti-50at.% Zr bulk specimen that was used for electrochemical tests. Additionally, published (standard) diffraction patterns for pure Ti and pure Zr are included for comparison. According to Ti-Zr equilibrium diagram [137], both titanium and zirconium are completely miscible in all phases. The Ti-Zr alloys sponge specimens synthesized at 923K and 1073K show sharp peaks from crystalline α-(Ti-Zr) phase (hcp). Ti-Zr sponge synthesized at 1073 K correspond to the pattern of the Ti-50at% Zr bulk specimen, while the peaks from the one synthesized at 973K slightly shifts to low diffraction angle compared to the pattern of the Ti-50at% Zr bulk specimen.

The measured XRD diffraction peak angles were used to calculate specific lattice-plane spacings and the lattice parameters. Table 4-5 shows the results. The experimentally determined lattice parameters of each the Ti-50at.% Zr bulk specimen and of the Ti-Zr sponge specimen synthesized at 1073K correspond approximately with literature values for Ti-Zr alloy. The lattice parameter of the 923K-synthesized Ti-Zr sponge specimen is slightly larger than the literature value for a stoichiometric

50/50 alloy. It means the sponge has a slightly higher Zr-concentration. Comparison with published lattice parameters in figure 4-16 indicated best match with a Zr-concentration of 55 at.% [143] [144]. The deviation from 50/50 may be associated with variations of the actual vapor pressures of TiI_4 and $ZrCl_4$ during the synthesis process.

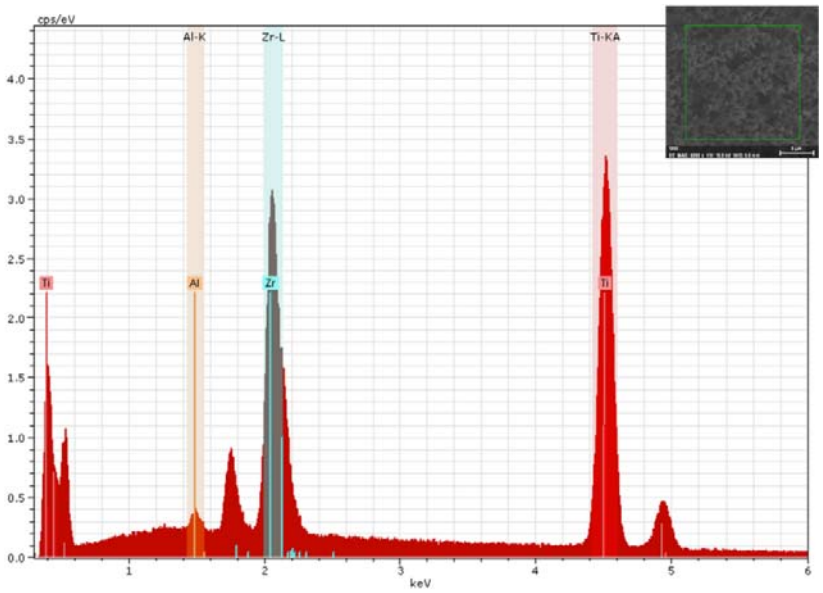

(a)

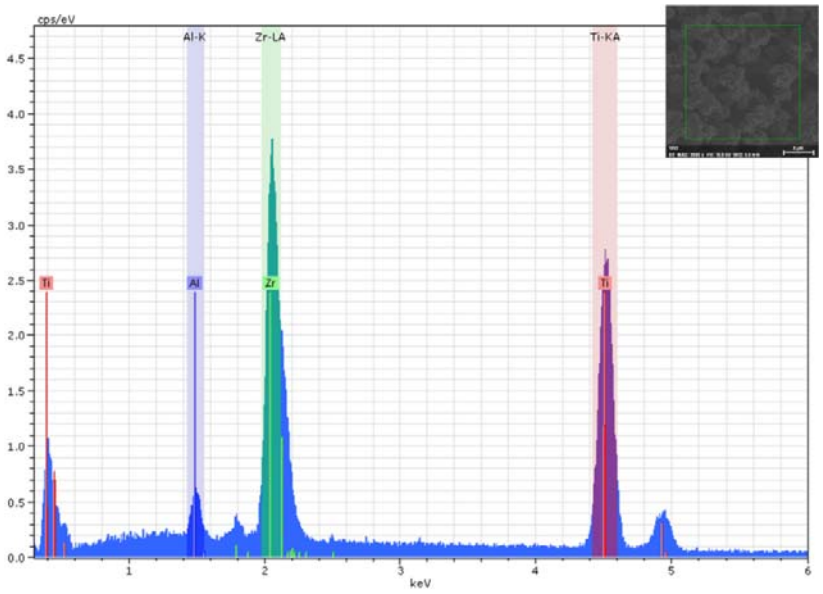

(b)

Figure 4-14. Spectra of EDS of Ti-Zr sponge synthesized at (a) 923K, (b) 1073K, 9 hours reduction

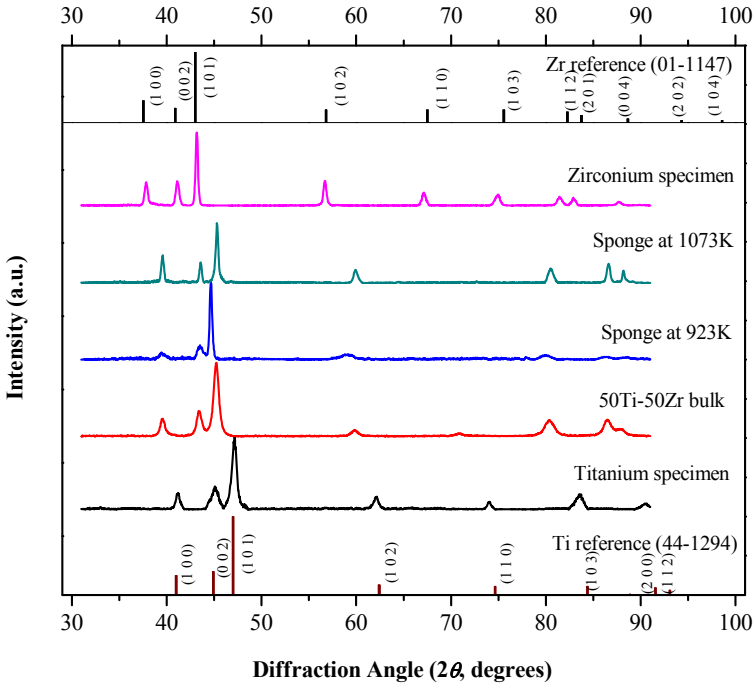

Figure 4-15. XRD diffraction patterns measured with Co $K\alpha_1$ incident beam (λ=1.789Å) of pure Ti and Zr specimens, Ti-Zr binary alloy bulk specimen, and Ti-Zr sponge synthesized at 923K, and 1073K.

Table 4-5. Lattice parameters of Ti-Zr alloys determined from XRD results.

Comparison with published lattice parameters of binary Ti-Zr alloys, shown in figure 4-16, enables an estimate of the composition of the synthesized alloy sponges.

Ti-50at.% Zr	Ti-Zr bulk specimen	Ti-Zr alloy sponge synthesized at		Literature value
		923K	1073K	[143] [144]
a [nm]	0.3094	0.3103	0.3096	0.3091
c [nm]	0.4933	0.494	0.492	0.493

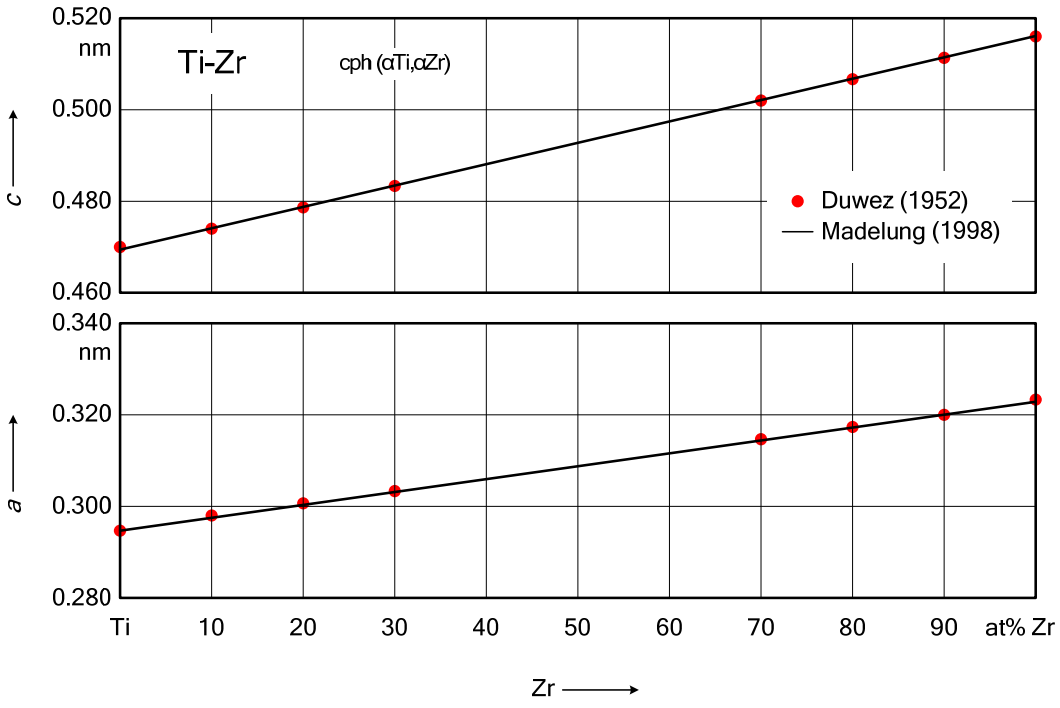

Figure 4-16. Ti-Zr Lattice parameter for cph (αTi, αZr) solid solution alloys by Duwez (1952) [143], and Madelung (1998) [144]

According to Brunsch and Steeb [145], diffusion coefficient values for the diffusion of titanium in β-zirconium and zirconium in β-titanium in Ti-49.5at.% Zr binary alloy at 1073 K (800 ˚C) are as follows.

$$\widetilde{D}_{\mathrm{Ti}} = 3.2 \times 10^{-10}\mathrm{cm}^2/\mathrm{sec}$$
$$\widetilde{D}_{\mathrm{Zr}} = 5.1 \times 10^{-10}\mathrm{cm}^2/\mathrm{sec} \quad [145]$$

From formula of diffusion distance over time, $x = \sqrt{t\widetilde{D}}$, a distance that Ti or Zr atoms diffuse into existing Ti-Zr alloy can be calculated. For 1073 K-synthesized Ti-Zr sponge specimen in this study the total thermal process time was 18 hours (9 hours of magnesiothermic reduction + 9 hours of vacuum distillation). The calculated distance of Ti diffusion in β-zirconium is about 4 μm, and the distance of Zr diffusion in β-titanium is about 5 μm. In comparison with data in table 4-4, the diffusion distances are almost twice longer than average particle size of 1073 K-synthesized Ti-Zr sponge specimen. Ti and Zr atoms have enough high diffusivity to form homogeneous Ti-Zr alloy when it is a solid solution.

Although the experiment was designed to yield a 50/50 ratio of Ti and Zr, the actual local partial pressures of starting halides and the individual sticking coefficients during reduction and nucleation of Ti- and Zr-metal may have caused the composition of sponge particles to vary somewhat between early and later-formed particles.

The electrochemical test results in Chapter 3 have shown relatively low leakage current for anodic Ti-Zr oxide films and exhibited higher resistance to oxygen evolution when the Zr content was between 40at.% to 60at.%. Therefore, an observed deviation of 5% in synthesized sponge specimens from the envisaged 50/50 stoichiometric composition is in the acceptable range for low-leakage capacitor anodes.

4.5 Conclusions

Porous Ti-Zr nanostructure was synthesized by magnesiothermic reduction and sinter processing under controlled temperatures and partial pressures of the reactants. Titanium tetraiodide and zirconium tetrachloride were used as starting materials, and magnesium was used as the reducing agent. The ratio of two halides was determined based on the intention to form a Ti-50at.% Zr alloy in a fine-porous sponge anode. This was based on the earlier electrochemical test results showing lowest leakage currents through anodically formed oxides on alloys ranging from Ti with 40 to 60at.% Zr. A reactor for chemical conversion processing was designed for simultaneous reduction of TiI_4 and $ZrCl_4$ vapors on a liquid magnesium substrate and for subsequent vacuum-distillation of volatile reaction products.

The experiments yield clean Ti-Zr open-porous sponge specimens. The synthesized alloy sponges were analyzed by SEM and particle size analysis. Depending on the chosen process parameters, mainly temperature and time, the average particle and sponge-branch sizes ranged from one-hundred nanometers to a few micrometers. The alloy sponge samples contained interconnected open porosity formerly occupied by by-products of the reduction reaction. From the chemical analyses by EDS and XRD it was confirmed that relatively homogeneous Ti-Zr alloy sponges were synthesized for all experimental temperature conditions.

Chapter 5 Anodization of NM-Porous Synthesized Ti-Zr Sponge and Testing of the Anodic (Ti-Zr)O_2 Films as an Electrolytic Capacitor Anode

5.1 Introduction

The anodic TiO_2 film can be considered as a dielectric of the electrolytic capacitor due to its advantages; high relative permittivity [5] [62] [63], low density, and low price [22]. However, since it has high leakage current, the anodic TiO_2 film is less attractive to be applied to the commercial capacitors [22] [23]. According to the studies hitherto discussed in the above chapter 2, the amorphous-to-nanocrystalline transition occurs during oxide growth at specific anodization condition (Table 2-2). With long time anodization, the initial amorphous TiO_2 layer changes to anatase that provides conductive pathways for electron charges. The current flow is called leakage current. To reduce the leakage of the anodic titanium oxide film, zirconium was considered as an alloy element in the present dissertation. Also, a new method to synthesize porous sponge anode was developed. In order to synthesize fine particles as possible, the reduction condition was controlled to reduce growth of the particles.

As mentioned above chapter 4, surface morphology and particle size now became an important factor to increase amount of energy stored in the energy storage [119]. However, there is a dimensional limitation to reduce particle size or to grow

oxide layer. According to Kelly et al., the oxide layer should be less than half of porous structure's dimension [146].

$$d \leq \frac{D}{2} \tag{5-1}$$

thus, it could be below,

$$D \geq 2d \tag{5-2}$$

where d is thickness of oxide layer, D is the typical dimension of the porous structure. Figure 5-1 shows a schematic diagram about it; if the oxide layer is thicker than half of the typical dimension D of the porous structure, than the total capacitance would equal to that of a flat electrode (figure 5-1-(b)). Thus in this case, there is no effect of enhanced specific surface area in total capacitance. Therefore, the size of particle of porous structure has to be designed with considering thickness of the oxide layer. If the oxide layer is designed with thickness of several tens of nanometers, then the metal porous structure should have at least twice larger dimension than oxide layer, which means it would be almost around 100nm of D value.

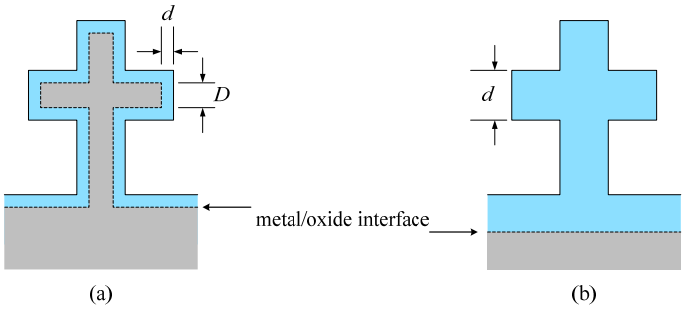

Figure 5-1. Schematic of a porous structure;
(a) the thickness of the oxide layer, *d*, is less than half the typical dimension, *D*, of the porous structure, (b) the nanostructure is completed depleted when anodic film completely consume their branches of the sponge [146]

From the result of the chapter 2, it is confirmed that the oxide thickness was about 50nm by 30V of anodization in the 1% electrolytic capacitor. The results correspond with previous research [22]. Considering the minimum anodization ratio of Ti-Zr alloy that was reported [91], the theoretical thickness of the oxide on Ti-Zr alloy could be about 52.5nm. According to Khalil [147], the ratio of the increased oxide thickness above the original metal/natural oxide interface to the total oxide thickness was 0.35, namely, 35% of oxide layer is formed by cation migration. Therefore, in the case of titanium, actual thickness of oxide growth from the original metal surface would be about 17.5 nm. Since the minimum dimension of developed particle in this research was averagely 103 nm, thus, it satisfies above equation 5-2.

Assuming that homogeneous oxide film is formed on the porous nanostructure by anodization, and thickness is smaller than half of the particle dimension, we can

calculate specific surface area from voltage climbing and the transition point during potentiostatic anodization. During stage zero, current increase rapidly up to the maximum limit, and the oxide film grows linearly [22]. If the surface area is enlarged, and the oxide layer forms homogeneously and grows linear, then total amount of coulombs for oxidation will be increased. Under constant current in the zero stage, it takes longer time to reach transition point (equation 5-3). Therefore, we can compare transition point of each specimen and can calculate the specific surface area of porous sponge specimen (figure 5-2).

$$\frac{Q_1}{t_1} = \frac{Q_2}{t_2} \tag{5-3}$$

In this chapter, the thin oxide layer was formed on the developed Ti-Zr alloy sponge specimens by anodization. 30V of constant voltage was applied to the Ti-Zr sponge specimens in the 1% phosphoric acid electrolyte. Leakage current was measured after the oxide film forming. Capacitance and DF were also measured.

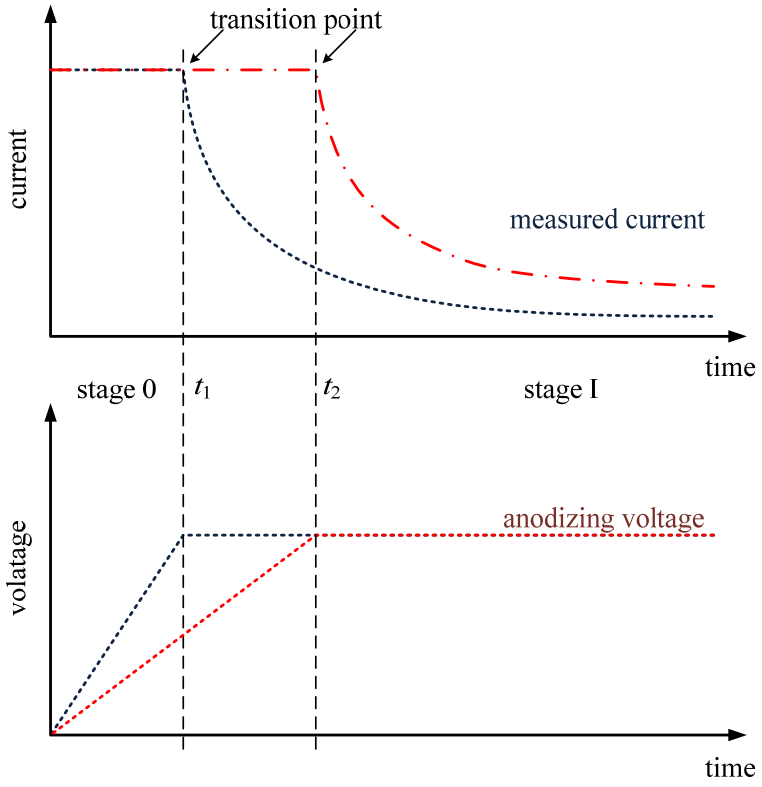

Figure 5-2. Illustration of potentiostatic anodization

5.2 Experimental Procedure

5.2.1 Ti-Zr Alloy Specimen Selection and Preparation

The porous sponge nanostructure of the Ti-50at.%Zr binary alloy that is synthesized by magnesiothermic reduction was used for the anode material of the electrolytic capacitor. Considering effect of specific surface area on the energy density of the final capacitor products, specimens with smaller particles size were preferred to be anodized. Sponge specimen that are synthesized under low

temperature was mainly considered; Ti-50at.%Zr sponges synthesized at 923K, 973K, and 1073K. To investigate the effect of Zr content on reducing the leakage current, pure titanium sponge synthesized at 1073K was also selected. Additionally, Ti mesh that was used for a frame of sponge was selected to be compared with other materials. Those results were compared to the potentiostatic polarization test data of standard specimen—pure Ti and Zr. The eight selected specimen are shown in table 5-1.

Each of selected specimens (porous nanostructure specimens and Ti mesh) was electrically connected to titanium wire (CP grade 2; Tricor Metals, 0.030″ OD) by lab-scale micro-welder (Orion 100C). The wire was then masked by a sealant (Silicone Sealant, 3M); thus the Ti wire was not revealed to the electrolyte.

Table 5-1. Anodizing and specimen information

	Composition	**Specimen**	
(a)	pure Ti	bulk	
(b)		mesh frame	
(c)		porous sponge specimen	synthesized at 1073K
(d)	50Ti-50Zr	bulk	
(e)		porous sponge specimen	synthesized at 923K
(f)			synthesized at 973K
(g)			synthesized at 1073K
(h)	pure Zr	bulk	

5.2.2 Anodization of Ti-Zr Alloys and Dielectric/Electrochemical Studies

The wire-connected specimens were anodized by the potentiostatic anodization in the 1% phosphoric acid solution (0.17M, 1.42pH). A two electrode cell system with pure Ti rods (Φ0.5cm×25cm) was used for anodization. Power supply and digital multi-meter (DMM 2000, Keithley) with connected desktop computer was used for the anodization.

The sponge specimen was immersed into the electrolyte for 4 hours before anodization to measure open circuit potential. The immersion time is twice longer than bulk specimen, because the electrolyte penetrates into small pits or gaps that may exist in the sponge specimen. Then, 30V of constant voltage with max 20mA of current was applied to the specimen. It was held for 3600 seconds. The current flow in the electrochemical cell during anodization was measured and logged to the system.

The capacitance and dissipation factor (dielectric loss tangent) were measured using LCR meter (HP 4262A) at 120 Hz and 1 kHz with 6V bias. Leakage current of the anodic oxide film on the porous nanostructure specimen was measured. The current was measured at 3V, 5V, 10V, 15V, 20V, and 30V, waiting two minute after applying voltage.

5.3 Results and Discussion

5.3.1 Potentiostatic Anodization of Ti-Zr Alloys

Figure 5-3 shows results of potentiostatic anodization. The ordinate of the graph represents the anodizing and anodic self-repair current for specimens. The shapes of the curves depend on the composition, microstructure and defects of the growing and/or self-repairing oxide dielectric. Curves of Ti mesh, (b), and Ti sponge specimen, (c), are similar to those of pure Ti bulk specimen (a); the current drops rapidly after the initial anodization stage, then gradually climbs, forming plateau. However, for the four Ti-Zr alloy specimens, including synthesized porous sponge specimens, only the expected current drop is observed. (figure 5-3-(d),(e),(f),(g)).

Transition point when the current starts dropping from its maximum set value is important information of this graph. Ti mesh and four sponge specimens exhibit longer period of stage zero, while flat specimens that have $1cm^2$ area for anodization show short period of the initial stage. The time of the zero stage is proportional to the surface area. More amount of electron charges are needed to form homogeneous oxide layer on the enlarged area. Based on the relation between electron charges and anodization time in equation 5-3 and known information of the surface area of the standard specimen, surface area can be calculated (table 5-2).

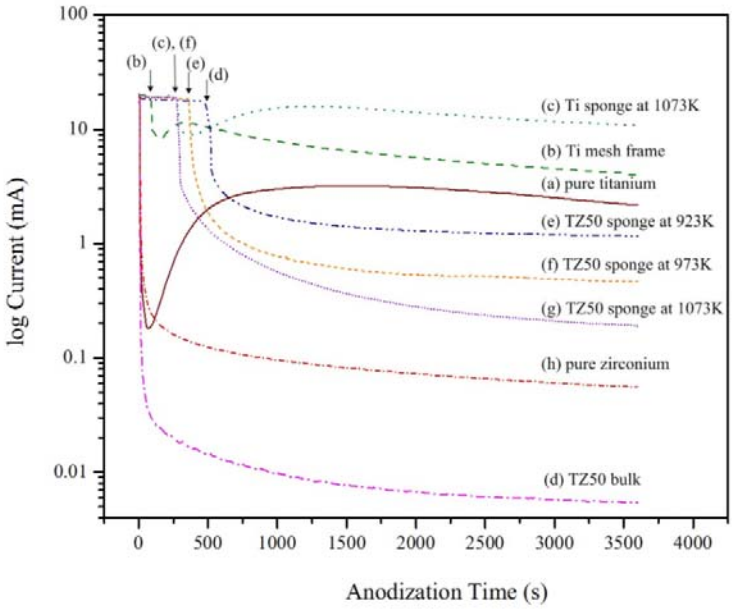

Figure 5-3. Graph of current density vs. time during potentiostatic anodization at 30V in 1% H_3PO_4 solution

Table 5-2. Transition points during anodic oxide growth by potentiostatic polarization; Surface area estimation of anodized alloy sponge samples

	Specimen	Transition point [seconds]	Estimated Area [cm^2]
(a)	pure Ti bulk	8	1*
(b)	pure Ti mesh frame	92	11.5
(c)	pure Ti porous sponge, 1073K	276	34.5
(d)	50Ti-50Zr bulk	8	1*
(e)	50Ti-50Zr porous sponge, 923K	484	60.5
(f)	50Ti-50Zr porous sponge, 973K	360	45
(g)	50Ti-50Zr porous sponge, 1073K	272	34
(h)	pure Zr bulk	8	1*

* Measured surface area on flat specimens

Final level of the anodization current also reflects surface area. In comparison to sponge structure synthesized at 973K, (f), and 1073K, (g), the Ti-Zr alloy sponge synthesized at 923K, (e), has higher level of anodization current. It must be due to its high surface area caused by small particles. Specimen (c), the pure Ti sponge, and (g), Ti-50at.%Zr sponge, were synthesized at the same reduction temperature. They behave similarly at the early of anodization in the zero stage, showing almost same transition point and surface area. However, once it passed the point, specimen (c) shows similar behavior with the flat Ti specimen, while specimen, (g), Ti-50at.%Zr synthesized at 1073K, behaves like the flat Ti-Zr bulk specimen.

Although, it shows lower anodization current as much as the one on the flat Ti-Zr alloy specimen, (d), the current of specimen (e), the 923K-Ti-50at.%Zr sponge, is still high because of its large surface area.

5.3.2 Leakage Current, Capacitance and Dissipation Factor of Anodic (Ti-Zr)O_2 Dielectric Films

Capacitance and dissipation factor are shown in table 5-3 and figure 5-4. Without a doubt, Ti sponge shows the highest value of capacitance with very high dissipation factor. All three Ti-Zr alloy sponge specimens—(e), (f), and (g)—exhibit well improved value of capacitance in comparison to standard bulk Ti-Zr alloy specimen. However, they allow increase of dissipation factor, either.

Franklin [26] suggested a selection limit of maximum leakage current that can be allowable for capacitor, which also used for estimation of Ta solid capacitor. The limit is 10 nA/μFV. It can be obtained by calculation of measured leakage current, capacitance, and applied test voltage for leakage current. As it is shown in table 5-4 and figure 5-5, all three Ti-50at.%Zr alloy specimens sufficiently satisfy the selection limit in any applied test voltage. On the other hand, the flat Ti specimen as well as Ti sponge specimen synthesized at 1073K does not satisfy the selection limit.

Table 5-3. Capacitance and dissipation factors of synthesized Ti-Zr alloy/(Ti-Zr)O_2 samples

	Specimen	Capacitance [μF]	weight [g]	C/w [μF/g]	Dissipation Factor
(a)	pure Ti bulk	4.570		-	1.719
(b)	pure Ti mesh frame	-		-	-
(c)	Ti sponge, 1073K	30.000	0.321	93.458	3.150
(d)	50Ti-50Zr bulk	0.371		-	0.371
(e)	TZ50 sponge, 923K	14.780	0.297	49.764	1.190
(f)	TZ50 sponge, 973K	6.620	0.329	20.122	0.859
(g)	TZ50 sponge, 1073K	4.218	0.313	13.476	0.573
(h)	pure Zr bulk	0.283		-	0.088

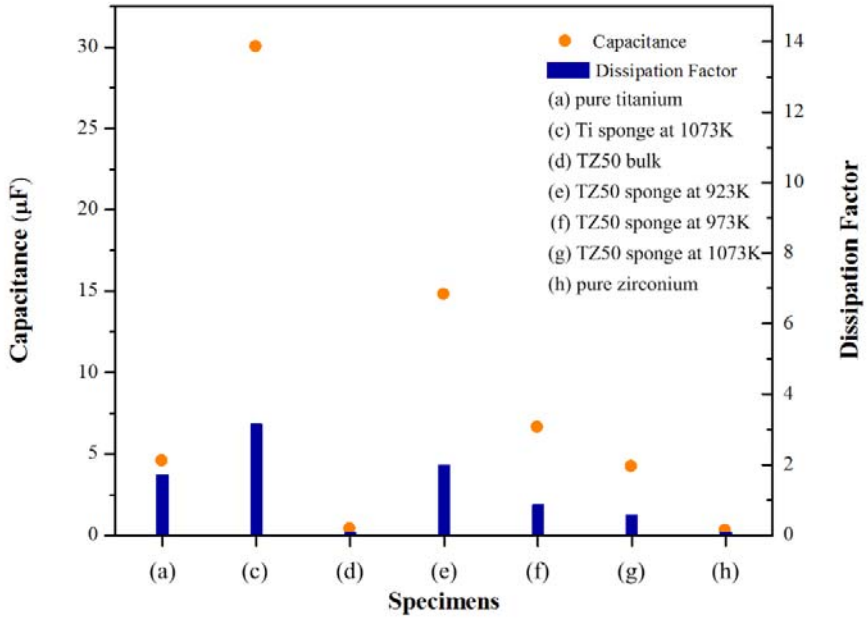

Figure 5-4. Capacitance and dissipation factor of various sponge specimens

Table 5-4. Leakage current of anodic (Ti-Zr)O_2 films and its dependence on capacitance and voltage

Leakage Current [nA/μFV]		Test Voltage [V]					
		3	**5**	**10**	**15**	**20**	**30**
(a)	pure Ti bulk	0.561	4.108	19.975	20.869	24.096	22.604
(c)	Ti sponge, 1073K	0.027	0.048	10.238	40.222	29.661	19.759
(d)	50Ti-50Zr bulk	0.329	0.361	0.376	0.494	0.478	0.600
(e)	TZ50 sponge, 923K	0.073	0.053	1.907	2.354	2.935	3.652
(f)	TZ50 sponge, 973K	0.019	0.253	4.161	4.904	5.052	4.251
(g)	TZ50 sponge, 1073K	0.031	0.397	2.367	3.374	3.410	2.725
(h)	pure Zr bulk	0.978	0.947	0.943	1.159	1.687	5.846

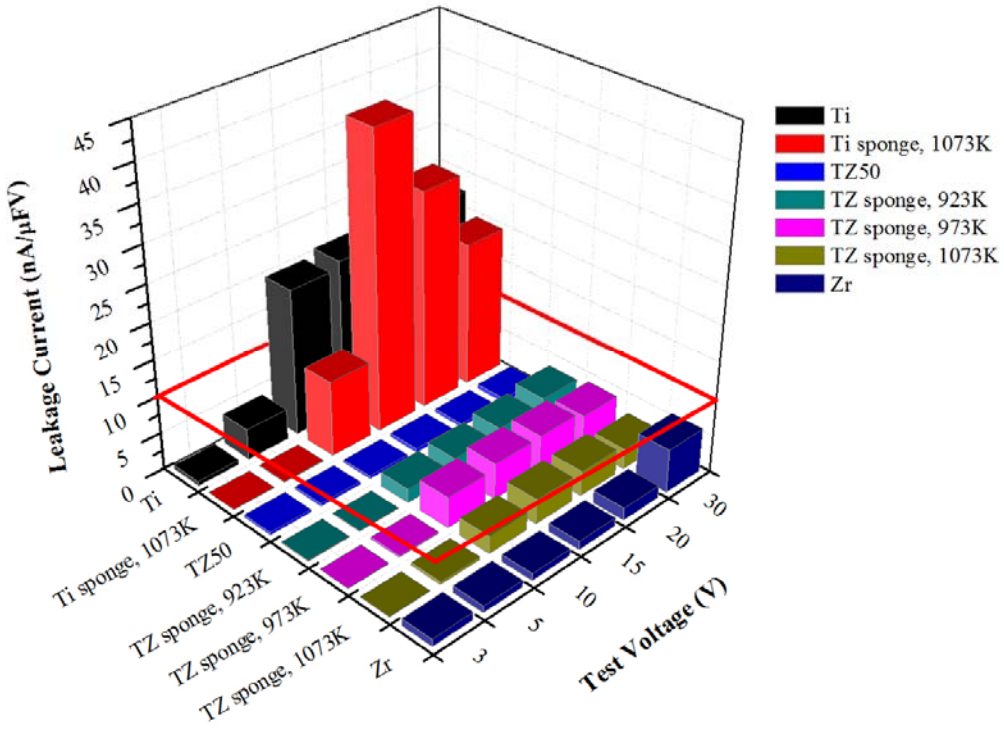

Figure 5-5. Leakage current with capacitance and voltage of various specimens. The red line represents the maximum permissible leakage current selection limit of 10 nA/μFV, suggested by Franklin [26]

5.3.3 Energy Density and Charge Density

Haas et al. suggested to use a value of charge density to estimate porous capacitor anode [16] [17] [18]. It is represented by product of capacitance, the reciprocal of weight and maximum anodizing voltage.

$$charge\ density = \frac{CV_{\max}}{w}\,[\mu FV/g] \tag{5-4}$$

where C represents capacitance, w is weight of the capacitor and V_{max} is maximum applied voltage. This value includs surface area and density of anode; thus it could be a simple and useful value to estimate performance of capacitor. Also, the specific energy density of capacitor is,

$$specific\ density = \frac{\left(\frac{1}{2}CV^2\right)}{mass}\,[MJ/kg] \tag{5-5}$$

Table 5-5. Energy density and charge density of anodic (Ti-Zr)O_2 dielectric films

	Specimen	Charge Density [CV/g]	Energy Density [J/g]
(c)	pure Ti porous sponge, 1073K	2,803	0.042
(e)	TZ50 porous sponge, 923K	1,492	0.022
(f)	TZ50 porous sponge, 973K	603	0.009
(g)	TZ50 porous sponge, 1073K	404	0.006

Table 5-5 shows the calculated value of charge density and energy density of various synthesized porous sponge structure. The energy density of pure Ti porous sponge reaches 0.042 J/g. The Ti-50at.%Zr alloy sponge specimen synthesized at 923K shows the highest value of charge density and energy density among the Ti-Zr alloy sponge specimens. The energy density was 0.022 J/g. Since Ti mesh is used as a frame to grab the Ti-Zr alloy particles, weight of Ti-Zr alloy sponge includes weight of Ti mesh frame. Weight of the frame was averagely almost 60% of the developed sponge anode.

Although the energy density of the developed porous anode was not high, it shows a possibility of the potential application to the electrolytic capacitor. Especially for the leakage current, it reaches very low level of the leakage. It is possible that with further research the porous Ti-Zr alloy sponge with nano-scale fine particles could be commercially used in the future.

5.4 Conclusions

Porous Ti-Zr sponge specimens, synthesized by developed magnesiothermic reduction process, were anodized in phosphoric acid solution. Surface area was estimated by comparing its transition time of reaching constant voltage with flat specimens that have 1cm^2 area for anodization. The estimated specific surface area of sponge specimen was maximum 60.5 times larger than the one with flat surface. The current change of the alloy sponge specimen during anodization shows similar behavior with the flat specimen of Ti-Zr alloy; it shows normal current drop during anodization. However, the measured current of pure Ti sponge specimen shows similar behavior with the flat Ti specimen. The current increases after rapid drop of the early stage of anodization. The trend is also shown in the result of leakage current measurement; sponge specimen of the Ti-Zr alloy shows lower leakage current than specimens with pure Ti. It is satisfying a standard of leakage current measurement of commercial electrolytic capacitors (10nA/μFV). Estimated value of energy density of porous Ti-Zr sponge specimen is reached to 0.022 J/g.

Conclusions and Suggestion for Future Works

One objective of the present work was to develop a method for the synthesis of the fine-porous Ti-Zr sponge structure that can be used for anodes of electrolytic capacitors. Magnesiothermic reduction reaction of titanium tetraiodide and zirconium tetrachloride was chosen as the process. The reaction was designed to take place on the surface-layer of melting magnesium plate. After the reaction, the unwanted products of the reaction, namely magnesium iodide and magnesium chloride, were removed by a vacuum distillation process. This developed a fine-porous sponge structure with nano-scale particles. It was then anodized and tested as an anode of electrolyte capacitor. The anodic oxide layer on pure titanium was also characterized by using electrochemical and microstructural analyses. After characterization of the anodic oxide layer on pure Ti, alloying of Ti with Zr was tried to form more resistive oxide and to achieve a lower leakage current. The electrochemical properties of the anodic oxide films formed on Ti-Zr alloy were then investigated.

The experimental results have shown that only at the beginning of 30V-anodization of pure titanium the newly formed TiO_2 is amorphous and resistive. However, within 90 seconds it transformed to a crystal structure. Nanocrystalline regions were observed by SEM and TEM. The oxide appears to have two sub-layers, an amorphous outer layer and an inner nanocrystalline layer. After about 300 seconds of anodization, additional small nodules and islands are observed on the oxide surface. This secondary anodization seems to be caused by repassivation in the oxide. The

repassivation continues until the entire oxide transformed to a new two sub-layers; the inner nanocrystal layer and the outer porous anatase layer. Since less amount of repassivation occurs, total current density of anodization decreases. By adding zirconium, the resistivity of the oxide on Ti-Zr alloy is improved. Through potentiodynamic anodic polarization measurement, the high resistivity of anodic oxide films on binary alloys was confirmed. The oxides formed on binary Ti-Zr alloys containing 40at.% to 60at.% Zr show extremely low leakage current density.

Using magnesiothermic reduction, TiI_4 and $ZrCl_4$ were reduced. Controlling pressure and temperature, those halides had reaction with Mg, and formed Ti-Zr alloy sponge mixed with by-products and Mg remainder. The pyro-vacuum distillation was an effective method to get rid of unwanted chemicals. After the pyro-vacuum distillation process, porous structure with nanometer-scale fine particles was obtained. The particle size could be controlled by reduction temperature and time. The results of XRD analysis represent that the porous structure consists of Ti-Zr alloy.

The synthesized porous sponge specimens were then anodized and tested as an anode of electrolytic capacitor. The results of capacitance measurement show that Ti-50at.%Zr synthesized at 923K has the highest capacitance value by large surface area among the synthesized specimens. The potentiodynamic polarization test and the leakage current measurement show that it has decreased leakage current in comparison with the anodic oxide films on pure Ti. Thus, the Ti-50at.% Zr sponge specimen synthesized at 923K can be used as the anode of the electrolytic capacitors.

Further exploration the following topics should be considered.

Studies of the electrochemical properties of the oxide on the Ti-Zr alloy using AC impedance. The EIS can give us more information about the resistivity of the complex oxide. Also by using the EIS, the porous nanostructure can be analyzed. EIS is very widely used analyzing method to investigate porous structure.

Based on the developed magnesiothermic process, development of a new process to synthesize a porous structure with different alloying composition can be considered. Other halides can be used to form alloyed sponge structure such as Ti-Nb or Ti-Al, which also can be used as anodes of electrolytic capacitors.

Appendix A

Optical Micrographs of Titanium Oxide Surface Anodized at 30V

9 second 90 second 300 second 1500 second 3600 second

Figure A-1. Color change of anodized titanium surface

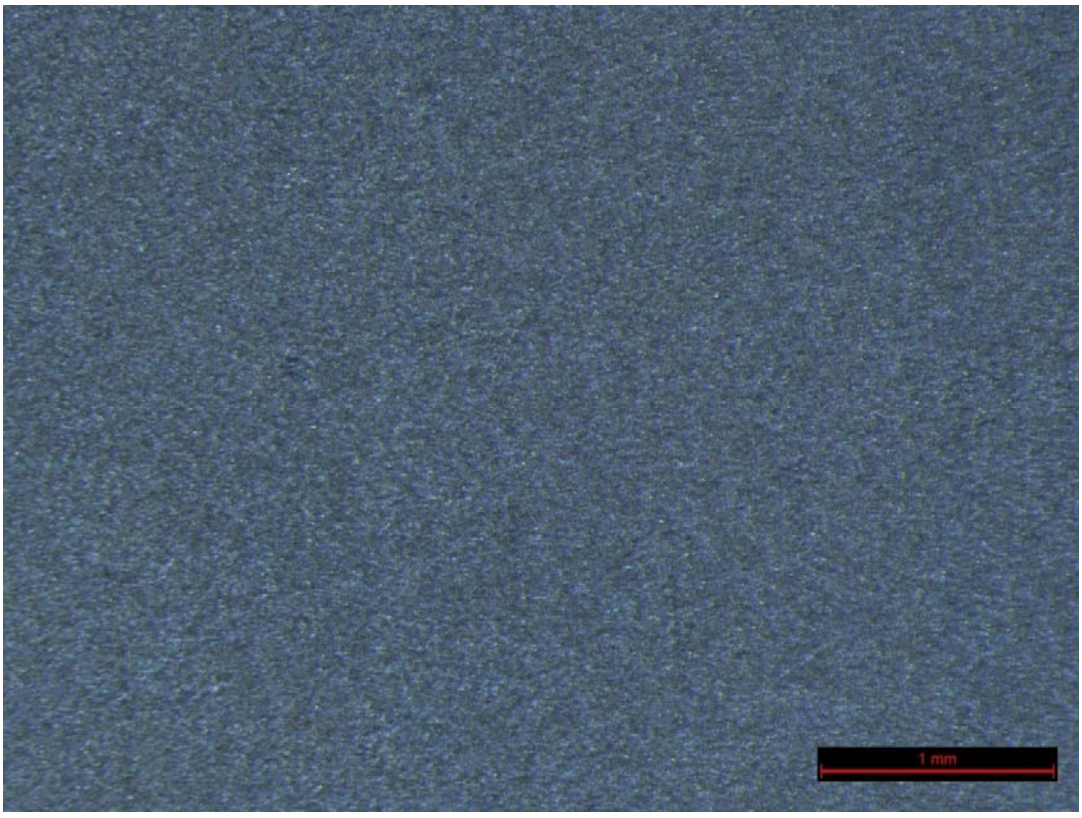

Figure A-2. Optical micrograph of titanium surface anodized at 30V after 9 seconds

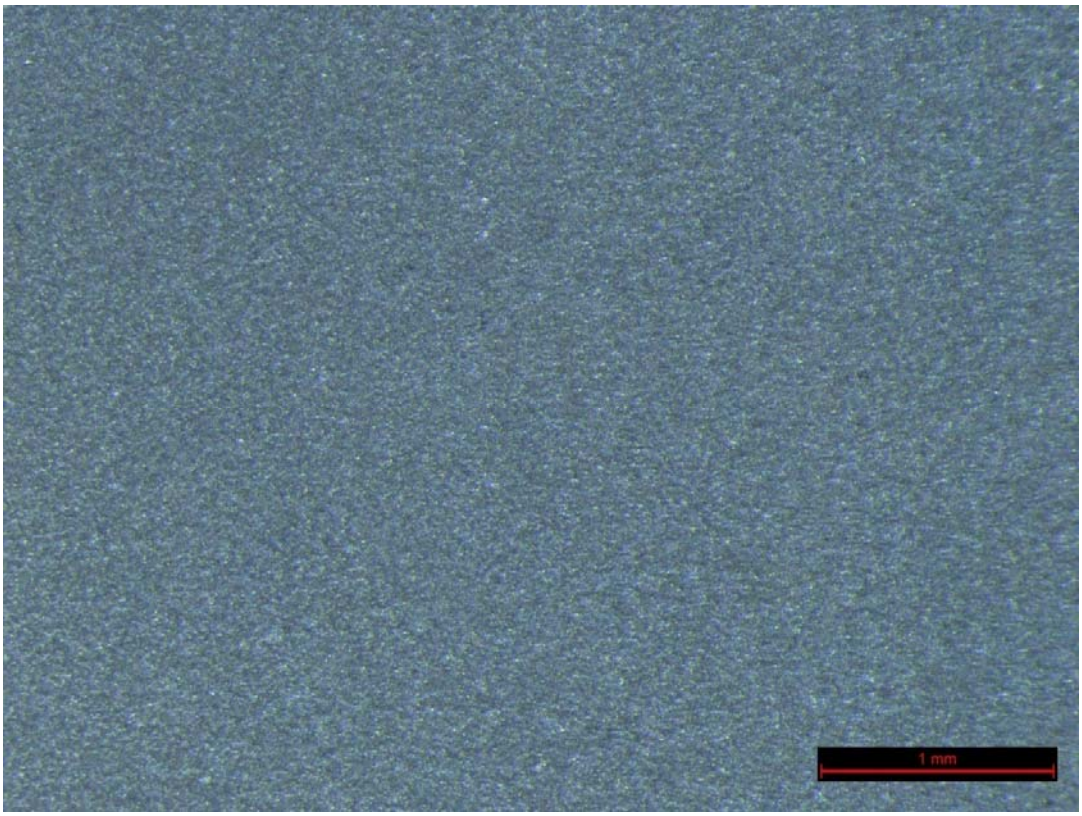

Figure A-3. Optical micrograph of titanium surface anodized at 30V after 90 seconds

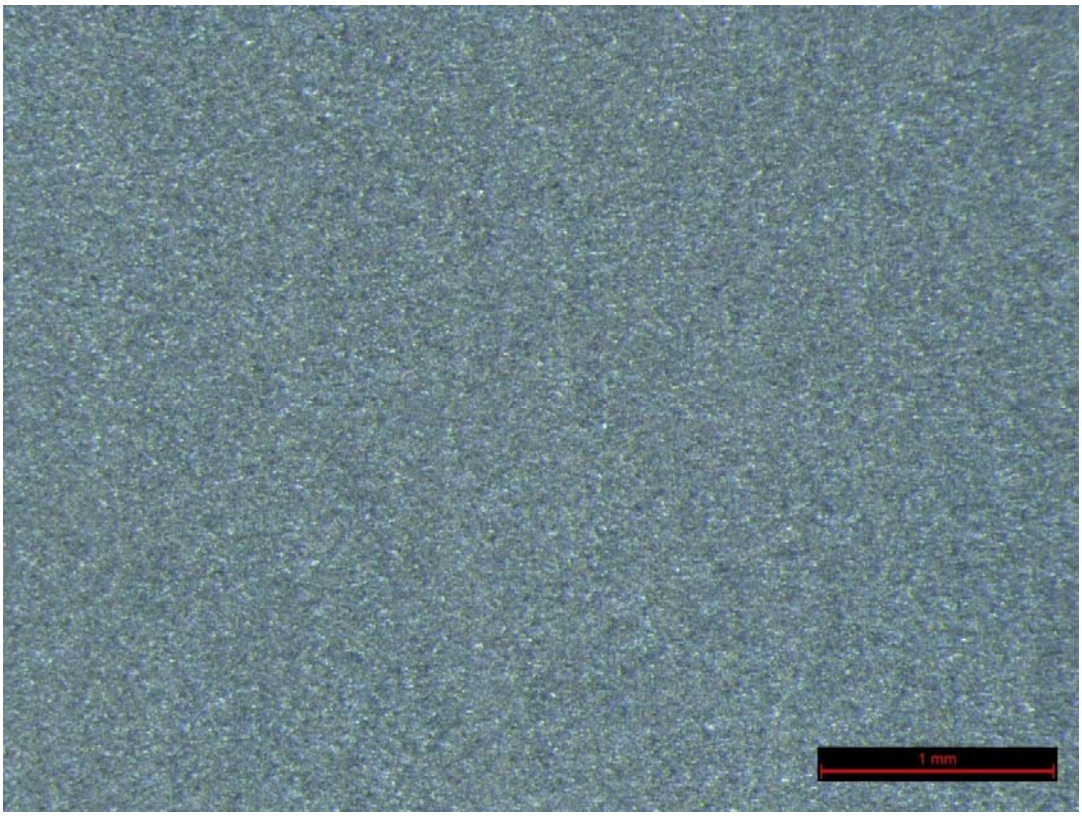

Figure A-4. Optical micrograph of titanium surface anodized at 30V after 300 seconds

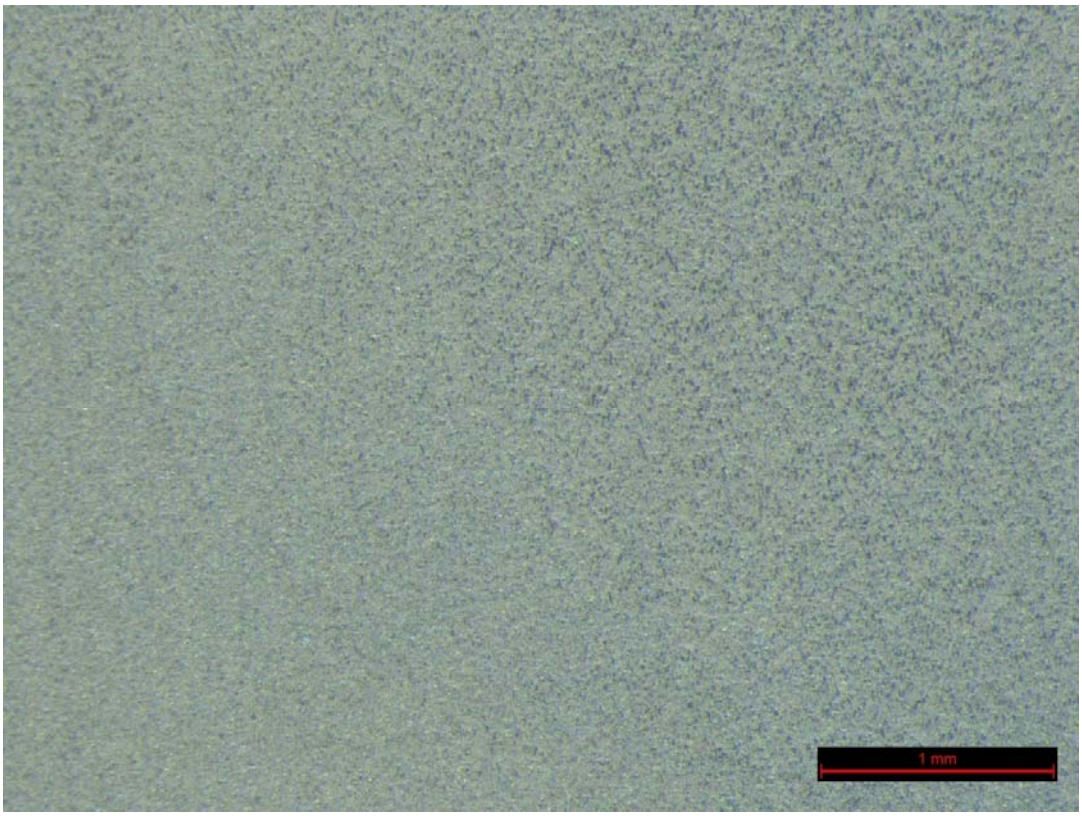

Figure A-5. Optical micrograph of titanium surface anodized at 30V after 1500 seconds

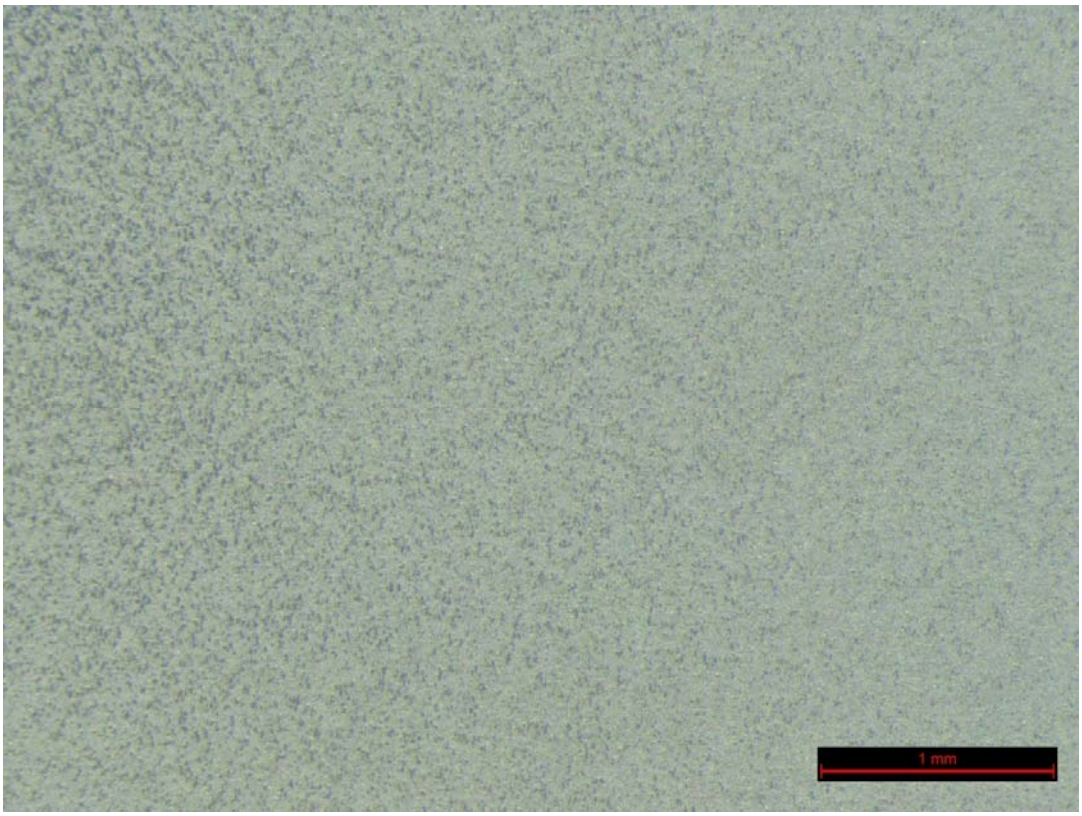

Figure A-6. Optical micrograph of titanium surface anodized at 30V after 3600 seconds

Appendix B

Snapshots of Movie Clip of the Evolution of Selected Area Diffraction Pattern (in TEM) of an Initially-Formed Anodic Amorphous TiO_2 Layer

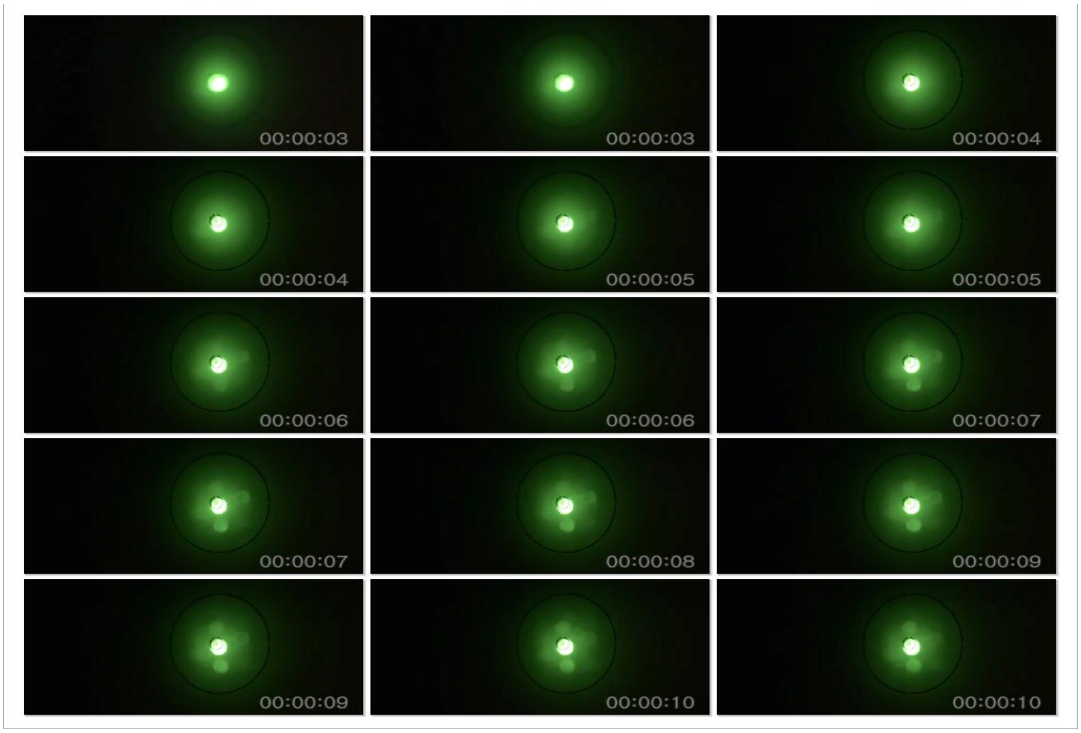

Figure B-1. Snapshots of movie clip showing diffraction pattern in high-resolution TEM of a selected area of anodically formed TiO_2 layer during focused electron irradiation; a time frame spanning 03 to 10 seconds.

At the initial of the electron irradiation in TEM a diffused diffraction pattern is observed. It is characteristic of amorphous oxide. During focused electron irradiation in TEM the diffraction develops diffraction spots indicating a transformation from amorphous to (nm) crystalline oxide. It appears that amorphous phase initially exists in the anodic TiO_2 film.

Appendix C

Nyquist Plots for Anodic TiO_2 Layers Grown during Different Anodizing Times at 30 Volts

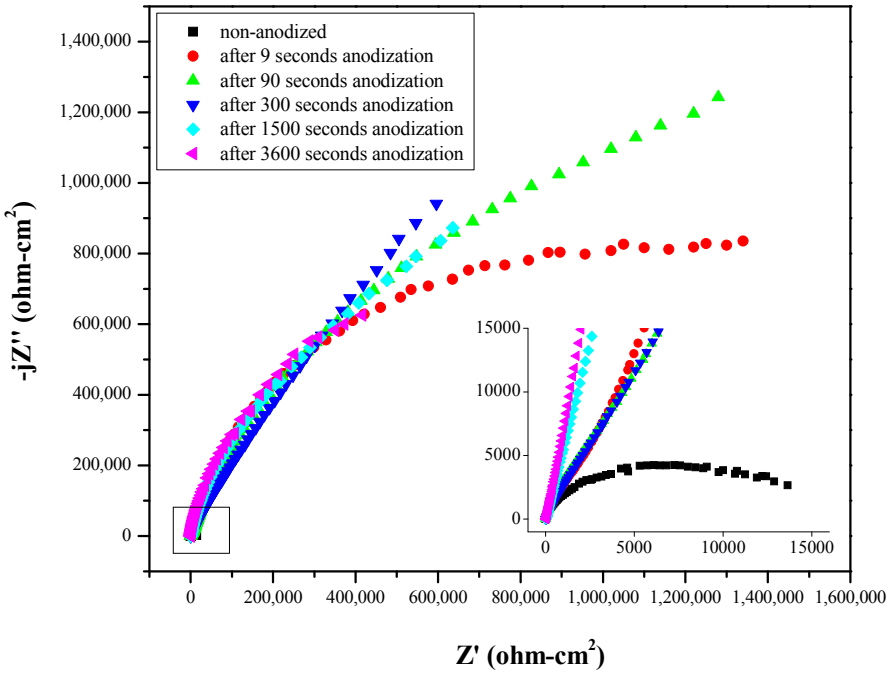

Figure C-1. Nyquist plots for anodic TiO_2 layers formed during different anodizing times at 30 Volts

Black dots in the inset graph represent impedance spectrum of the natural oxide film formed on Ti specimen in the air. It shows much smaller resistance than the anodized specimens. The 9s to 3600s times represent fully grown oxide films without and with increasing amounts of self-repair. It shows very high polarization resistance

(radius of partial semicircles) in all anodizing time condition. This generally happens in a highly capacitive system and brings difficulty to analyze low-frequency limit in the plot [39]. Thus, Bode plots are used for analyzing anodic oxide films in this study.

References

1 Ho, J., Jow, T. R., and Boggs, S. *IEEE Electrical Insulation Magazine*, 26 (2010), 20.

2 Moulson, A. J. and Herbert, J. M. *Electroceramics: Materials, Properties, Applications*. John Wiley and Sons, San Francisco, CA, USA, 2003.

3 Nishino, A. *Journal of Power Sources*, 60 (1996), 137.

4 Jain, R., Chou, B., McGervey, D., Chung, J., and Welsch, G. Anodic TiO2 Films Doped with Alkali-Earth Oxides. In Brodd et al., R. J., ed., *The Electrochemical Society Proceedings Series, Electrochemical Capacitors and Hybrid Power Sources*. The Electrochemical Society INC, Pennington, NJ, USA, 2002.

5 Schultz, J. W. and Lohrengel, M. M. *Electrochimica Acta* , 45 (2000), 2499.

6 AVX. *Dielectric Comparison Chart*.

7 HOLYSTONE CAPACITORS. *Technical Note; Capacitor Dielectric Comparison*.

8 Bettacchi, P., Montanari, D., Zenarini, D., Orioli, D., Rondelli, G., and Sauna, A. Power Films Capacitors for Industrial Applications. *Proceedings CARTS Europe 2010 - Symposium for Passive Electronics* (2010), 53.

9 Shukla, A. K., Banerjee, A., Ravikumar, M. K., and Jalajakshi, A. *Electrochimica Acta*, 84 (2012), 165.

10 Cavigliasso, G. E., Esplandiu, M. J., and Macagno, V. A. *Journal of Applied Electrochemistry*, 28 (1998), 1213.

11 Fischer, V., Stormer, H., Gerthsen, D., Stenzel, M., Zillgen, H., and Ivers-Tiffee, E. Niobium as New Material for Electrolytic Capacitors with Nanoscale Dielectric Oxide Layers. In *Proceedings of the 7th International Conference on Properties and Applications of Dielectric Materials* (Nagoya, Japan 2003).

12 Wilhelmsen, W. *Electrochimica Acta*, 33 (1988), 63.

13 Badawy, W. A. and Ismail, Kh. M. *Elctrochimica Acta*, 38 (1993), 2231.

14 Al-Kharafi, F. M. and Badawy, W. A. *Electrochimica Acta*, 40 (1995), 2623.

15 Badawy, W. A., Elegamy, S. S., and Ismail, Kh. M. *British Corrosion Journal*, 28 (1993), 133.

16 Haas, H. Magnesium Vapour Reduced Tantalum Powders with Very High Capacitance. *Proceedings CARTS Europe 2004 Nice France* (2004), 5.

17 Haas, H., Schnitter, C., Sato, N., Karabulut, H., Fujimori, Y., and Thomas, O. Challenge: Highest Capacitance Tantalum Powders. *Proceedings CARTS USA 2009 Jacksonville Florida* (2009), 98.

18 Horacek, I., Zednicek, T., Zednicek, S., Karnik, T., Petrzilek, J., Jacisko, P., and Gregorova, P. High CV Tantalum Capacitors - Challenges and Limitations. *Proceedings CARTS USA 2009 Jacksonville Florida* (2009), 159.

19 Zednicek, T., Sikula, J., and Leibovitz, H. A Study of Field Crystallization in

Tantalum Capacitors and its effect. *Proceedings CARTS USA 2009 Jacksonville Florida* (2009), 266.

20 Agulyanski, A. *The chemistry of tantalum and niobium fluoride compounds*. Elsevier, Boston, U.S.A, 2004.

21 *metal-pages.com*.

22 Chou, B., McGervey, D., Landau, U., and Welsch, G. Anodic Formation of TiO2 Dielectric Films. *Electrochemical Society Proceedings Series, PV2002-7, Electrochemical Capacitors and Hybrid Power Sources, The Electrochemical Society INC., Pennington, NJ, USA* (2002), 365.

23 Kalapos, T., Landau, U., and Welsch, G. Characterization of Electrochemically Formed Anodic Oxide Films on Titanium. *The Electrochemical Society Proceedings Series, PV2002-7, Electrochemical Capacitors and Hybrid Power Sources, The Electrochemical Society INC., Pennington, NJ, USA* (2002), 397.

24 Oh, M.-Y., Choe, H.-C., and Ko, Y.-M. *Advanced Materials Research*, 26-28 (2007), 817.

25 Santamaria, M., Di Quarto, F., and Habazaki, H. *Electrochimica Acta*, 53 (2008), 2272.

26 Franklin, R.W. *Analysis of Solid Tantalum Capacitor Leakage Current*. AVX.

27 *Testing Super-Capacitors, Part I -CV, EIS and leakage current*. Gamry Instruments, Inc., Warminster, PA.

28 Gerhardt, R. *Journal of Physics and Chemistry of Solids*, 55 (1994), 1491.

29 Tomozawa, M., Cordaro, J., and Singh, M. *Journal of Materials Science*, 14 (1979), 1945.

30 Abdullah Dar, M., Batoo, K.M., Verma, V., Siddiqui, W.A., and Kotnala, R.K. *Journal of Alloys and Compounds*, 493 (2010), 553.

31 Behera, B., Nayak, P., and Choudhary, R.N.P. *Journal of Alloys and Compounds*, 436 (2007), 226.

32 Chaudhary, A., Welch, J.O, and Jackman, R.B. *Applied Physics Letters*, 96 (2010), 242903.

33 Voelker, R.H., Lei, G.-T., Pan, G.-W., and Gilbert, B.K. Determination of Complex Permittivity of Low-Loss Dielectrics. *IEEE Transactions on Microwave Theory and Techniques*, 45 (1997), 1955.

34 Pfeifer, S., Park, S.-H., and Bandaru, P.R. *ECS Solid State Letters*, 2 (2013), M5.

35 Jones, D.A. *Principles and Prevention of Corrosion*. Prentice Hall, Upper Saddle River, NJ, 1996.

36 *G102-89, Standard Practice for Calculation of Corrosion Rates and Related Information from Electrochemical Measurments*. ASTM, West Conshohocken, PA, 1999.

37 Macdonald, D.D. *Electrochimica Acta* , 51 (2006), 1376.

38 Orazem, M.E. and Tribollet, B. *Electrochemical Impedance Spectroscopy*. John

Wiley and Sons, Hoboken, NJ, 2008.

39 Cottis, R. and Turgoose, S. *Electrochemical Impedance and Noise*. NACE International, Houston, TX, 1999.

40 Lvovich, V.F. *Impedance Spectroscopy - Applications to Electrochemical and Dielectric Phenomena*. John Wiley & Sons, Inc., Hoboken, NJ, 2012.

41 Laisa, A. Electrochemical Impedance Spectroscopy and its Application. In Conway, B.E. et al., eds., *Modern Aspects of Electrochemistry*. Kluwer Academic/Plenum Publishers, New York, NY, 1999.

42 *http://www-groups.dcs.st-and.ac.uk/~history/Mathematicians/Heaviside.html*.

43 Jüttner, K. *Electrochimica Acta*, 35 (1990), 1501.

44 Schnider, M., Schroth, S., Schilm, J., and Michaelis, A. *Electrochimica Acta*, 54 (2009), 2663.

45 Hsu, C. H. and Mansfeld, F. *Corrosion*, 57 (2001), 747.

46 Hirschorn, B., Orazem, M. E., Tribollet, B., Vivier, V., Frateur, I., and Musiani, M. *Electrochimica Acta*, 55 (2010), 6218.

47 Brug, G. J., Van Den Eeden, A. L. G., Sluyters-Rehbach, M., and Sluysters, J. H. *Journal of Electroanalytical Chemistry*, 176 (1984), 275.

48 Krstajić, N. V., Jović, V. D., Gajić-Krstajić, Lj., Jović, B. M., Antozzi, A. L., and Martelli, G. N. *International Journal of Hydrogen Energy*, 33 (2008), 3676.

49 Birry, L. and Lasia, A. *Journal of Applied Electrochemistry*, 34 (2004), 735.

50 Hirschorn, B., Orazem, M. E., Tribollet, B., Vivier, V., Frateur, I., and Musiani, M. *Journal of Electrochemical Society*, 157 (2010), C452.

51 Hirschorn, B., Orazem, M. E., Tribollet, B., Vivier, V., Frateur, I., and Musiani, M. *Journal of Electrochemical Society*, 157 (2010), C458.

52 Musiani, M., Orazem, M. E., Pebere, N., Tribollet, B., and Vivier, V. *Journal of Electrochemical Society* , 158 (2011), C424.

53 Popa, M. V., Demetrescu, I., Suh, S.-H., Vasilescu, E., Drob, P., Ionita, D., and Vasilescu, C. *Bioelectrochemistry*, 71 (2007), 126.

54 Lavos-Valereto, I. C., Wolynec, S., Ramires, I., Guastaldi, A. C., and Costa, I. *Journal of Materials Science: Materials in Medicine*, 15 (2004), 55.

55 Gonzalez, J. E. G. and Mirza-Rosca, J. C. *Journal of Electroanalytical Chemistry*, 471 (1999), 109.

56 Pan, J., Theirry, D., and Leygraf, C. *Electrochimica Acta* , 41 (1996), 1143.

57 Sul, Y.-T., Johansson, C.B., Jeong, Y., and Albrektsson, T. *Medical Engineering & Physics*, 23 (2001), 329.

58 Ferreira, E. A., Rocha-Filho, R. C., Biaggio, S. R., and Bocchi, N. *Corrosion Science* , 52 (2010), 4058.

59 Duarte, L. T., Biaggio, S. R., Rocha-Filho, R. C., and Bocchi, N. *Corrosion Science* , 72 (2013), 35.

60 Fadl-allah, S. A. and Mohsen, Q. *Applied Surface Science*, 256 (2010), 5849.

61 McGervey, D. and Welsch, G. Energy and Power of Titanium Electrolytic Capacitors. *The Electrochemical Society Proceedings Series, PV2002-7, Electrochemical Capacitors and Hybrid Power Sources, The Electrochemical Society INC., Pennington, NJ, USA* (2002), 343.

62 Lohrengel, M. M. *Material Science and Engineering*, R11 (1993), 243.

63 Cotton, F.A. and Wilkinson, G. *Advanced Inorganic Chemistry, fifth ed.* Wiley Interscience, NY, 1988.

64 Lee, W.G., Woo, S.I., Kim, J.C., Choi, S.H., and Oh, K.H. *Thin Solid Films*, 237 (1994), 105.

65 Mantzila, A. G. and Prodromidis, M. I. *Electrochimica Acta* , 51 (2006), 3537.

66 Shibata, T. and Zhu, Y. -C. *Corrion Science* , 37 (1995), 253.

67 Marsh, J. and Gorse, D. *Electrochimica Acta* , 43 (1998), 659.

68 Lee, E.-J. and Pyun, S.-I. *Journal of Applied Electrochemistry*, 22 (1992), 156.

69 Mazzarolo, A., Curioni, M., Vicenzo, A., Skeldon, P., and Thompson, G.E. *Electrochimica Acta*, 75 (2012), 288.

70 Jaeggi, C., Kern, P., Michler, J., Patscheider, J., Tharian, J., and Munnik, F. *Surface and Interface Analysis*, 38 (2006), 182.

71 Xing, J. -H., Xia, Z. -B., Hu, J. -F., Zhang, Y. -H., and Zhong, L. *Journal of Electrochemical Society*, 160 (2013), C239.

72 Williams, K.R. and Muller, R.S. *Journal of Microelectromechanical Systems*, 5

(1996), 256.

73 Ki, J.-W. *Titanium sponge on titanium substrate for titanium electrolytic capacitor*. Ph.D. Dissertation, Case Western Reserve University. 2005.

74 Chen, L.-J. *Oxidation and Reduction Synthesis of Surface Enhanced Titanium Based Electrodes for Electrolytic Capacitors*. Ph.D. Dissertation, Case Western Reserve University. 2013.

75 Delplancke, J.-L., Degrez, M., Fontana, A., and Winand, R. *Surface Technology*, 16 (1982), 153.

76 Van Gils, S., Mast, P., Stijns, E., and Terryn, H. *Surface & Coatings Technology*, 185 (2004), 303.

77 Ashby, M., Shercliff, H., and Cebon, D. *Materials Engineering, Science, Processing and Design 3rd Ed.* Butterworth-Heinemann, Waltham, MA, 2014.

78 Young, L. *Proceedings of the Royal Society A*, 244 (1958), 41.

79 McAdam, Jr., D.J. and Geil, G.W. *Journal of Research of the National Bureau of Standards*, 28 (1942), 593.

80 Halary-Wagner, E., Bret, T., and Hoffman, P. *Applied Surface Science*, 208-209 (2003), 663.

81 Karambakhsh, A., Afshar, A., Ghahrama, S., and Malekinejad, P. *Journal of Materials Engineering and Performance*, 20 (2011), 1690.

82 Karambakhsh, A., Afshar, A., and Malekinejad, P. *Journal of Materials*

Engineering and Performance, 21 (2012), 121.

83 MacAdam, D.L. *Color Measurement*. Springer, New York, NY, 1981.

84 Xing, J.-H., Xia, Z.-B., Li, H., Wang, Y.-Y., and Zhong, L. *Transactions of Nonferrous Metals Society of China*, 23 (2013), 3286.

85 Michaelis, A., Delplancke, J.-L., and Schultze, J.W. *Materials Science Forum*, 185-188 (1995), 471.

86 Hammond, C.R. Principles of the Elements and Inorganic Compounds. In Lide, D.R., ed., *CRC Handbook of Chemistry and Physics (86th ed.)*. CRC Press, Boca Raton, FL, 2005.

87 Phillips, W.R. and Griffen, D.T. *Optical Mineralogy: The Non-opaque Minerals*. Freeman, New York, NY, 1981.

88 Whitten, K.W., Davis, R.E., Peck, M.L., and Stanley, G.G. *Chemistry*. Brooks/Cole, Belmont, CA, 2014.

89 Nelson, J.C. and Oriari, R.A. *Corrosion Science*, 34 (1993), 307.

90 Sato, N. *Journal of Electrochemical Society*, 16 (1971), 1683.

91 Habazaki, H., Uozumi, M., Konno, H. et al. *Electrochimica Acta*, 48 (2003), 3257.

92 Patrito, E.M., Torresi, R.M., Leiva, E.P.M., and Macagno, V.A. *Journal of Electrochemical Society*, 137 (1990), 524.

93 Macdonald, J.R. *Solid State Ionics*, 13 (1984), 147.

94 Hanini, F., Bouabellou, A., Bouachiba, Y., Kermiche, F., Taabouche, A., Hemissi, M., and Lakhdari, D. *IOSR Journal of Engineering*, 3 (2013), 21.

95 Roh, B. and Macdonald, R.R. *Russian Journal of Electrochemistry*, 43 (2007), 125.

96 Bhola, R., Bhola, S.M., Mishra, B., Ayers, R., Olson, D.L., and Ohno, T. Electrochemical Characteristics of Titanium and its Alloys in Phosphoric Buffer Saline. *Proceedings from the Materials & Processes for Medical Devices Conference* (2009), 52.

97 Devillers, D., Dinh, M.T., Mahe, E., Krulic, D., Larabi, N., and Fatouros, N. *Journal of New Materials for Electrochemical Systems*, 9 (2006), 221.

98 Kraskck-Cydzik, E. *Corrosion Science*, 46 (2004), 2487.

99 Hsu, C.H. and Mansfeld, F. *Corrosion*, 57 (2001), 747.

100 Hirschorn, B., Orazem, M.E., Tribollet, B., Vivier, V., Frateur, I., and Musiani, M. *Electrochimica Acta*, 55 (2010), 6218.

101 Brug, G.J., Van den Eeden, A.L.G., Sluyters-Rehbach, M., and Sluyters, J.H. *Journal of Electroanalytical Chemistry*, 176 (1984), 275.

102 Kerrec, O., Devilliers, D., Groult, H., and Chemla, M. *Electrochimica Acta*, 40 (1995), 719.

103 Santamaria, M., Di Quatro, F., and Habazaki, H. *Corrosion Science*, 50, 2012 (2008).

104 Okazaki, K. *Ceramics engineering for dielectrics*. Gakken Shya, Tokyo, 1969.

105 Andreeva, V. V. and Glukhova, A. I. *Journal of Applied Chemistry*, 11 (1961), 390.

106 Andreeva, V. V. and Glukhova, A. I. *Journal of Applied Chemistry*, 12 (1962), 457.

107 Oliveira, N. T. C., Biaggio, S. R., Nascente, P. A. P., Piazza, S., Sunseri, C., and Di Quarto, F. *Electrochimica Acta*, 51 (2006), 3506.

108 Grandin, H. M., Berner, S., and Dard, M. *Materials*, 5 (2012), 1348.

109 Oliveria, N.T.C., Biaggio, S.R., Rocha-Filho, R.C., and Bocci, N. *Journal of Biomedical Materials Research A*, 74 (2005), 397.

110 Ikarashi, Y., Toyoda, K., Kobayashi, E., Doi, H., Yoneyama, T., Hamanaka, H., and Tsuchiya, T. *Materials Transactions*, 46 (2005), 2260.

111 Habazaki, H., Shimizu, K., Nagata, S. et al. *Thin Solid Films*, 479 (2005), 144.

112 Thompson, D.P., Dickins, A.M., and Thorp, J.S. *Journal of Materials Science*, 27 (1992), 2267.

113 Vanhumbeeck, J.-F. and Proost, J. *Corrosion Reviews*, 27 (2009), 117.

114 Wood, G.C. and Pearson, C. *Corrosion Science*, 7 (1967), 119.

115 Boddy, P.J. *Journal of Electrochemical Society*, 115 (1968), 199.

116 Dyer, C.K. and Leach, J.S.L. *Journal of Electrochemical Society*, 125 (1978), 1032.

117 Matykina, E., Arrabal, R., Skeldon, P., Thompson, G.E., and Habazaki, H. *Thin Solid Film*, 516 (2008), 2296.

118 Abdel Rahim, M.A. *Journal of Applied Electrochemistry* , 25 (1995), 881.

119 Arico, A.S., Bruce, P., Scrosati, B., Tarascon, J.-M., and Schalkwijk, W.v. *Nature Materials*, 4 (2005), 366.

120 Exner, H.E. and Arzt, E. In Cahn, R.W. and Haasen, P., eds., *Physical Metallurgy*. Elsevier Science Publisher, Amsterdam, the Netherlands, 1983.

121 Li, C. and Zhu, Z. *Journal of Porous Materials*, 13 (2006), 21.

122 Ye, B. and Dunand, D. C. *Materials Science and Engineering A*, 528 (2010), 691.

123 Esen, Z. and Bor, S. *Scripta Materialia*, 56 (2007), 341.

124 Kwok, P. J., Oppenheimer, S. M., and Dunand, D. C. *Advanced Engineering Materials*, 10 (2008), 820.

125 Torres, Y., Pavo, J. J., and Rodriguez, J. A. *Metallurgical and Materials Transactions B*, 42B (2011), 891.

126 Arockiasamy, A., German, R. M., Heaney, D. F., Wang, P. T., Horstemeyer, M. F., King, R. L., and Adcock, B. *Powder Metallurgy*, 54 (2011), 420.

127 Dabrowski, B., Swieszkowski, W., Godlinski, D., and Kurzydlowski, K. J. *Journal of Biomedical Materials Research B: Applied Biomaterials*, 95B (2010), 53.

128 Chen, G. Z., Fray, D. J., and Farthing, W. *Nature*, 407 (2000), 361.

129 Ma, M., Wang, D., Wang, W., Hu, X., Jin, X., and Chen, G. Z. *Journal of Alloys and Compounds* , 420 (2006), 37.

130 Kroll, W. *Journal of the Electrochemical Society*, 78 (1940), 35.

131 Kapoor, K., Padmaprabu, C., and Nandi, D. *Materials Characterization*, 59 (2008), 213.

132 Barin, I., ed. *Thermochemical Data of Pure Substances*. Wiley-VCH Verlag GmbH, Weinheim, Germany, 1989.

133 Blocher Jr., J.M. and Campbell, I.E. *Journal of American Chemistry Society*, 69 (1947), 2100.

134 Hummers, W.S., Tyree Jr., S.Y., Yolles, S., Busalo, F., and Bauer, L. Zirconium and Hafnium Tetrachlorides. In Bailar, J.C., ed., *Inorganic Syntheses Vol.4*. McGraw Hill Book Company, New York, 1953.

135 Nagesh, Ch.R.V.S., Rao, Ch.S., Ballal, N.B., and Rao, P.K. *Metallurgical and Materials Transaction B*, 35B (2004), 65.

136 Evdokimov, V.I. and Krenev, V.A. *Inorganic Materials*, 38 (2002), 490.

137 Murray, J.L. *Bulletin of Alloy Phase Diagram*, 2 (1981), 197.

138 Luz, T., Henriques, V.A.R., de Oliveira, J.L., and Diniz, E.F. *Production of Ti-Zr Alloy by Powder Metallurgy*. SAE Technical Paper. 2013.

139 Vajtai, R. *Springer Handbook of Nanomaterials*. Springer Berlin Heidelberg,

Berlin, Germany, 2013.

140 Alloyeau, D., Prevot, G., Le Bouar, Y., Oikawa, T., Langlois, C., Loiseau, A., and Ricolleau, C. *Physical Review Letters*, 105 (2010), 255901-1.

141 Banfield, J.F. and Navrotsky, A., eds. *Nanoparticles and the Environment*. The Mineralogical Society of America, Washington, DC, 2001.

142 Sahu, P. and Prasad, B.L.V. *Langmuir*, 30 (2014), 10143.

143 Dewez, P. *Journal of the Institute of Metals*, 80 (1952), 525.

144 Madelung, O. *Group IV Physical Chemistry Volume 5J*. Springer Berlin Heidelberg, Berlin, 1998.

145 Brunsch, A. and Steeb, S. *Zeitschrift für Naturforschung A*, 29 (1974), 1319.

146 Kelly, J.J. and Vanmaekelbergh, D. Porous-etched Semiconductors: Formation and Characterization. In Hodes, G., ed., *Electrochemistry of Nanomaterials*. Wiley-VCH, Weinheim, 2001.

147 Khalil, N. and Leach, J.S.L. *Electrochimica Acta*, 31 (1986), 1279.

148 Vermilyea, D.A. Journal of The Electrochemical Society (1963), 345.